AD 711860

SU-SEL-69-012

Details of High Quantum Efficiency Photoemission in Gallium Arsenide

by

Lawrence William James

March 1969

Technical Report No. 5221-2

Prepared under
U. S. Army Contract DA 44-009 AMC-1474(T), and
Center for Materials Research Contract SD-87

"This document has been approved for public release and sale; its distribution is unlimited."

DDC
RECEIVED
SEP 30 1970
C

SOLID-STATE ELECTRONICS LABORATORY

STANFORD ELECTRONICS LABORATORIES

STANFORD UNIVERSITY · STANFORD, CALIFORNIA

SEL-69-012

DETAILS OF HIGH QUANTUM EFFICIENCY PHOTOEMISSION IN GALLIUM ARSENIDE

by

Lawrence William James

March 1969

Technical Report No. 5221-2

Prepared under
U.S. Army Contract DA 44-009 AMC-1474(T)

and

Center for Materials Research Contract SD-87

Solid-State Laboratory
Stanford Electronics Laboratories
Stanford University Stanford, California

ABSTRACT

Using the technique of high resolution energy distribution analysis of electrons photoemitted from a cleaved GaAs surface coated with cesium and oxygen layers, we have been able to determine many of the properties of GaAs which are important in the operation of the GaAs-Cs-O photocathode and other GaAs devices. A two minima diffusion model is presented which explains the photon energy dependence of the photocathode yield near threshold. Electron diffusion lengths for the Γ_1 and X_1 minima have been determined from the spectral shape of quantum yield as a function of temperature and carrier concentration for heavily doped p-type material. The hot electron scattering length for equivalent intervalley scattering has been measured by comparison with a computer scattering model. The coupling constant for equivalent intervalley scattering has been calculated from the hot electron scattering length. The coupling constant for scattering between the Γ_1 and X_1 minima is calculated from the X_1 diffusion length. These results, along with other recent data, are used to calculate the temperature dependence of the mobility in the X_1 valleys and the intervalley scattering time. The positions of several of the conduction band minima are determined, including the temperature dependence of the location of the Γ_1 and X_1 minima. The temperature dependence of the velocity-field characteristic is calculated using the measured coupling constants and temperature dependence of the Γ_1 to X_1 spacing. The escape probability for the photocathode and the shape of the energy distribution curves is explained by a model which includes optical phonon scattering in the band-bending region, reflection at the surface, trapping in surface states, and lifetime broadening. The escape probability as a function

of electron energy is measured, both for the case of a single cesium layer surface treatment and for the case of a Cs + $(O+Cs)^n$ surface treatment where absorption of electrons in the 'n' oxygen-cesium layers is included. Practical operation of the GaAs photocathode is discussed in terms of effects on yield of cooling, heating, exposure to bright light and high current densities, and various dopings and surface treatments.

CONTENTS

Page

I. INTRODUCTION 1

II. EXPERIMENTAL TECHNIQUES 2

A. The Basic Experiment 2

B. The Cesiation Process 6

C. Construction and Calibration of a New Reference Tube for the Visible Monochromator 9

D. Refinements in Energy Distribution Curve Measurements 13

1. Measurement of the Derivative of the Energy Distribution Curve 13

2. Resolution Improvements 17

III. THE TWO MINIMA DIFFUSION MODEL FOR PHOTOEMISSION NEAR THRESHOLD 22

IV. THE HOT ELECTRON SCATTERING MODEL FOR HIGHER PHOTON ENERGIES 41

V. CALCULATION OF INTERVALLEY COUPLING CONSTANTS 47

VI. TEMPERATURE DEPENDENCE OF THE X_1 MOBILITY AND DIFFUSION LENGTH 51

VII. TEMPERATURE DEPENDENCE OF THE HOT ELECTRON SCATTERING LENGTH 56

VIII. LOCATION AND IDENTIFICATION OF STRUCTURE IN THE ENERGY DISTRIBUTION CURVES 57

IX. DETAILS OF THE ESCAPE PROCESS 75

X. EFFECTS OF DOPING ON YIELD 92

XI. EFFECTS OF HEATING ON THE CLEAVED GaAs SURFACE 102

XII. THE FUTURE FOR PRACTICAL PHOTOCATHODES 104

XIII. SUGGESTIONS FOR FUTURE WORK 106

REFERENCES 107

TABLES

Number		Page
I	S-1 Reference Tube Yield	12
II	Measured Diffusion Lengths for Boat-Grown Zn-Doped Material	38
III	Physical Constants Used in the Calculations	41
IV	Experimental and Theoretical Values for the Location of Conduction Band Minima	73

ILLUSTRATIONS

Figure		Page
1	Diagram of the ultrahigh vacuum cleaving chamger in which photocathodes are prepared and measured	2
2	Photograph of the chamber in which experiments were done.	4
3	Photograph of the flange from the chamber of Figure 2 ...	5
4	Diagram of the connections used to monitor photocurrent during cesiation	7
5	Drawing of the reference tube assembly for the visible monochromator	10
6	Calibrated yield of the S-1 reference tube assembly	11
7	Experimental apparatus used to measure the energy distribution curve and its derivative	14
8	Principle of operation of the ac technique for measuring the energy distribution curve and its derivative	16
9	Experimental E.D.C. and derivative curves for a photon energy of 1.7 eV	18
10	Normalized and smoothed experimental energy distribution curves for a 1 x $10^{19}/cm^3$ Zn-doped GaAs crystal with a Cs + (O+Cs) surface treatment shown for increments of 0.2 eV for a photon energy range of 1.4 eV to 3.0 eV	21
11	Band-bending diagram showing the effects of a layer of cesium applied to a p^+ GaAs surface	23
12	GaAs band structure near the energy gap showing examples of photoexcitation, scattering, and thermalization in the Γ_1 and X_1 minima	24
13	Fraction of photoexcited electrons which thermalize in each minima	26
14	Equal energy contours for the first conduction band in GaAs in the (110) plane	27
15	Equal energy contours in one plane near the center of the Brillouin zone, illustrating the method used to find F_X and F_{Γ}	28

ILLUSTRATIONS (Contd)

Figure		Page
16	Theoretical and experimental yields from the X_1 minima in a 1 x $10^{19}/cm^3$ Zn-doped GaAs crystal with a Cs + (O+Cs) surface treatment	32
17	Experimental yield for the Γ_1 minima in a 1 x $10^{19}/cm^3$ Zn-doped GaAs crystal with a Cs + (O+Cs) surface treatment, compared with theory	33
18	p^+ GaAs optical absorption coefficient, α	34
19	Comparison between theoretical and experimental Γ_1 yields for various surface treatments	35
20	Comparison of the Γ_1 peak in 80°K energy distribution curves for photon energies of 1.6 to 2.3 eV	37
21	Comparison of calculated and measured energy distribution curves for an excitation at $h\nu$ = 3.0 eV	45
22	Scattering times for Γ_1 to X_1 scattering, polar optical scattering, and acoustic scattering for hot electrons in the Γ_1 minima	50
23	Temperature dependence of the various mechanisms which determine the mobility in the X_1 minima	52
24	Temperature dependence of the X_1 to Γ_1 scattering time ..	54
25	Experimental and theoretical temperature dependence of the X diffusion length	54
26	Energy distribution curves for a 3 x $10^{19}/cm^3$ Zn-doped sample for a photon energy of 3.0 eV over a temperature range of 80°K to 300°K	60
27	Energy distribution curves for a 3 x $10^{19}/cm^3$ Zn-doped sample for a photon energy of 1.6 eV over a temperature range of 80°K to 300°K	61
28	Temperature depencence of the GaAs velocity-field characteristic	63
29	Temperature dependence of the location of conduction band minima indicating best estimates and possible error ranges	64
30	The E.D.C. and its derivative for a photon energy of 1.5 eV on a 3 x $10^{19}/cm^3$ Zn-doped GaAs crystal	66

ILLUSTRATIONS (Contd)

Figure		Page
31	The E.D.C. and its derivative for a photon energy of 1.46 eV on the same crystal as Figure 28	67
32	Structure plot showing the location of structure measured using the high resolution can structure and the derivative curves for a $1 \times 10^{19}/cm^3$ Zn-doped GaAs crystal	69
33	p^+ GaAs photoemitted electron energy distribution curve for a photon energy of 2.2 eV	70
34	Derivative of energy distribution curves. A curve is given for $h\nu$ = 2.2 eV showing the position of the dominant X_1 peak as well as the L_1 shoulder and shoulders due to the unscattered electrons in the original optical excitation spectra. Also included in this figure is data for $h\nu$ = 4.65 eV showing only that portion corresponding to the X_3 conduction band minima	71
35	GaAs band structure calculated by Herman et al.,[3] using our experimental data as a perturbation on a first principles calculation	74
36	Comparison between theory and experiment for the shape of the 80°K energy distribution curve	79
37	Estimate from a simplified model of the effect of surface states on escape probability	81
38	Comparison between theory and experiment for the shape of the 80°K energy distribution curve for the case of C_E constant	83
39	High resolution electron energy distribution curve for a photon energy of 1.6 eV at 80°K showing determination of the vacuum level	85
40	Effects of additional oxygen-cesium layers, showing the vacuum level lowering and the electron absorption as measured experimentally	86
41	Surface escape probability vs electron energy above the work function, measured for a $1 \times 10^{19}/cm^3$ sample. Slight differences could be expected for different doping due to the differing doping due to the differing width of the band-bending region	87

ILLUSTRATIONS (Contd)

Figure		Page
42	Γ and X escape probability for a $1 \times 10^{19}/cm^3$ sample calculated using Figures 2 and 3	88
43	Energy distribution curves at 300°K showing the effect of 30 (O+Cs) layers on the energy distribution	89
44	Theoretically maximum possible yield for samples with two different diffusion lengths	93
45	Yield curves comparing different doping densities and surface treatments	94
46	Normalized energy distribution curves for a photon energy of 2.6 eV before and after oxygen and recesiation, for a $1 \times 10^{19}/cm^3$ Zn-doped crystal	95
47	Yield from electrons thermalized in the Γ_1 minimum for a $1 \times 10^{19}/cm^3$ Zn-doped crystal with a Cs-only and a Cs + (O+Cs) surface treatment	96
48	Yield from electrons thermalized in the X_1 minima for a $1 \times 10^{19}/cm^3$ Zn-doped crystal with a Cs-only and a Cs + (O+Cs) surface treatment	97
49	Experimental Γ escape probability for various surface treatments	99
50	Absolute quantum yield curves shown for optimum cesium-only treatment (4×10^{19} Cs), optimum oxygen-cesium treatment (1×10^{19} Cs + $(O+Cs)^6$), and, for comparison, a commercial S-1 photocathode	100
51	Yield at room temperature and liquid nitrogen temperature from a 3×10^{19} Zn-doped GaAs crystal which has a large surface trapping coefficient	101

SYMBOLS

c_{ℓ}	Elastic stiffness constant for longitudinal optical phonons.
$C_E(E)$	Escape coefficient (probability of escape upon striking the surface once).
$C_{ST}(E)$	Surface trapping coefficient.
$C_R(E)$	Reflection coefficient.
$Cs + (O+Cs)^n$	A surface treatment of an initial layer of cesium with 'n' additional oxygen-cesium layers.
D_{Γ}	Diffusion length of electrons thermalized in the Γ_1 minimum.
D_X	Diffusion length of electrons thermalized in the X_1 minima.
$D_{XX'}$	Coupling constant for equivalent intervalley scattering.
D_{12}	Coupling constant for scattering from Γ_1 to X_1.
E	Electron energy (all energies referred to the valence band maximum unless otherwise indicated).
E_x	Energy of the bottom of the X_1 conduction band minima.
E_{Γ}	Energy of the bottom of the Γ_1 conduction band minima.
f	Electron energy distribution function.
$f_n(E)$	Distribution function after n scattering events.
$f_{EMT}(E)$	Emitted distribution function.
$f_{OBS}(E)$	Experimentally observed distribution function.
$F_{EMT}(E)$	Emitted distribution function including thermalization in the X_1 minima.
F	Electric field strength.
F_{APP}	Applied electric field.
$F_{\perp}$	Perpendicular component of the extraneous field.
F_T	Total electric field.

$F_X(h\nu)$	Fraction of electrons assumed generated as thermalized in the X_1 minima.
$F_\Gamma(h\nu)$	Fraction of electrons assumed generated as thermalized in the Γ_1 minima.
$h = 2\pi\hbar$	Planck's constant.
$\hbar\omega_{opt}$	Optical phonon energy.
I	Incident light intensity per unit area.
J_X	Current density of electrons in X_1 flowing into the band-bending region.
J_Γ	Current density of electrons in Γ_1 flowing into the band-bending region.
k	Boltzman's constant.
$\bar{k}$	Electron wave vector.
ℓ_s	Hot electron scattering length.
L	Symmetry point at the edge of the Brillouin zone in the (111) direction.
L_T	Length an electron travels through the crystal (straight line distance from start to finish) while thermalizing.
L_X	Diffusion length in the X_1 minima.
L_Γ	Diffusion length in the Γ_1 minima.
$m_X^{(N)}$	Density of states effective mass for the X_1 minima.
m_X^*	Conductivity effective mass for the X_1 minima.
m_t	Transverse effective mass for the X_1 minima.
m_ℓ	Longitudinal effective mass for the X_1 minima.
N	Average number of scattering events required for thermalization.
$n_X(y)$	Electron density in the X_1 minima.
$n_\Gamma(y)$	Electron density in the Γ_1 minima.
P	Escape probability.

P_X	Escape probability for electrons in the X_1 minima.
P_Γ	Escape probability for electrons in the Γ_1 minima.
P_G	Probability of gaining energy during a scattering event.
P_L	Probability of loosing energy during a scattering event.
q	Electron charge.
$R(h\nu)$	Reflectivity.
T	Lattice temperature.
$u(x)$	Unit step function.
v	Electron velocity.
X	Symmetry point at the edge of the Brillouin zone in the (100) direction.
y	Distance into the crystal perpendicular to the cleaved surface.
Y	Yield (electrons per absorbed photon).
Y_X	Yield from electrons thermalized in the X_1 minima.
Y_Γ	Yield from electrons thermalized in the Γ_1 minima.
W	Width of the band-bending region.
$\alpha(h\nu)$	Optical absorption coefficient.
β	$\hbar\omega_{opt}/kT$.
ΔE_S	Average energy lost in a scattering event.
ΔE_T	Half amplitude width of a thermalized distribution.
ΔE_τ	Half amplitude width due to lifetime broadening.
Γ	Symmetry point in the center of the Brillouin zone at $\underline{k} = (000)$.
$\gamma(E)$ =	$E\,(1 + 0.576\,E - 0.050\,E^2 + \ldots)$ with E in eV referred to E_Γ (Ref. 6).
$\gamma'(E)$ =	$\frac{d}{dE}\,\gamma\,(E)$.
ρ	Density.

τ	Relaxation time.
$\tau_{\Gamma V}$	Recombination time for electrons in the Γ_1 minima.
$\tau_{X\Gamma}$	Relaxation time for scattering to the Γ_1 minima for electrons thermalized in the X_1 minima.
$\tau_{XX'}$	Scattering time for equivalent intervalley scattering.
$\langle\tau_X\rangle$	Average scattering time for electrons in the X_1 minima.
ω_{opt}	Optical phonon radian frequency.
Ξ_d	Dilation deformation potential.
Ξ_u	Uniaxial deformation potential.
Ξ_l	Longitudinal deformation potential.
Ξ_t	Transverse deformation potential.
μ	Mobility.
μ_{EIS}	Mobility for equivalent intervalley scattering.
μ_{po}	Mobility for polar optical scattering.
μ_A	Mobility for accoustic scattering.
μ_I	Mobility for impurity scattering.
$\mu_{X\Gamma}$	Mobility for nonequivalent intervalley scattering to Γ_1.
μ_X	Total mobility for electrons in the X_1 minima.

ACKNOWLEDGMENT

The author wishes to express his deep appreciation to Professor J. L. Moll for his expert guidance and support throughout the course of this work. Professor Moll's deep insight into physical problems has made working with him a very rewarding experience. Special thanks goes also to Professor W. E. Spicer for his encouragement and advice, and to all the graduate students with whom I have been associated for enriching my experiences while doing this work. Mr. Phil McKernan's work in constructing the cleaving chamber and liquid nitrogen cooled photoemission flange is especially appreciated. The author would also like to thank the Stanford University German Department who made it possible for him to take six months longer to finish his Ph.D. work than would otherwise have been possible.

Financial support was provided by the National Science Foundation and the U.S. Army, Ft. Belvoir, Virginia. Considerable use was made of the facilities provided by the Advanced Research Projects Agency through the Center for Materials Research at Stanford University.

I. INTRODUCTION

Since the original experimental work by Scheer and van Laar[1] which indicated that heavily doped GaAs cleaved in an ultrahigh vacuum and coated with cesium has a low enough work function to permit photoelectrons from all energies within the conduction band to escape, considerable interest has been shown in developing a practical photocathode using the GaAs-Cs system. This system shows promise of extremely high quantum efficiency since the escape length for electrons is determined by a diffusion length rather than a hot electron scattering length.

While eventual practical photocathodes will probably be made with other than vacuum-cleaved surfaces, it was felt that a thorough study of the photoemission from vacuum cleaved surfaces would eliminate the variable of surface preparation, and allow a detailed examination of the photoemission process in GaAs. In the process of this examination, new instrumentation allowing high resolution measurement of emitted electron energy distributions and their derivatives was developed, and played a critical role in making sufficient information available from experiment to allow the description of the photoemission process in terms of meaningful quantitative theories. In parallel with other laboratories, a process was developed for applying additional layers of oxygen and cesium to the surface, resulting in a lower vacuum level and an increased quantum efficiency.

This report covers in detail the methods and results of the experimental work conducted, and the theories which have been developed to explain the experimental results.

II. EXPERIMENTAL TECHNIQUES

A. THE BASIC EXPERIMENT

All of the photoemission experiments described in this report were performed in an ultrahigh vacuum cleaving chamber designed by Eden[21] and Baer[8] after the design of Powell.[19] This chamber is shown schematically in Fig. 1. A single crystal of commercially available p^+-type GaAs 1 cm square by 1-1/2 cm long is mounted on a movable rod, aligned such that the (110) face, the cleavage plane, faces the LiF window mounted on the front of the chamber.

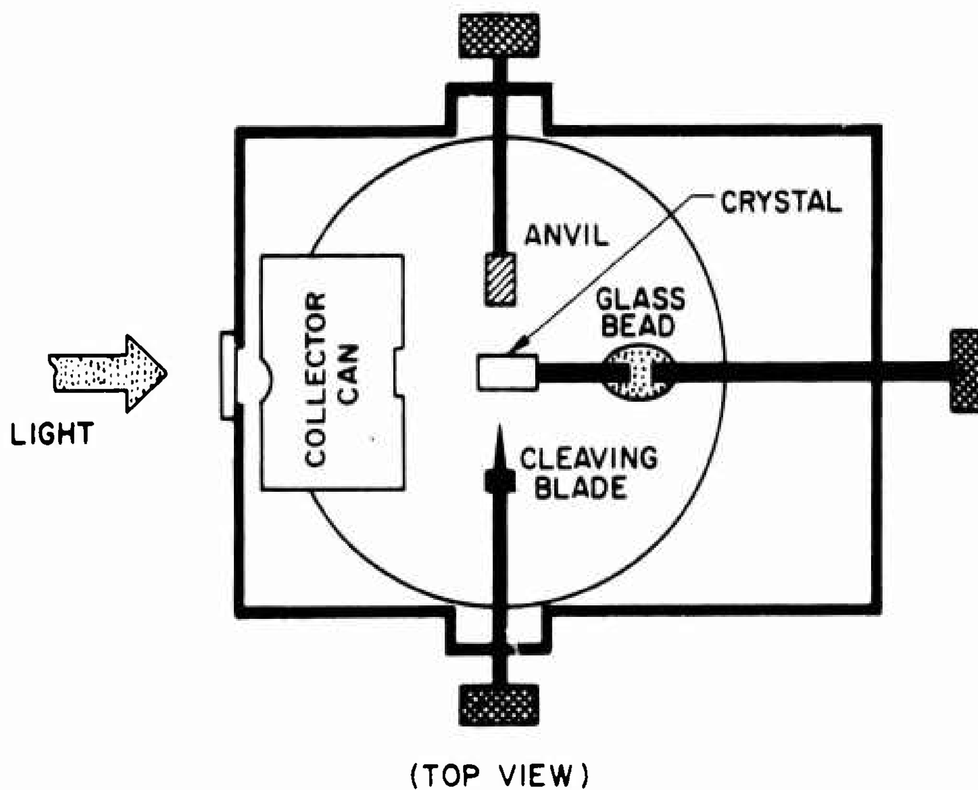

FIG. 1. Diagram of the ultrahigh vacuum cleaving chamber in which photocathodes are prepared and measured.

The chamber is then connected through a flexible vacuum connection to a roughing system consisting of three VacSorb® pumps and a small VacIon® pump. The VacSorb pumps are used in series to pump the chamber down to a pressure of 1 micron at which point they are valved off and the small VacIon pump is started. The chamber and the large Varian combination pump which is mounted directly below the chamber are baked at a temperature of 200°C for two days into the roughing station. At this point, the roughing station is valved off and the combination pump is started. The chamber is baked at 200°C into the combination pump for another day. All heaters for evaporation are outgassed immediately after this bakeout. The cesium channels used for cesiation are outgassed next. The chamber is allowed to pump down to a pressure of approximately 10^{-11} Torr after the outgassing procedures have been completed before an experiment is started. When this pressure has been reached, the crystal is moved into position between the tungsten carbide cleaving blade and the annealed copper anvil which are carefully aligned parallel to the (110) face. The anvil and blade are brought into position touching the sides of the crystal and then the pressure against the crystal is increased until it cleaves. The crystal is then cesiated and moved into the collector can where measurements can be made.

Figure 2 shows a picture of the actual chamber used with the experimental apparatus removed. The LiF window and the cleaving blade and anvil may be clearly seen. The experimental apparatus which mounts inside the chamber on the flange which has been removed in Fig. 2 is shown in Fig. 3. In this picture, the cleaved crystal and its holder are clearly visible. As can be seen, the cleave obtained is almost a

perfect mirror-like surface with a few lines running across it. The crystal holder is specially designed so that the crystal shields it from monochromator light. An ultrasonic tool is used to cut a cylindrical post on the back of the crystal by which the crystal is clamped. The large box-like structure below the crystal is used to catch the cleavage chip.

The collector can structure will be described in Section D. One of the two symmetrically mounted Cs channels discussed in the next section can be seen at the end of the collector can.

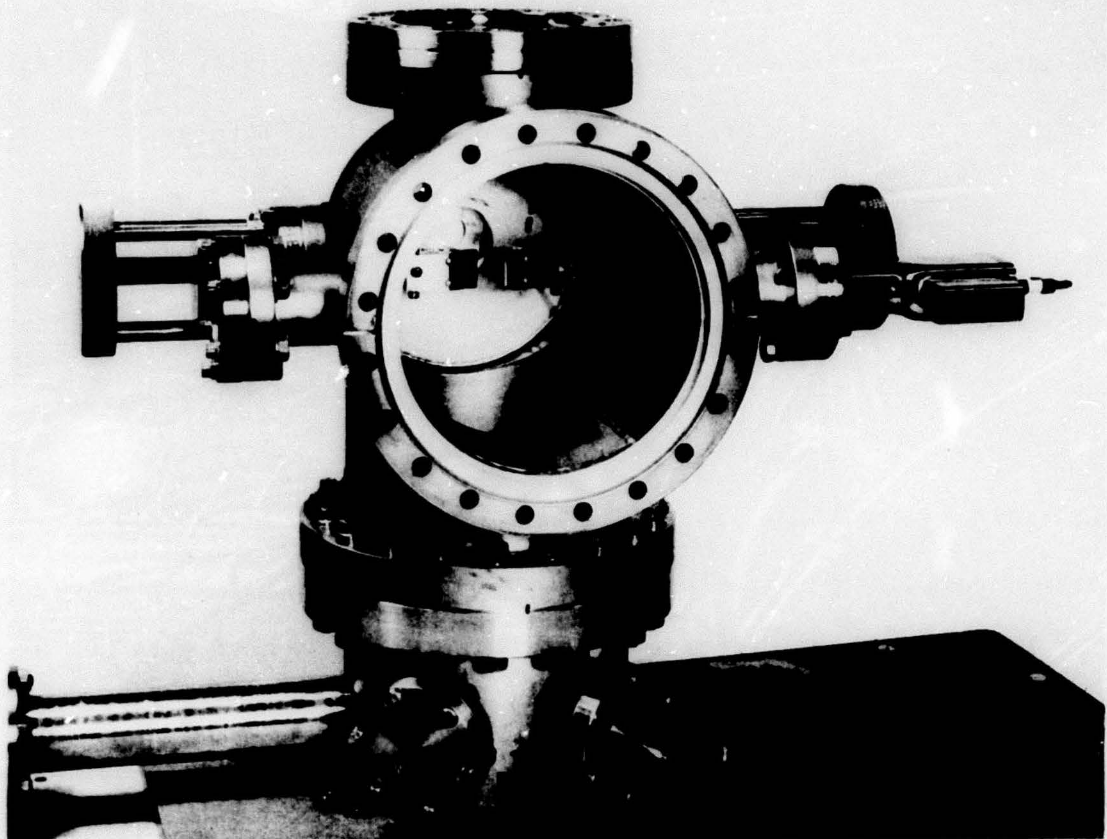

FIG. 2. Photograph of the chamber in which experiments were done.

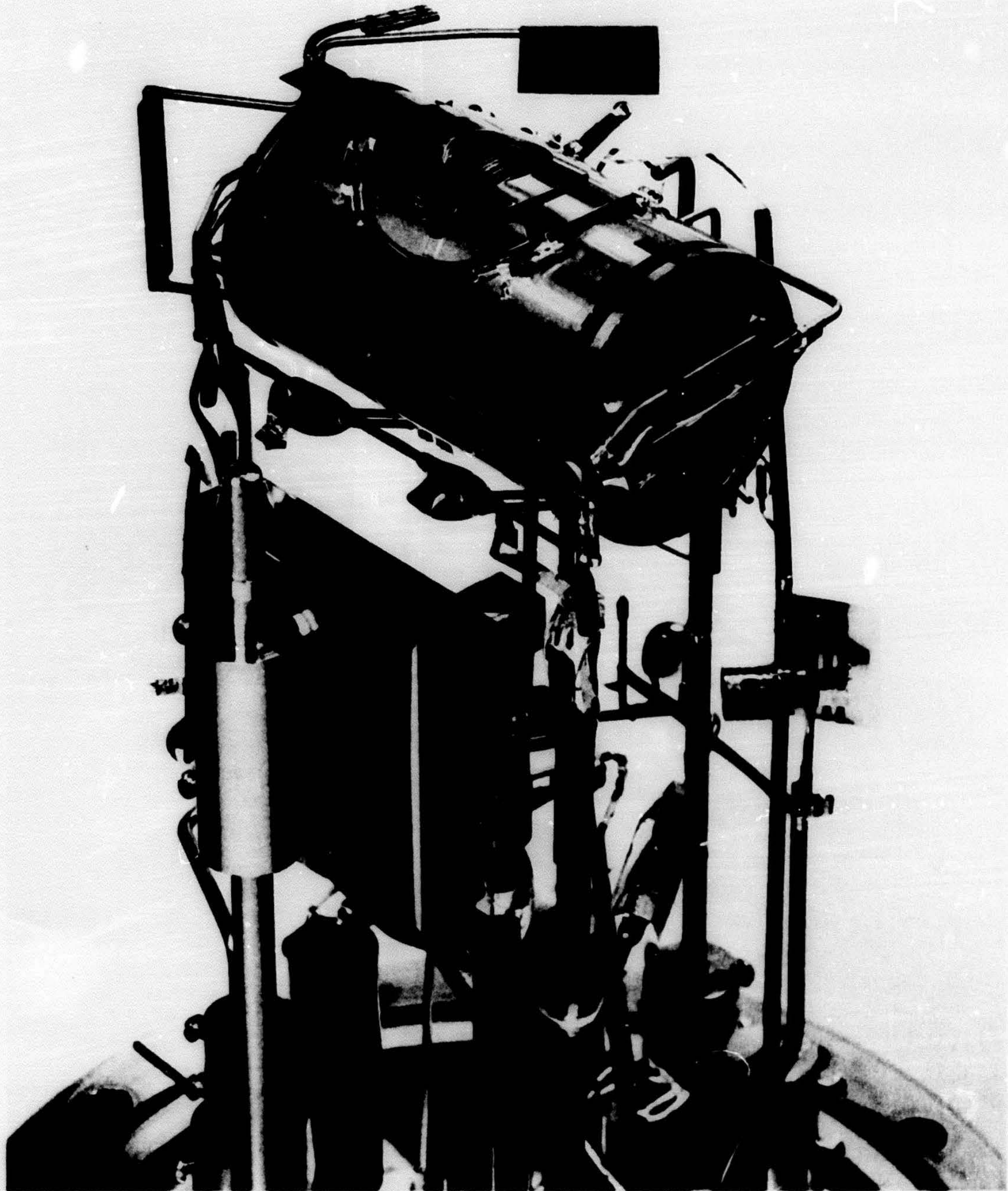

FIG. 3. Photograph of the flange from the chamber of Figure 2, showing the cleaved crystal in its holder and the collector can with ring structure and screen.

B. THE CESIATION PROCESS

Immediately after the crystal is cleaved, the cesiation process is started. Cesium chromate channels are used as a cesium source. A dim white light source (a #47 pilot lamp with 3 volts applied) is rigidly mounted to the flange outside the LiF window in the proper position to illuminate the crystal face. The photocurrent generated by this source is monitored during cesiation, using the circuit shown in Fig. 4. It is necessary to leave the cesium channels floating to prevent cesium ion current from affecting the photocurrent reading. If it is desirable to monitor the cesium ion current given off by the channels as an indication of the amount of cesium being given off, the cesium channels may be biased positive and the picoammeter connected to the collector can.

It should be emphasized that a very stable lamp mounting, a regulated lamp supply, and shielding from extraneous light are necessary to ensure that variations in photocurrent actually correspond to variations in photocathode sensitivity.

In early experiments, the crystal was placed inside the collector can and the entire chamber heated to 70°C to give the cesium enough mobility to uniformly coat the crystal and the inner collector can surfaces in a reasonable time. In more recent experiments with a modified collector can design, the chamber and the entire collector can structure are thoroughly cesiated by running the cesium channels for 12 hours with the chamber at room temperature before the crystal is cleaved. After cleaving, the crystal is cesiated at room temperature in a position behind the collector can, but still shielded from a direct view of the cesium channels. The cesiation is accomplished by passing a current

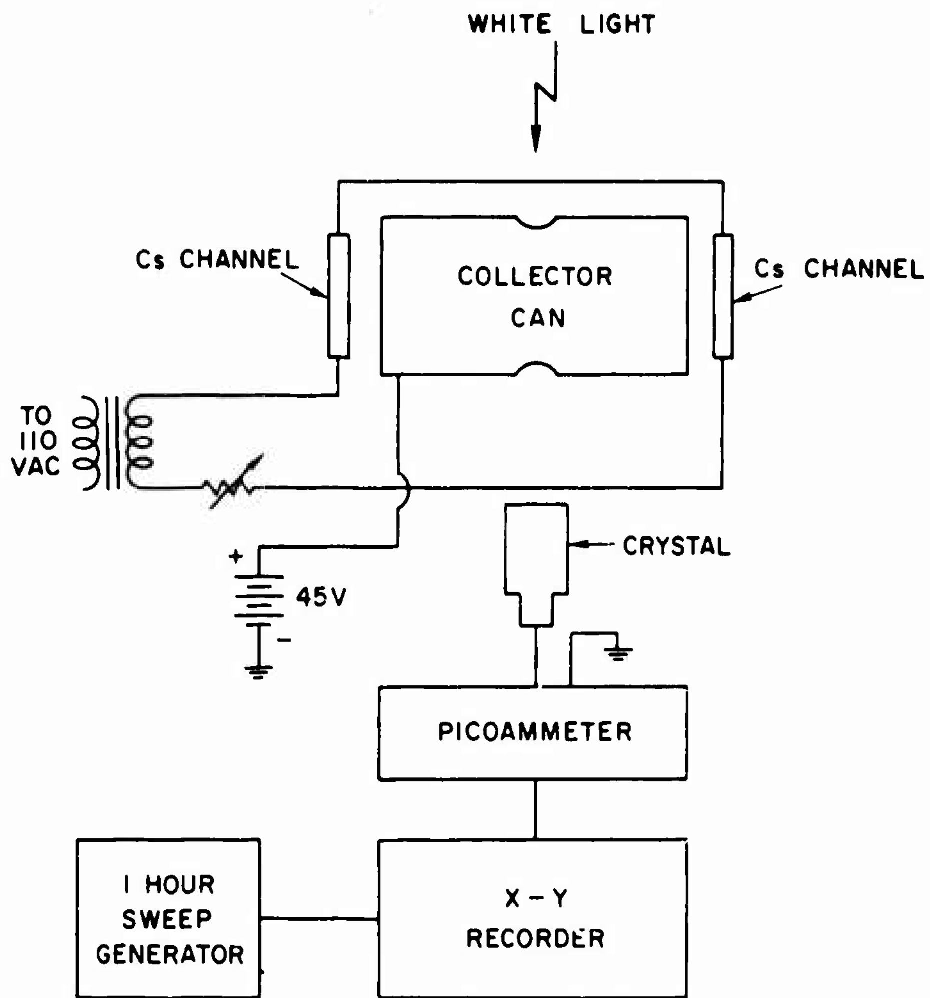

FIG. 4. Diagram of the connections used to monitor photocurrent during cesiation.

through the cesium channels to heat them until cesium is given off (approximately 6 amperes for the Varian channels used). The photocurrent from the white light source increases in approximately exponential fashion, doubling approximately every five minutes, until a maximum sensitivity peak is reached. The actual time required for optimum cesiation depends critically on the chamber geometry and crystal position. Beyond this peak the photocurrent drops slowly. By plotting photocurrent vs time on an X-Y recorder, it is easy to judge when the peak has been reached, and current through the cesium channels is turned off at this point.

For those samples treated with additional oxygen-cesium layers, after applying the first layer of cesium (as described above), oxygen is leaked into the chamber at a partial pressure of 2×10^{-8} Torr for a period of 20 minutes. During this time the photocurrent decreases. The oxygen supply is then turned off, and the chamber is allowed to pump back to a low pressure. After the photocurrent has stabilized, cesium is again applied until a peak in sensitivity is reached. This process gives an additional "oxygen-cesium layer," and may be repeated as many times as desired to obtain multiple oxygen-cesium layers, referred to as $(O+Cs)^n$ for n additional layers.

After moving the crystal into the collector can, detailed measurements can begin. Response of the photocathode to monochromatic light is measured in terms of the number of electrons emitter per absorbed photon at each photon energy (yield). The energy distribution curve (E.D.C.) of the emitted electrons is also measured at each photon energy.

C. CONSTRUCTION AND CALIBRATION OF A NEW REFERENCE TUBE FOR THE VISIBLE MONOCHROMATOR

In order to do a detailed study of the yield near threshold in GaAs, it was necessary to design and construct a new reference tube assembly for use in determining the monochrometer light intensity below 2.4 eV. Earlier GaAs yield measurements in the photon energy range below 4.0 eV were made by using the F-7 CsSb reference tube between 2.4 and 4.0 eV to measure the absolute level of illumination. Below this energy the yield was calculated by means of a ratio technique utilizing the absolute light output vs wavelength characteristics of the tungsten source-monochromator system as measured with an Eppley thermopile.[21] This method proved unsatisfactory for high accuracy measurements.

In order to overcome this deficiency a new secondary standard has been designed and constructed using a type 922 phototube. This tube has a type S-1 photocathode and has a useful yield from 1.2 eV to 4.0 eV, covering the entire range of interest in this work.

The standard and accompanying lens system are constructed to ensure that the entire monochromator output beam strikes the same portion of the reference tube's cathode and the center of the GaAs crystal in each experiment. This allows excellent repeatability, and is particularly useful when determining small changes in yield caused by varying the surface treatment of the GaAs crystal or other parameters.

A drawing of the reference tube and lens assembly is shown in Fig. 5. The reference tube is shown in the retracted position. When it is pushed into the monochromator beam by means of the outside handle, its position is accurately fixed. The rod guides were individually etched in nitric

acid until the rods would just slide freely in them, in order to keep the side play to an absolute minimum.

The mounting position for the quartz lens was choosen so that the entire monochromator beam would be intercepted by the lens. The focal length was choosen such that the monochromator beam is focused 4-1/4 inches in front of the front flange, ensuring that the entire beam hits the GaAs crystal, and allowing focusing of the beam to a small spot in the center of the crystal face when desired by mounting spacer rings between the reference assembly flange and the vacuum chamber, and closing down the slit width and height.

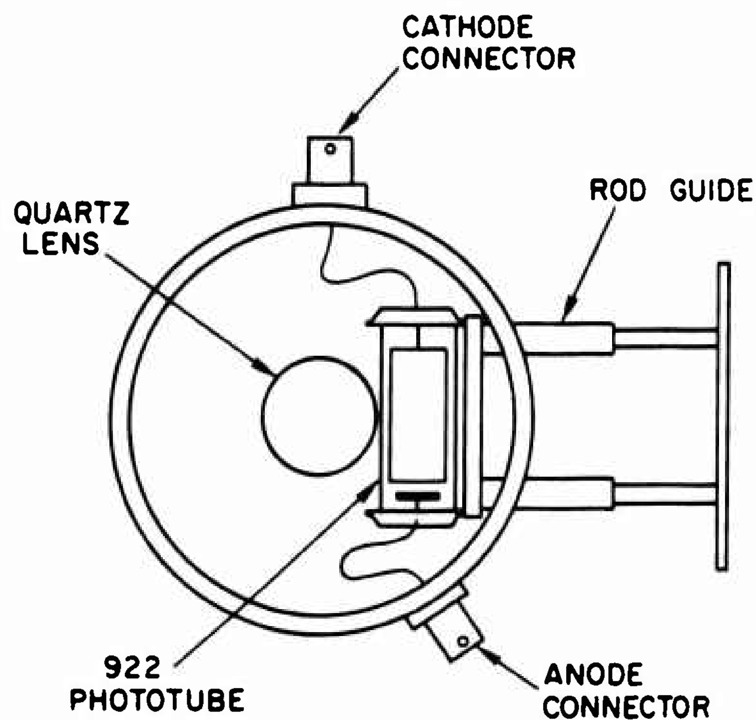

FIG. 5. Drawing of the reference tube assembly for the visible monochromator.

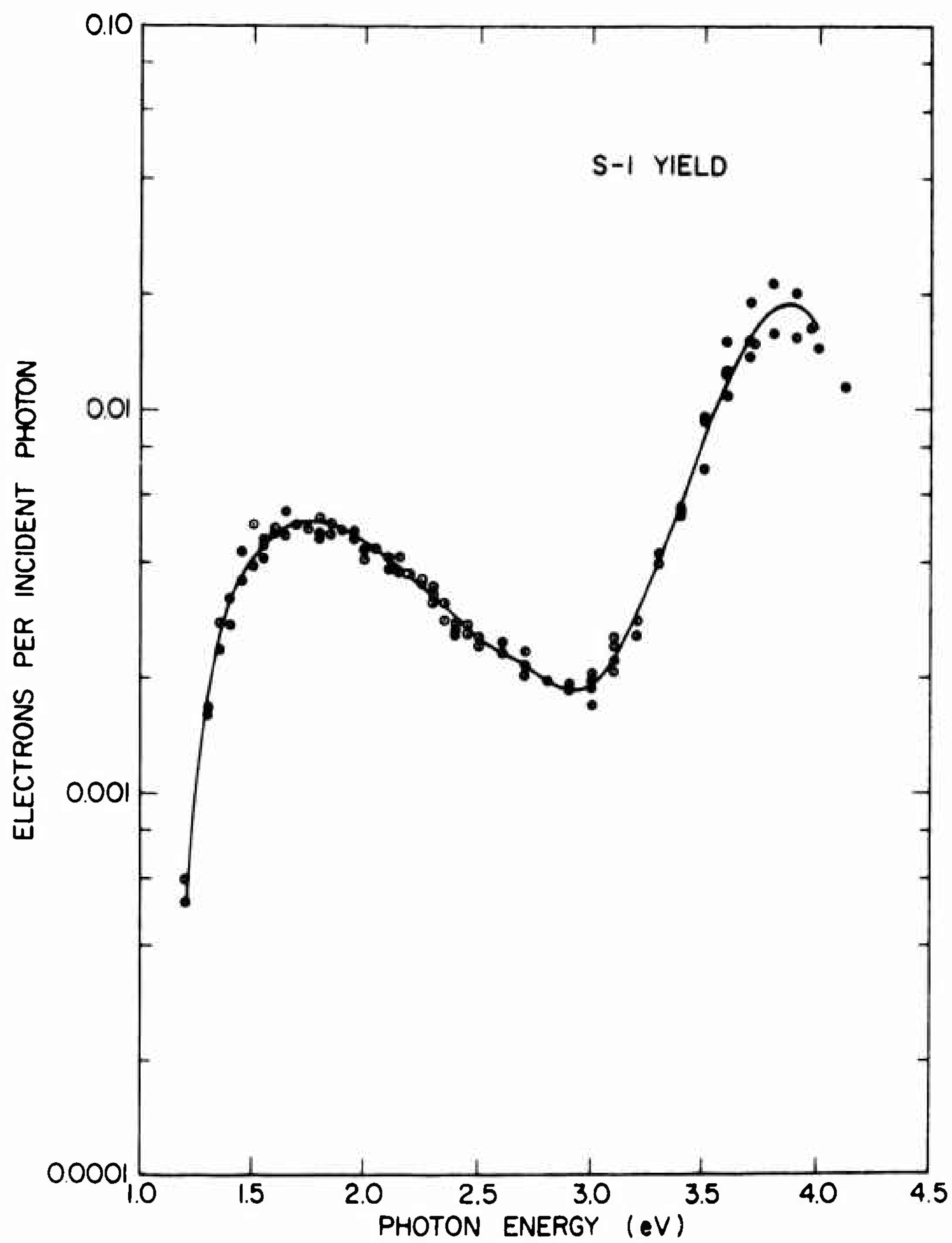

FIG. 6. Calibrated yield of the S-1 reference tube assembly, showing experimental points.

TABLE I

S-1 Reference Tube Yield

ENERGY (eV)	YIELD	ENERGY (eV)	YIELD
1.2	.00055	2.35	.0030
1.3	.00165	2.4	.0028
1.35	.00253	2.45	.0026
1.4	.0031	2.5	.00248
1.45	.0037	2.6	.00235
1.5	.0042	2.7	.00219
1.55	.0045	2.8	.00196
1.6	.0048	2.9	.00182
1.65	.0050	3.0	.00197
1.7	.0051	3.1	.00236
1.75	.0051	3.2	.00312
1.8	.0051	3.3	.0433
1.85	.0050	3.4	.00599
1.9	.0049	3.5	.00845
1.95	.0047	3.6	.0121
2.0	.0044	3.7	.0155
2.05	.0042	3.8	.0184
2.1	.0040	3.9	.0188
2.15	.00385	4.0	.0167
2.2	.0036	F-7 Calibration to Match	
2.25	.0034	4.0	.175
2.3	.0032	4.2	.170

The S-1 reference tube and lens assembly were calibrated as a unit using the Eppley thermopile over the entire range, and also by comparison with the most recent F-7 CsSb reference tube calibration above 3.0 eV. Figure 6 shows the apparent yield curve for the reference tube-lens assembly, along with a sample of the experimental data points taken to establish the curve. This calibration was done in January 1968. Table I gives the reference tube yield used in all yield calculations. The calibration was done using 70 volts on the S-1 anode and 1 mm x 5 mm slits on the visible monochromator, with the regulated tungsten source. The 922 phototube appears to be somewhat nonlinear at high light levels, so 1 mm x 5 mm slit settings should be used when making yield measurements with this calibration for best results.

D. REFINEMENTS IN ENERGY DISTRIBUTION CURVE MEASUREMENTS

1. Measurement of the Derivative of the Energy Distribution Curve

The experimental equipment used to measure the energy distribution curve and its derivative is shown in Fig. 7. A small 17.5 Hz ac voltage is applied in series with a variable retarding voltage. When the retarding voltage is increased, the collector can current decreases as the lower energy electrons are repelled from the collector can. The 17.5 Hz component of the collector can current is proportional to the derivative of the collector can current with respect to retarding voltage, as shown in "a" and "b" of Fig. 8. This is just the electron current in an incremental energy range, or the electron energy distribution curve. As shown at "c" in Fig. 8, when there is a curvature in the current-retarding voltage curve, the ac current waveform is distorted from the sinusoidal input voltage. This distorted waveform may be decomposed into

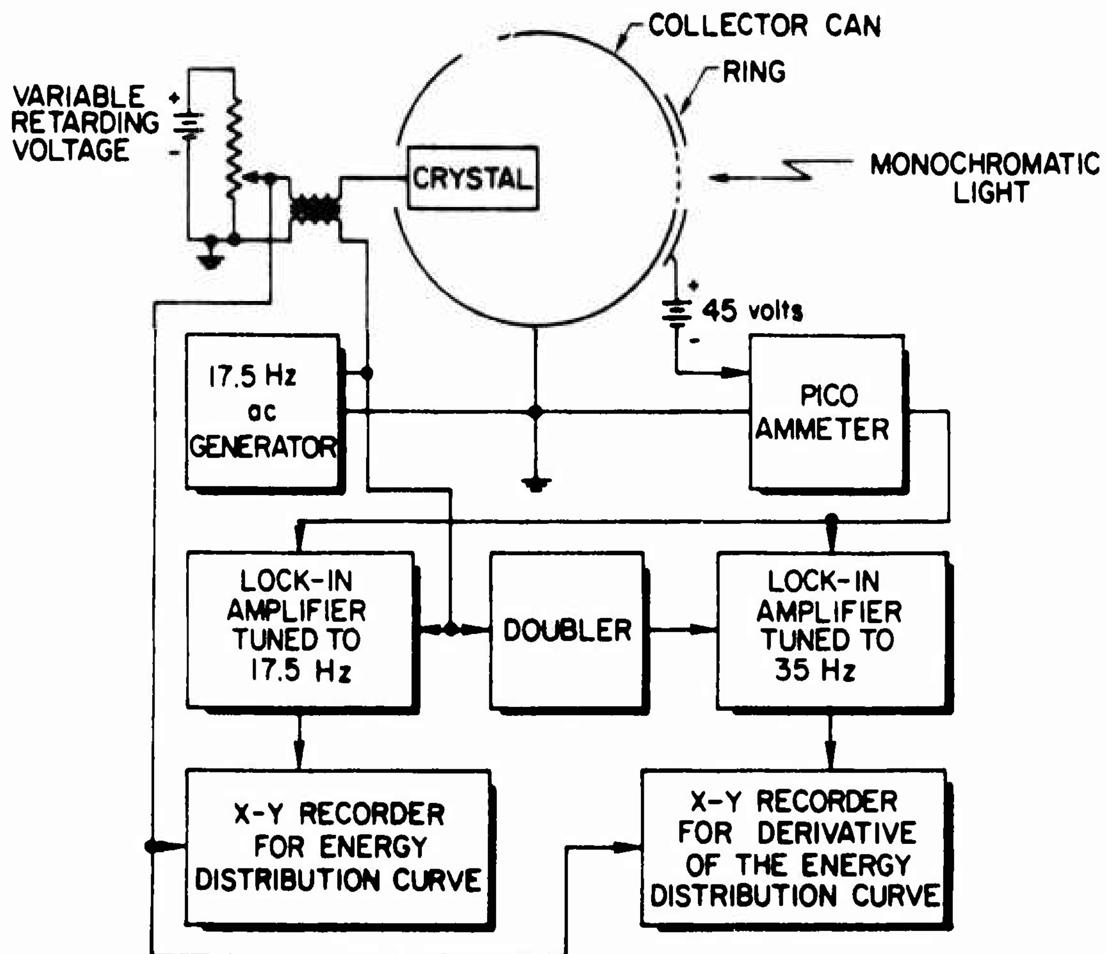

FIG. 7. Experimental apparatus used to measure the energy distribution curve and its derivative.

the fundamental (17.5 Hz) and harmonic components. The second harmonic (35 Hz) component of the collector can current is proportional to the second derivative (the rate of curvature) of the collector can current with respect to retarding voltage, or the derivative of the energy distribution curve. Lock-in amplifiers tuned to the fundamental and second harmonic of the 17.5 Hz reference voltage provide low noise recordings of the energy distribution curve and its derivative.

It should be noted that the voltage amplitude of the fundamental component is proportional to

$$\left(\frac{\text{reference voltage}}{\text{can structure resolution}}\right),$$

whereas the voltage amplitude of the second harmonic component is proportional to

$$\left(\frac{\text{reference voltage}}{\text{can structure resolution}}\right)^2 .^*$$

Thus a high resolution can structure is particularly helpful in obtaining meaninful and low noise derivative curves.

In many cases it is advantageous to increase the gain and obtain magnified curves for the high energy "tail" of the E.D.C. and its derivative. In these cases, a low noise recording may be obtained by increasing the integration time constant and the sweep time used to record one curve.

The principal advantages of measuring the derivative of the energy distribution curve as well as the E.D.C. are the more accurate location of structure and the possibility of seeing structure not capable of being observed on the E.D.C. Note at "b" in Fig. 8 that the zero

---

* This is strictly true only for ac voltages less than the width of the structure being measured, and for structure which is narrower than the resolution of the can structure.

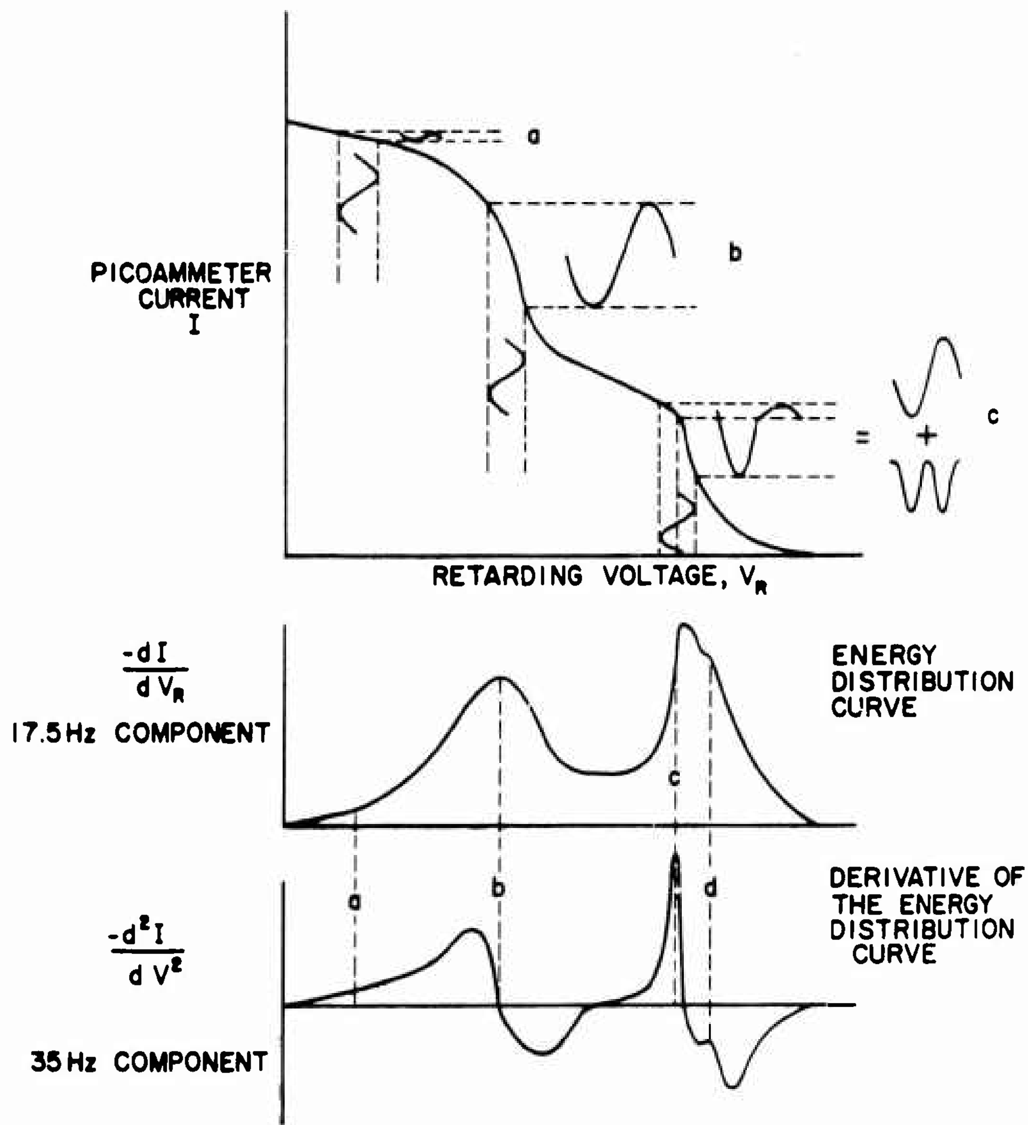

FIG. 8. Principle of operation of the ac technique for measuring the energy distribution curve and its derivative.

crossing is at a sharp angle and may be more easily accurately located than the top of the peak in the E.D.C. Notice also near "b" the approximately symmetrical structure on each side of the zero crossing. This symmetrical structure is present also for structure which is not fully resolved on the E.D.C. At "d" in Fig. 8, the exact position of the shoulder on the E.D.C. is very difficult to determine. However, the center of the symmetrical structure (in this case about the larger curve rather than the zero axis) may be easily located accurately. Figure 9 shows actual experimental data demonstrating these principles.

2. Resolution Improvements

With the majority of energy distribution curve (E.D.C.) measurements, the current level is so low that the important considerations in getting the best possible curves are elimination of input noise to the picoammeter from vibration and electrical pickup, and realizing the proper trade-off between resolution and signal level as determined by the slit width and ac voltage amplitude. For a complete discussion of the factors involved, see Eden's thesis.[21]

With a high yield material such as cesiated GaAs in the visible photon energy range, sufficient current is available that many of these factors are no longer significant. Both the slit width and the ac voltage amplitude may be reduced to the point where their effects on resolution may be ignored without a serious deterioration of the signal-to-noise ratio of the energy distribution curve.* Typical curves were measured

* The principal noise source at high photocurrent levels was variation in the source lamp intensity, but that was eliminated by constructing a current regulated power supply for the monochromator source tungsten lamp, giving highly reproducible and practically noise-free E.D.C.'s throughout the visible range.

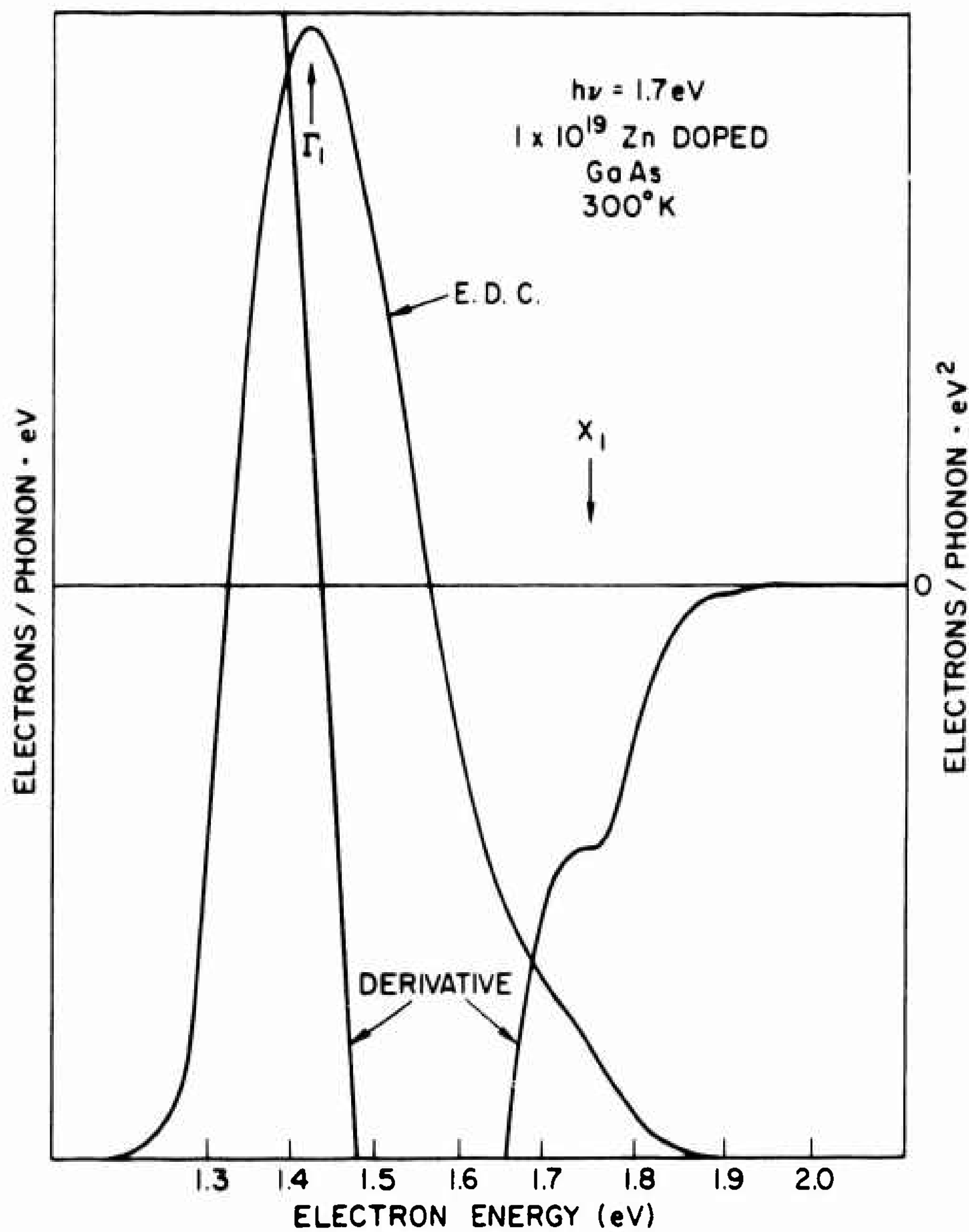

FIG. 9. Experimental E.D.C. and derivative curves for a photon energy of 1.7 eV. Notice that the location of the X_1 minima (marked from its location on an E.D.C. taken with a higher photon energy) is easy to locate exactly on the derivative curve. On the E.D.C. itself, it is difficult for the untrained eye to even determine that a definite structure appears on the high energy shoulder, let alone determine its energy accurately.

using 0.2 mm slit width and 0.01 volt peak-to-peak reference voltage. Thus the resolution is determined by the crystal and can structure.

Several factors within the crystal and can structure are responsible for decreasing the resolution. These factors, and the steps taken to minimize them will be covered next.

The ideal electron energy distribution measurement apparatus would provide a retarding potential such that the gradient of the potential would be parallel to the electron momentum vector at all points. A structure providing such a potential would be a point source emitter at the center of a spherical collector can coated with a uniform work function material. The collector can structure actually used is an approximation to this structure. The cylindrical collector can used is shown in Fig. 3. Similar cans have been used in the past. This can is larger than the earlier cans, giving a closer approximation to the ideal structure. A mesh screen is placed across the light entrance hole to provide a continuation of the equipotential surface across the hole. In earlier experiments, electrons coming through the hole produced a negative charge on the LiF window, producing a retarding field which extended into the can. The screen greatly reduced this effect.

An electric field exists between the edges of the GaAs crystal and the face, due to the difference in work function between the sawed and the cleaved surfaces. This field is reduced, but not entirely eliminated, by evaporating Cu on the sides of the crystal before cleaving. The work function of cesiated copper (1.5 eV)[22] is lower than the work function of cesiated "dirty" GaAs (approximately 2.0 eV). The monochromator beam is focused to a small spot in the center of the crystal

face to further reduce the effect of this field.

A collector ring is placed around the screened hole in the front of the can and biased 22-1/2 volts positive with respect to the can. This ring collects those electrons which come through the screened hole. By measuring only the current collected by this ring instead of the entire collector can current, an increase in resolution is obtained. This current travels very near a path inside the collector can which is a two-fold symmetry axis for the electric field. This arrangement prevents appreciable transfer of translational to angular momentum. Also, small variations in work function on the wires of the screen will be averaged out as seen by an electron passing between wires. It has been experimentally determined that for excitation with photons below 4 eV and proper placement of the crystal in the collect can as determined by comparison of E.D.C.'s, the ring current is an accurate sample of the total collector can current. At higher photon energies there may be problems caused by high energy electrons coming through the screen which are not collected by the ring. The amplitude of the ring current E.D.C.'s should be carefully checked against emitted current E.D.C.'s. With proper collector can design, and a uniform copper evaporation and cesiation of the inside of the can, excellent resolution (such as is seen in Fig. 37) is possible without using the ring. This approach is highly recommended.

The increased resolution obtained through these steps allows more accurate location of structure in the distribution, makes possible the observation of structure not previously observed, and allows a more accurate separation of the total yield into its components.

Figure 10 shows a typical set of experimental energy distribution curves using the ring current taken at room temperature for a range of photon energies from 1.4 to 3.0 eV.

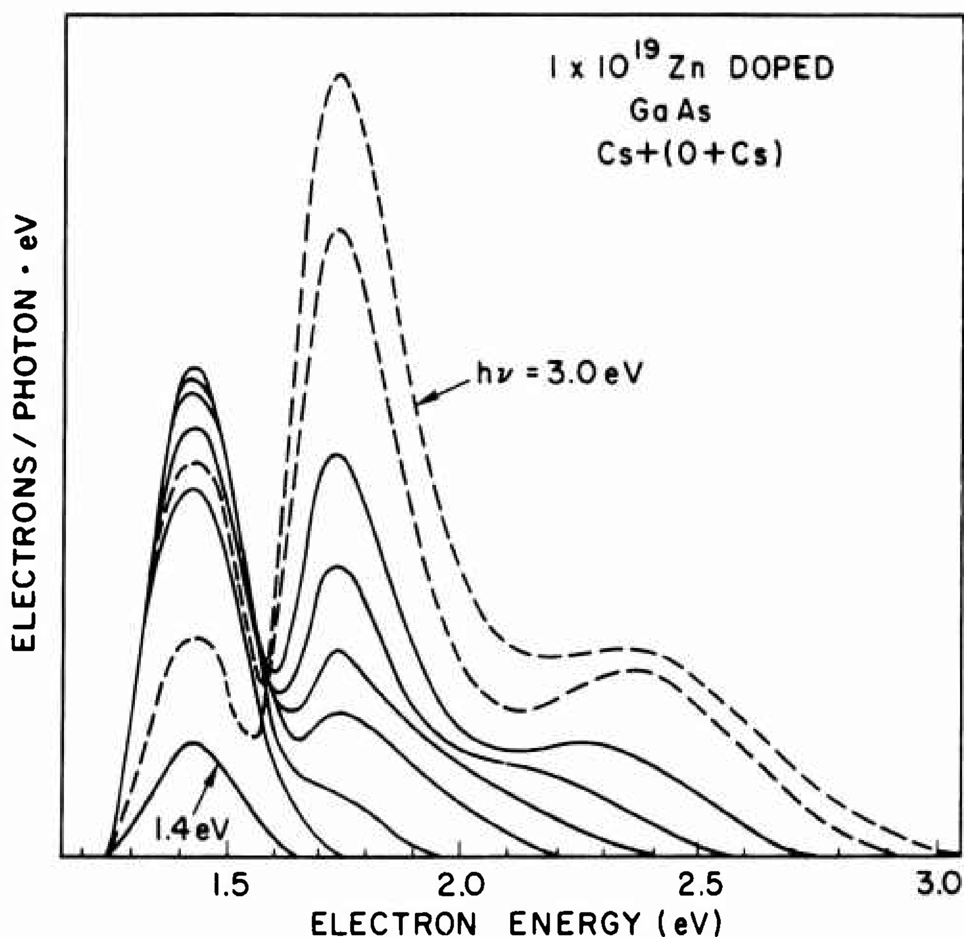

FIG. 10. Normalized and smoothed experimental energy distribution curves for a 1 x $10^{19}/cm^3$ Zn-doped GaAs crystal with a Cs + (O+Cs) surface treatment shown for increments of 0.2 eV for a photon energy range of 1.4 eV to 3.0 eV. The 2.8 eV and 3.0 eV curves are shown dotted for clarity.

III. THE TWO MINIMA DIFFUSION MODEL FOR PHOTOEMISSION NEAR THRESHOLD

Figure 11 shows a band diagram for a p^+ GaAs crystal coated with a layer of cesium. The bands are bent near the surface and the work function is lowered sufficiently that the vacuum level is below the bottom of the conduction band in the bulk of the material. Near threshold the absorption coefficient for light is small enough that only a few percent of the light is absorbed in the band bending region, and almost all photoexcitation takes place in the bulk of the material. The hot-electron scattering length is also short compared with the optical absorption length, so that photoexcited electrons thermalize in a conduction band minima, then diffuse to the band bending region where they are accelerated toward the surface and emitted.

Figure 12 shows a band structure for GaAs near the band gap. Photoexcitation in this material requires conservation of k-vector and energy, giving vertical transitions between states in the valence bands and states in the conduction bands which differ in energy by $h\nu$, where $h\nu$ is the photon energy. Photoexcited electrons will have a range of final energies which could in principle be determined accurately from a knowledge of the band structure and optical-transition matrix elements throughout the Brillouin zone. Rather than work with the actual final excited energy distribution, we will make approximations at this point.

For low photon energies, such as shown at "a" in Figure 12, all photoexcitation will be to final states lower in energy than the X_1 minima and thermalization will occur into the Γ_1 minima. For higher

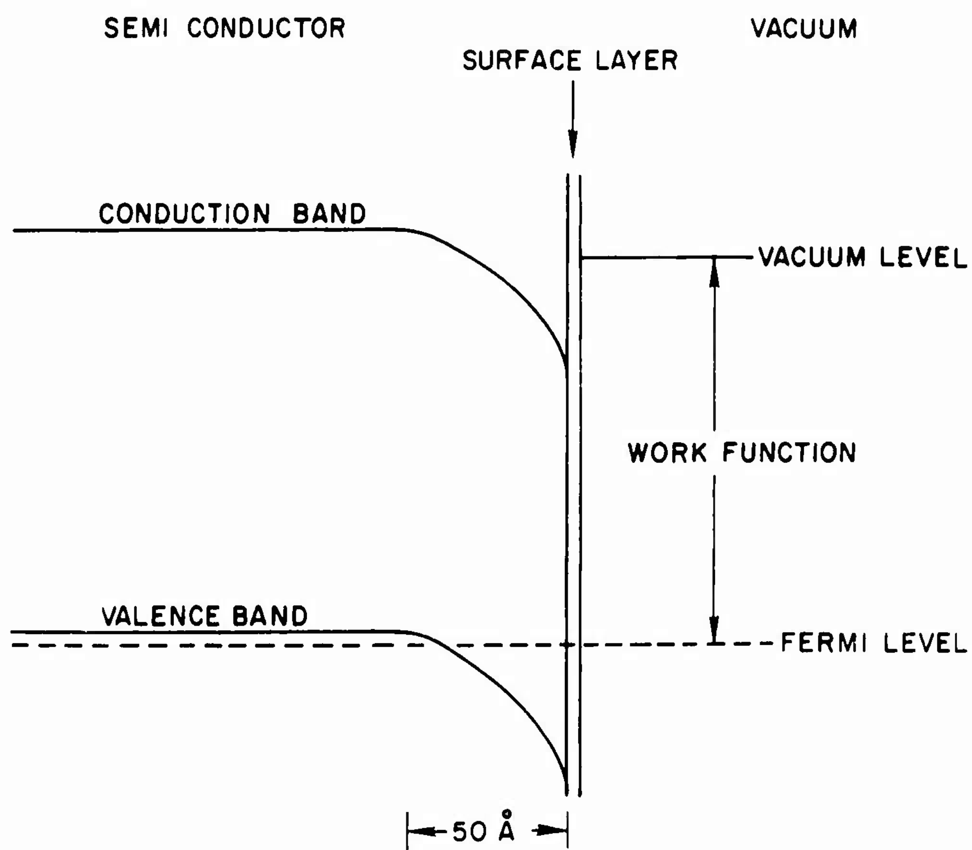

FIG. 11. Band-bending diagram showing the effects of a layer of cesium applied to a p^+ GaAs surface.

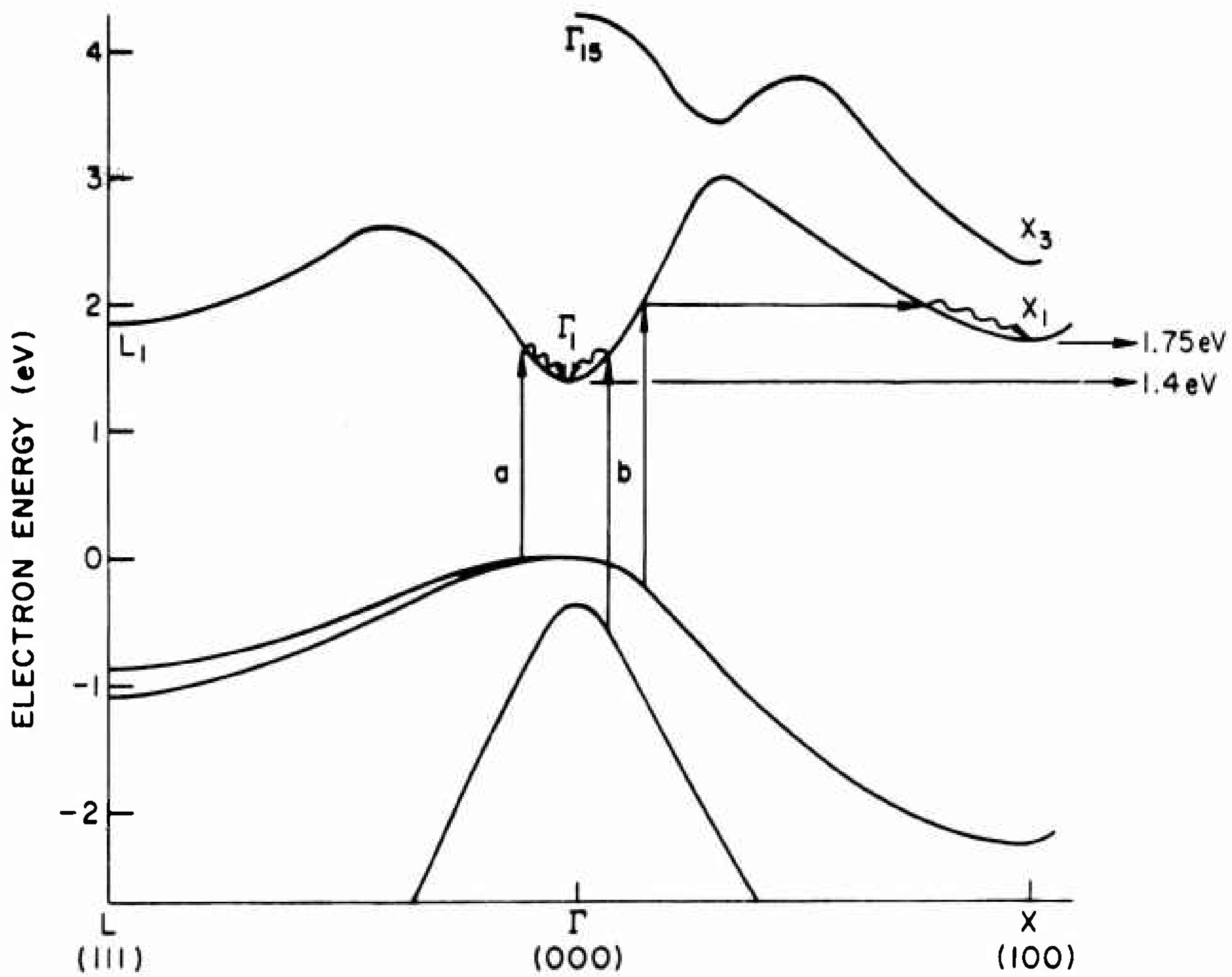

FIG. 12. GaAs band structure near the energy gap showing examples of photoexcitation, scattering, and thermalization in the Γ_1 and X_1 minima. For photon energies below 1.75 eV ("a"), all electrons thermalize in the Γ_1 minima. Above 1.75 eV ("b"), some electrons are excited to a high enough energy to thermalize in X_1.

photon energies, such as shown at b, some excitation will be to energies above 1.75 eV and some to energies below 1.75 eV. An electron excited above 1.75 eV will rapidly scatter into X_1 and thermalize there,[2] due to the higher density of states in X and the value of the coupling coefficient for Γ_1 to X_1 scattering. The fraction which is excited to energies greater than 1.75 eV will be defined as F_X. These electrons are assumed to travel only a very short distance through the crystal before thermalizing in X. The remaining fraction of excited electrons, F_Γ, are assumed to rapidly thermalize in the Γ minima. F_Γ and F_X are shown in Fig. 13.

Above the band gap, F_X and F_Γ were determined by a graphical construction taking into account energy and k-vector conserving transitions from the highest three valence bands to the lowest conduction band. The graphical construction was done using equal energy contours for these four bands in the 110 and 100 planes obtained from Herman's band structure calculation[3] such as are shown in Figs. 14 and 15. Corrections were included for spin-orbit splitting, X-Γ spacing, and band tailing. Constant matrix elements were assumed for transitions from the highest two valence bands, while the matrix elements for transitions from the third highest valence band were assumed to be a factor of 3 smaller. It should be noted that while the shape of these curves are qualitatively correct, the actual numbers must be considered approximate due to the assumption of constant matrix elements, the use of only two planes rather than the entire Brillouin zone, the approximate nature of the graphical technique

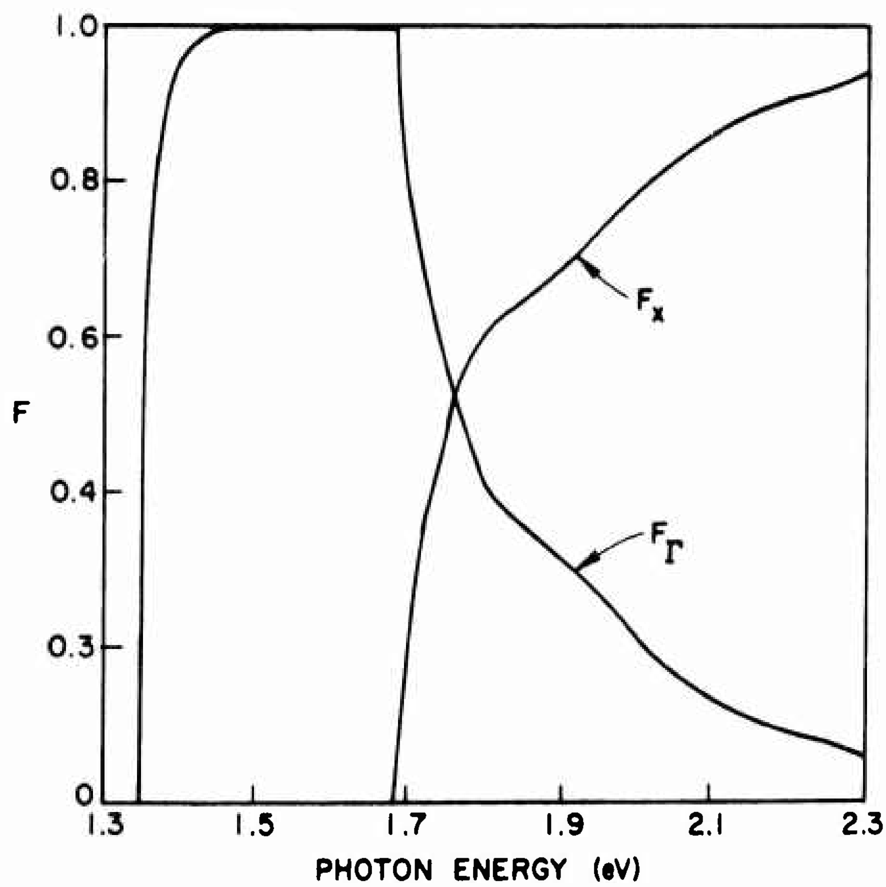

FIG. 13. Fraction of photoexcited electrons which thermalize in each minima, calculated from the GaAs band structure, corrected for the presence of an impurity band.

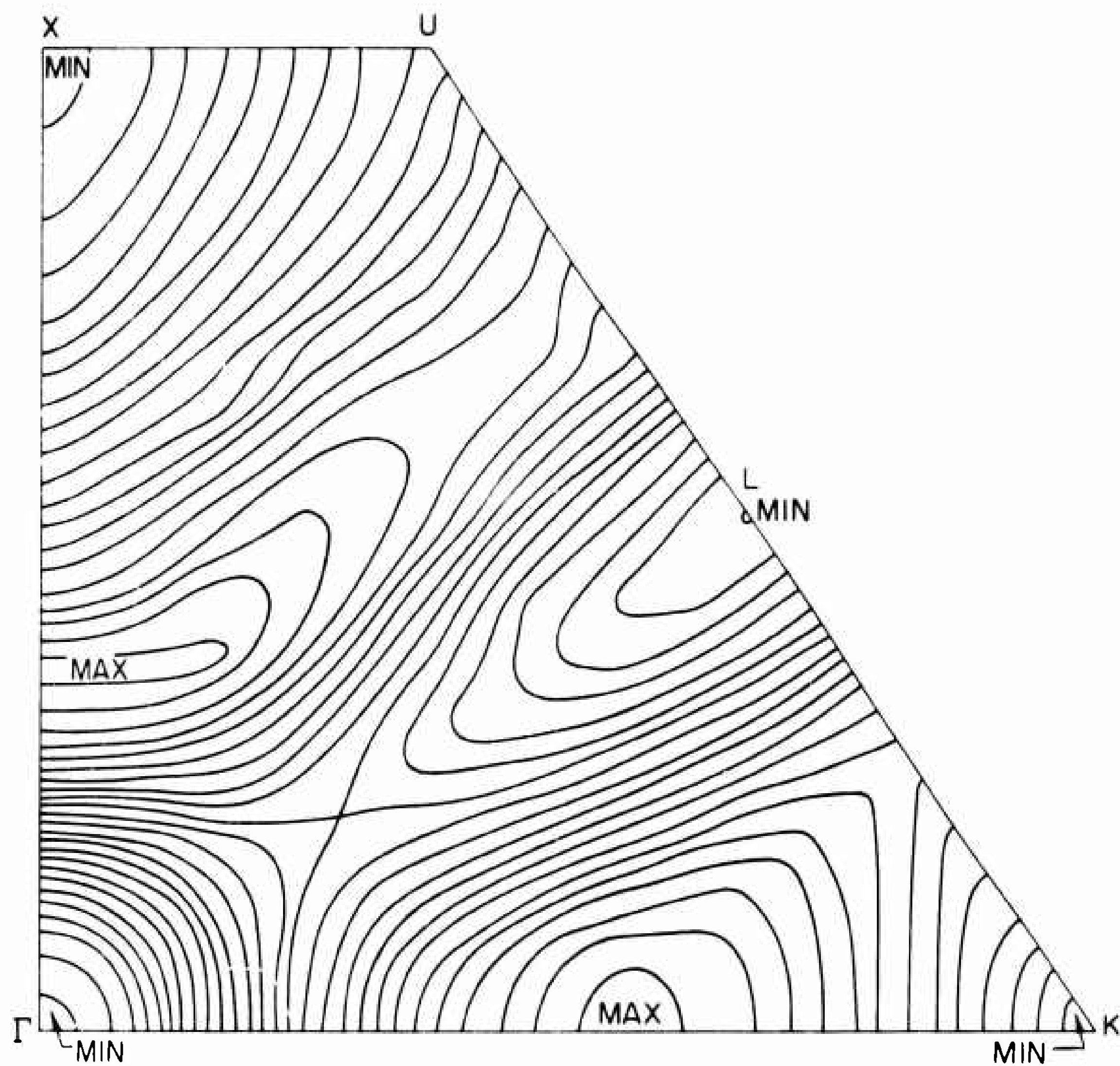

FIG. 14. Equal energy contours (0.2 eV spacing) for the first conduction band in GaAs in the (110) plane in the Brillouin zone from Herman.[5]

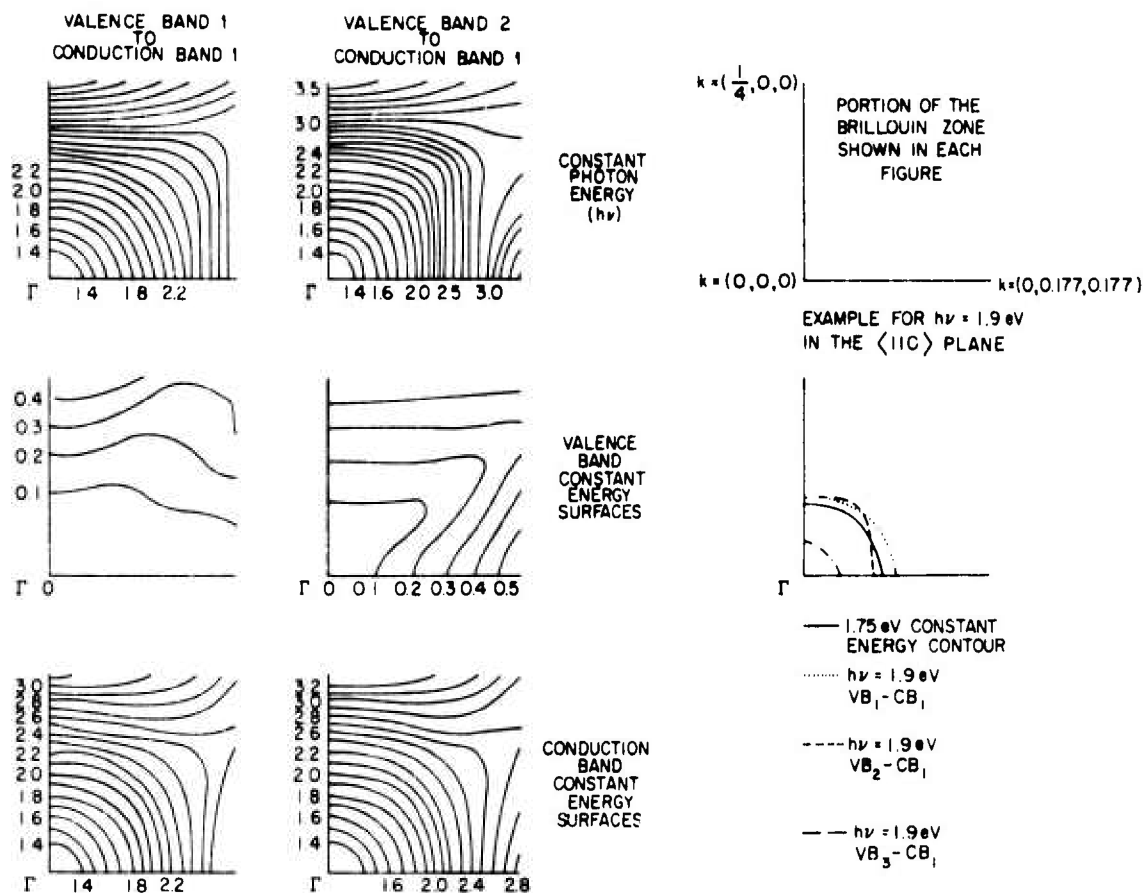

FIG. 15. Equal energy contours in one plane near the center of the Brillouin zone, illustrating the method used to find F_X and F_Γ. In the left two columns, equal energy contours for a valence band and a conduction band are shown along with equal photon energy lines obtained by subtracting the values of the bands at each point. On the right, the energy surface in the conduction band above which scattering to X_1 occurs is shown along with the constant photon energy curves for a photon energy of 1.9 eV for transitions to the lowest conduction band from the highest three valence bands. In this plane, all electrons excited from the highest valence band are included in F_X, 1/4 of the electrons excited from the second highest valence band are included in F_Γ and 3/4 in F_X, and all electrons excited from the third highest valence band are included in F_Γ. For reasons of space and clarity the third highest valence band equal energy contours are not shown. This third band is the light hole band which is 0.32 eV below the other two valence bands at k = (000) (spin-orbit splitting).[5]

used, and the possible errors in the band structure calculation. The major effect of changes in these numbers is to change the X diffusion length as calculated later. Below the band gap F_Γ drops below unity as a significant fraction of the photons are absorbed by free carriers (holes) rather than by band-to-band transitions.[4]

Examination of the experimental energy distribution curves shows that for photon energies from threshold at 1.4 eV (near-infrared) to 2.3 eV (blue-green) almost all emitted electrons are thermalized in either the Γ_1 or X_1 minima, while for higher photon energies a significant number of higher energy, unthermalized electrons may be seen in the distribution. Also, above 2.3 eV, α becomes large enough that excitation in the band bending region may no longer be neglected. Below 2.3 eV we need to consider only those electrons generated in the bulk crystal, and these are assumed to be thermalized in either the Γ or X minima, so we may solve for electron transport in terms of the one-dimensional coupled diffusion equations for these minima.

$$-D_\Gamma \frac{\partial^2 n_\Gamma}{\partial y^2} + \frac{n_\Gamma}{\tau_{\Gamma V}} = \frac{n_X}{\tau_{X\Gamma}} + I(1 - R)F_\Gamma \alpha e^{-\alpha y} \qquad (\Gamma \text{ equation}) \qquad (3.1)$$

$$-D_X \frac{\partial^2 n_X}{\partial y^2} + \frac{n_X}{\tau_{X\Gamma}} = I(1 - R)F_X \alpha e^{-\alpha y} \qquad (X \text{ equation}) \qquad (3.2)$$

where y is the distance into the crystal.

The first term in each equation is the diffusion term where D is the diffusion coefficient. The second term is the rate at which carriers are lost from each minima. $\tau_{\Gamma V}$ is the recombination time from the Γ minima to

the valence band (or to traps). $\tau_{X\Gamma}$ is the relaxation time for scattering from the X_1 minima to the Γ_1 minima. $n_X/\tau_{X\Gamma}$ is a rate of generation term in the Γ equation as well as a rate of loss term in the X equation. The last term is the rate of generation by photoexcitation, where I is the incident light intensity, R is the reflectivity, and α is the optical absorption coefficient. The assumptions implicit in writing these equations are that there is no recombination from X directly to the valence band, and that the distance an electron travels through the crystal while thermalizing is short compared with $(1/\alpha)$ and the diffusion lengths.

Using the band bending region as a boundary condition, we may solve these equations for the current density flowing into the band bending region, giving

$$J_X = \frac{qI(1 - R)F_X}{1 + 1/\alpha L_X} \tag{3.3}$$

and

$$J_\Gamma = \frac{qI(1 - R)}{1 + 1/\alpha L_\Gamma}\left[F_\Gamma + \frac{F_X L_\Gamma}{\alpha L_X (L_\Gamma + L_X)(1 + 1/\alpha L_X)}\right] \tag{3.4}$$

where the diffusion lengths are given by

$$L_X = \sqrt{D_X \tau_{X\Gamma}} \tag{3.5}$$

$$L_\Gamma = \sqrt{D_\Gamma \tau_{\Gamma V}} \quad . \tag{3.6}$$

Of that current flowing into the band-bending region, a certain fraction, given by the escape probability P, will be emitted into the vacuum. P will be a function of both surface treatment and electron energy. The photoelectric quantum efficiency, or yield, is then given for each minima by

$$Y_X = \frac{P_X J_X}{qI(1 - R)} = \frac{P_X F_X}{1 + 1/\alpha L_X} \qquad (3.7)$$

$$Y_\Gamma = \frac{P_\Gamma J_\Gamma}{qI(1 - R)} = \frac{P_\Gamma}{1 + 1/\alpha L_\Gamma} \left[F_\Gamma + \frac{F_X L_\Gamma}{\alpha L_X (L_\Gamma + L_X)(1 + 1/\alpha L_X)} \right]. \qquad (3.8)$$

Everything is known in these equations except the diffusion lengths, L_X and L_Γ, and the escape probabilities, P_X and P_Γ. The X and Γ yields may be obtained experimentally from the energy distribution curves. Examining the yield equations, we see that the magnitude of the yield vs photon energy curves is determined by the escape probability, while the shape of the curves is determined by the diffusion length. Thus P_X and L_X may be determined uniquely from the experimental X yield curve, and P_Γ and L_Γ may be obtained from the Γ yield curve. Figure 16 and the solid curve in Fig. 17 indicate the match between theory and experiment for the X and Γ minima respectively, where the points are room temperature experimental data for a $1 \times 10^{19}/cm^3$ Zn-doped crystal, vacuum cleaved and coated with cesium plus an additional oxygen-cesium layer; and the solid curves are plots of the theoretical yield equations using the parameters $P_\Gamma = .18$, $L_\Gamma = 1.573$ microns, $P_X = .54$, $L_X = .03$ microns. α is shown in Fig. 18.[4,21] Some changes in α with doping density[27] are expected.

For this theory to be physically meaningful, the diffusion length should be a property of the bulk crystal, while the escape probability should be a function of surface treatment. That this is in fact the case is shown in Fig. 19 where the match between theory and experiment is shown for various surface treatments on the same crystal. All theoretical curves use the same diffusion length of 1.573 microns, while the escape probability

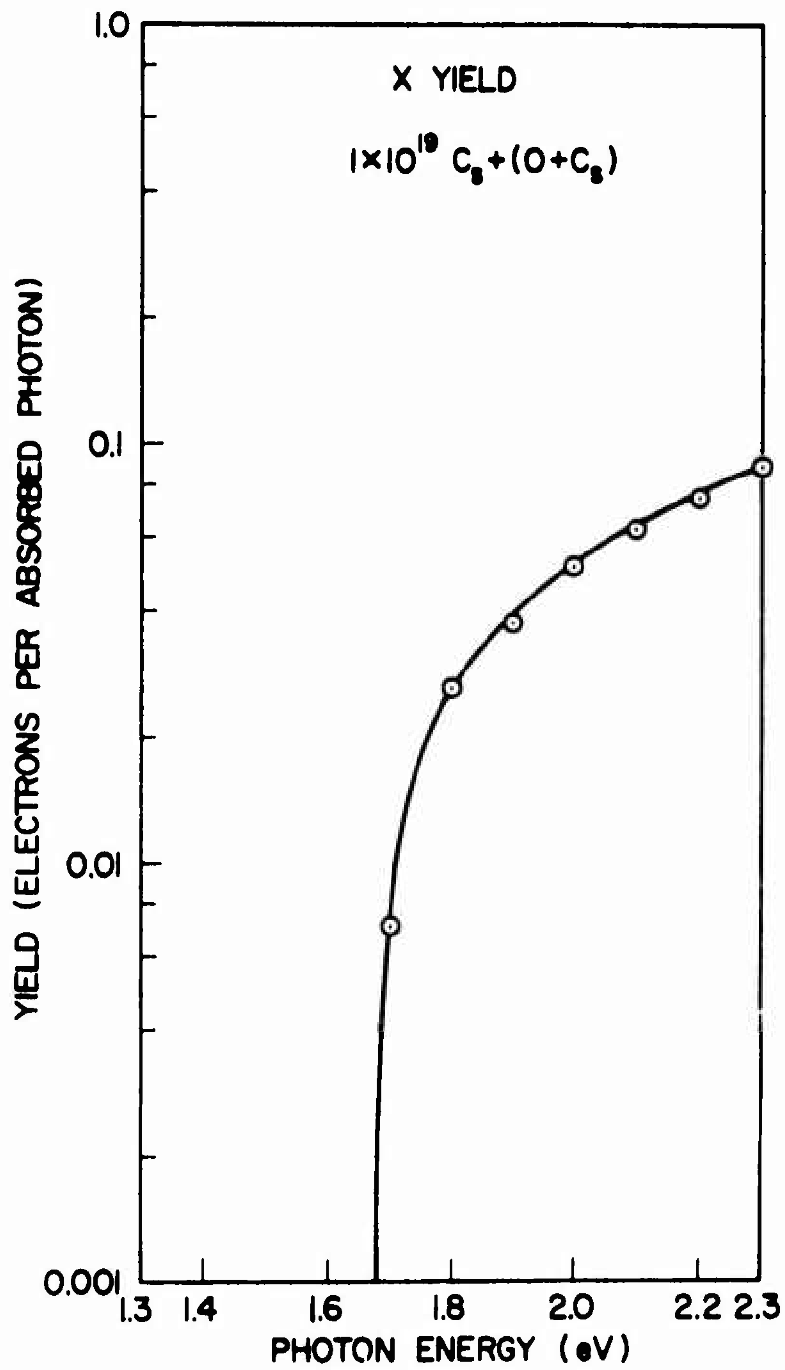

FIG. 16. Theoretical (solid line) and experimental (points) yields from the X_1 minima in a 1 x $10^{19}/cm^3$ Zn-doped GaAs crystal with a Cs + (O+Cs) surface treatment.

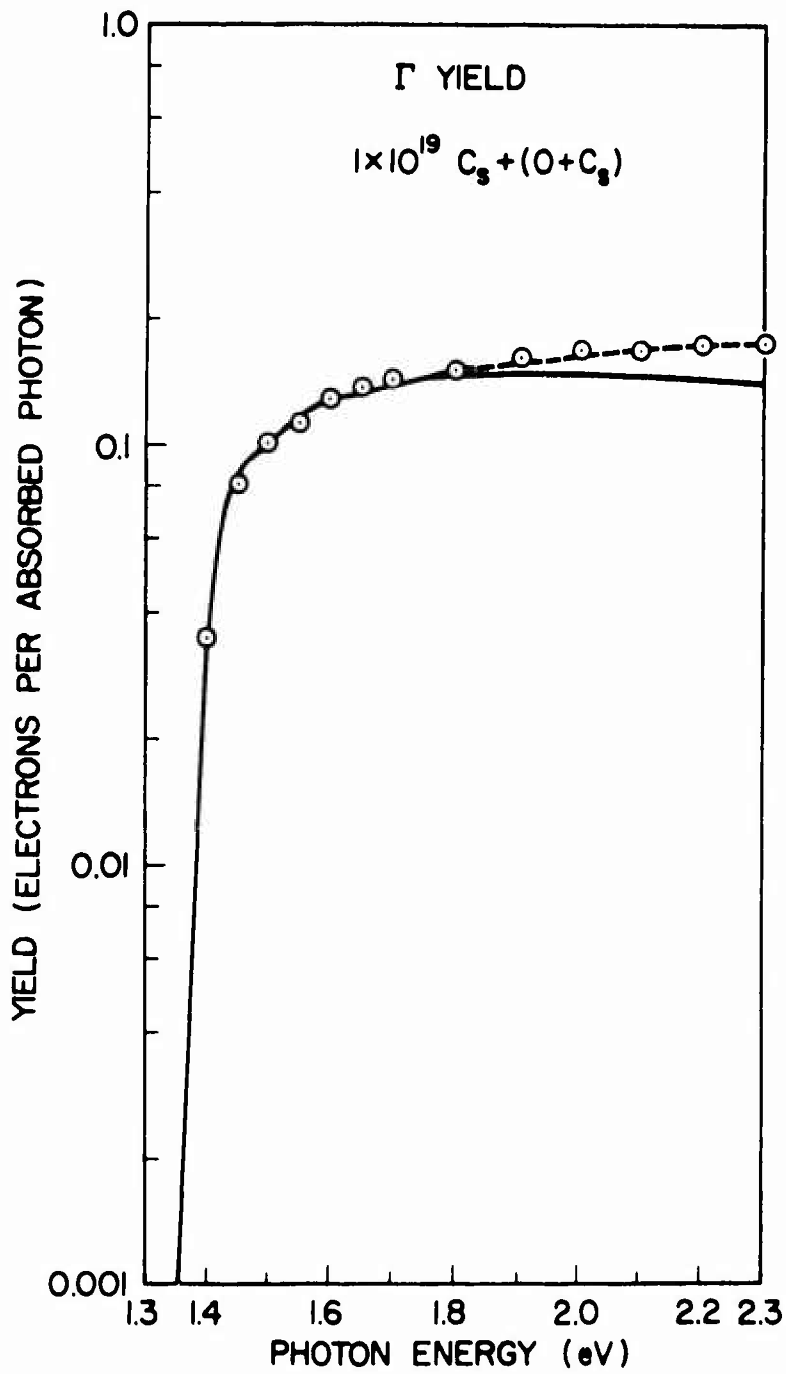

FIG. 17. Experimental yield (points) for the Γ_1 minima in a $1 \times 10^{19}/cm^3$ Zn-doped GaAs crystal with a Cs + (O+Cs) surface treatment, compared with Eq. (3.8) (solid curve) and Eq. (3.9) (dotted curve).

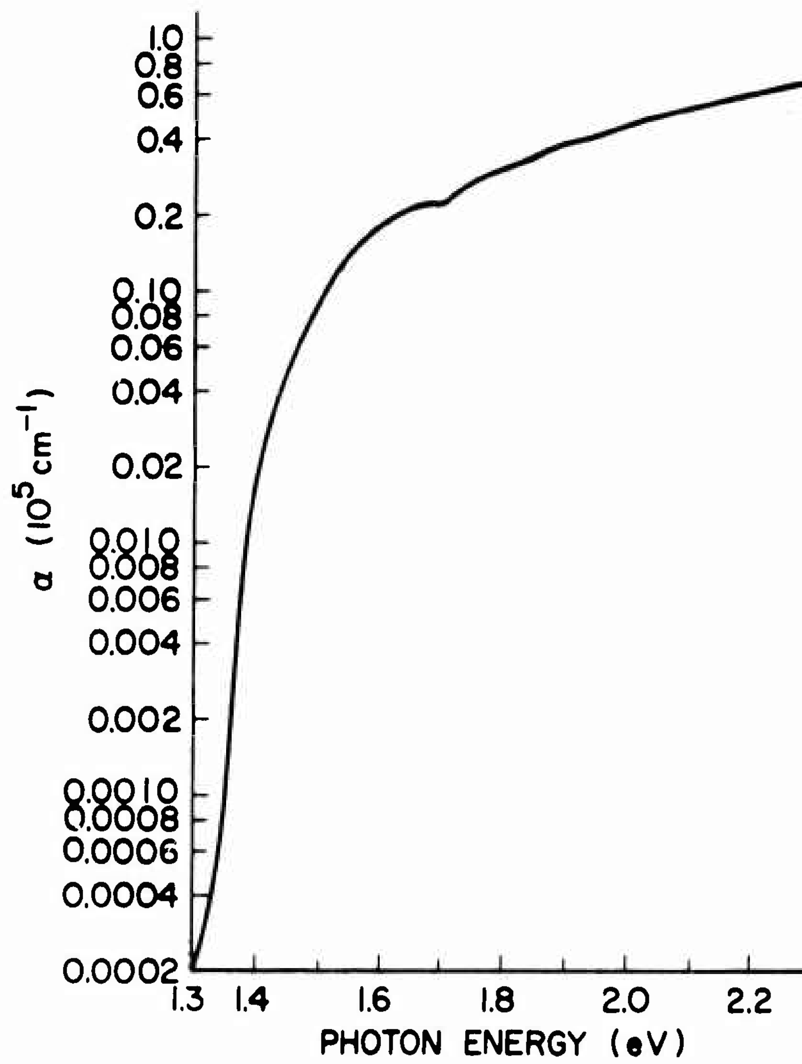

FIG. 18. p^+ GaAs optical absorption coefficient, α, for $p = 3 \times 10^{19}/cm^3$.

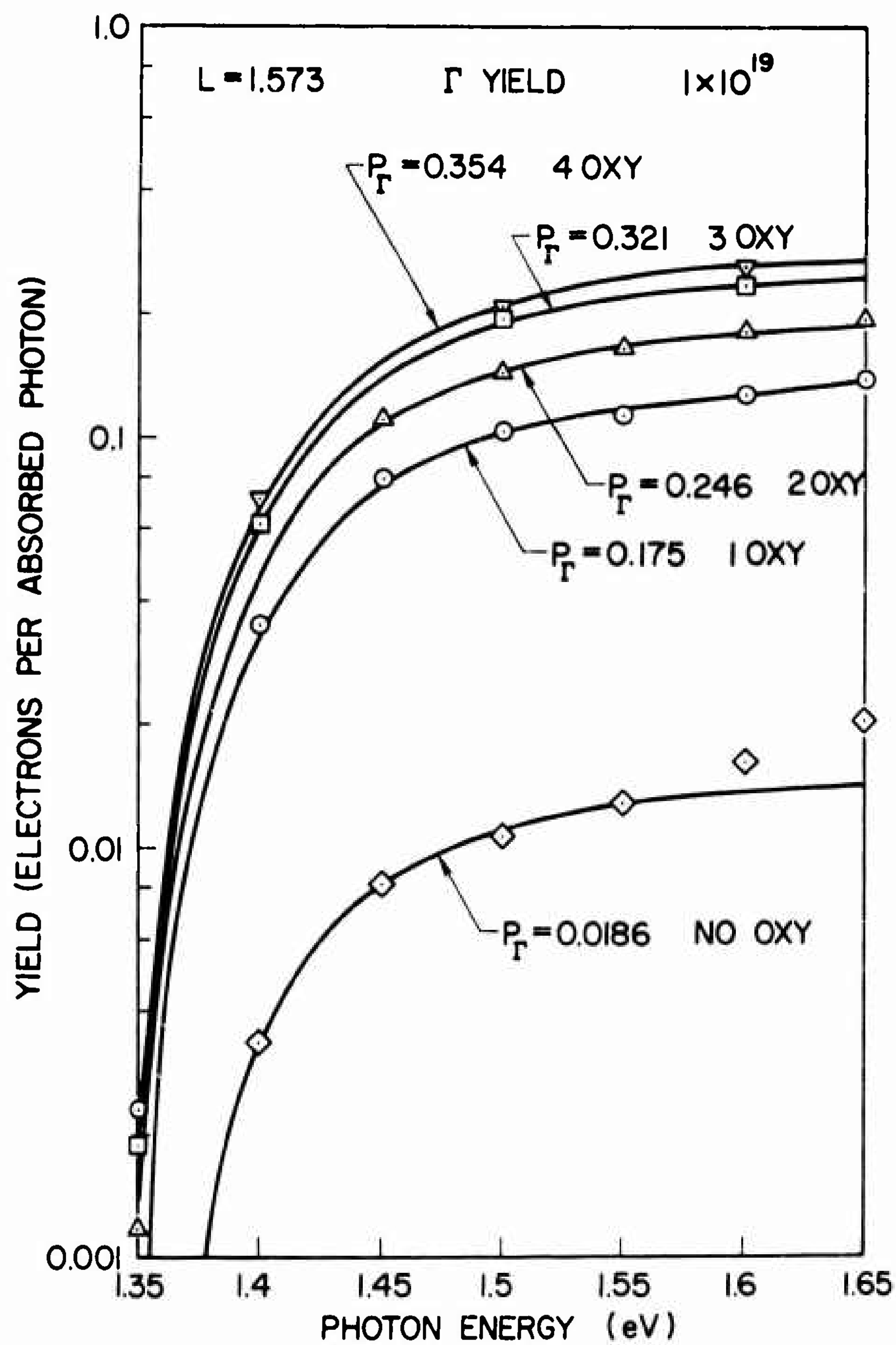

FIG. 19. Comparison between theoretical and experimental Γ_1 yields for various surface treatments, demonstrating that the measured diffusion length is a property of the bulk crystal, and is independent of surface treatment.

varies over a range of almost 20. In both Fig. 17 and the lowest curve in Fig. 19, there is a slight discrepancy between theory and experiment. A probable reason for at least part of this discrepancy is the assumption of complete thermalization of Γ electrons in a distance short compared with other relevant distances. Γ electrons which are not completely thermalized before reaching the band bending region would be expected to have a higher escape probability than those which are thermalized. As the absorption length decreases (photon energy increased), the departure from thermalization becomes more significant. Figure 20 shows the comparison between energy distributions for photon energies of 1.6 eV and 2.3 eV at 80°K. The increased number of electrons at the high energy end of the distribution gives experimental evidence for this departure. The increased escape probability caused by lack of complete thermalization may be taken into account empirically by adding an additional parameter, P_{Γ}', which is slightly larger than P_{Γ}, to the Γ yield equation, giving

$$Y_{\Gamma} = \frac{1}{(1 + 1/\alpha L_{\Gamma})} \left[F_{\Gamma} P_{\Gamma} + \frac{F_X P_{\Gamma}'}{1 + \alpha L_X} \right] \text{ for } L_X \ll L_{\Gamma} . \qquad (3.9)$$

The dotted curve in Fig. 17 is drawn using this equation with $P_{\Gamma}' = .22$. (The other parameters are the same as previously listed.) The match between theory and experiment is now quite good.

Using the least squares fit between this theory and experimental data for several samples, we have obtained the Γ diffusion lengths which are shown in Table II. Only experimental data for photon energies between 1.45 eV and 1.65 eV was used to make the least squares fit in order to

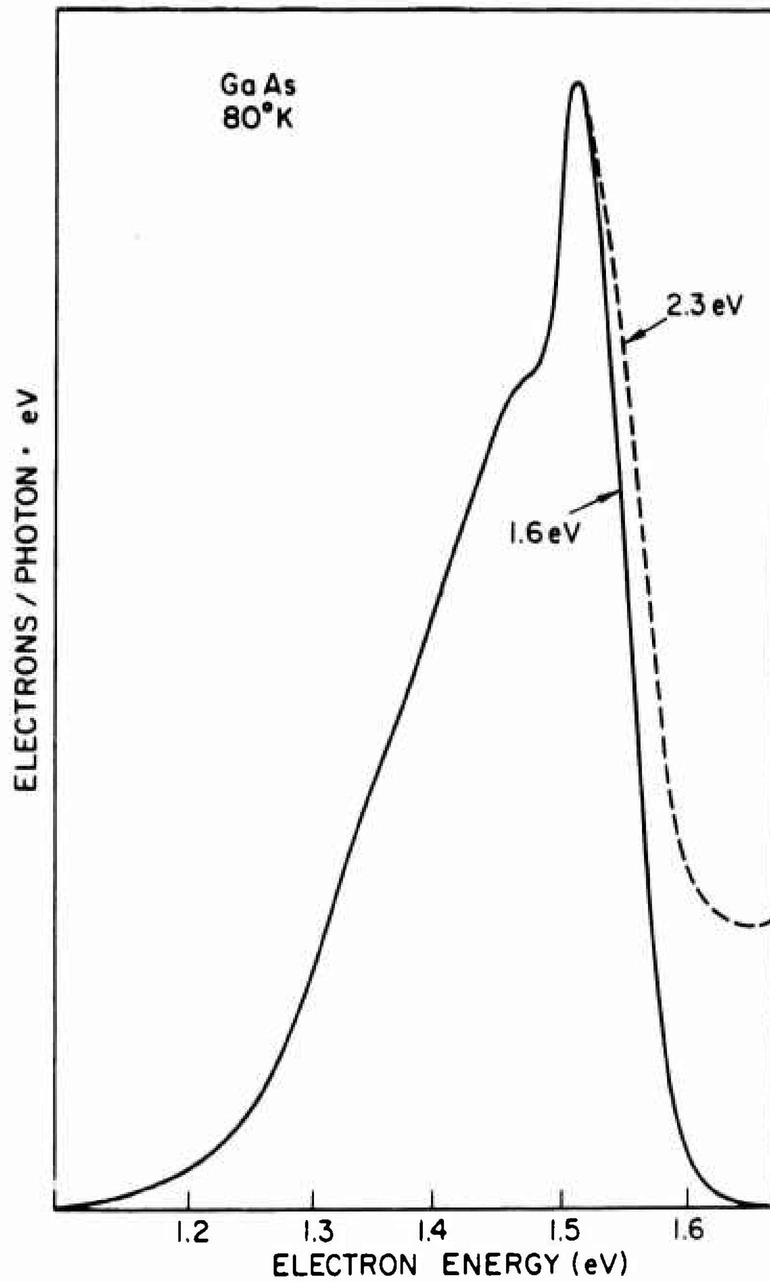

FIG. 20. Comparison of the Γ_1 peak in 80°K energy distribution curves for photon energies of 1.6 eV and 2.3 eV, showing evidence for the lack of complete thermalization with 2.3 eV excitation.

TABLE II

Measured Γ Diffusion Lengths for Boat Grown Zn-Doped Material

Carrier Concentration /cm^3	Diffusion Length Microns	
	300°K	80°K
1×10^{19}	1.6 ± .2	
3×10^{19}	1.2 ± .2	1.0 ± .3
4×10^{19}	1.0 ± .2	

prevent any effect of departure from complete thermalization or changes in α and F_Γ near the band gap with doping density on the measured diffusion length.

The X diffusion length is found to be independent of doping and is measured to be .03 microns at room temperature. As indicated earlier, the measured value of the X diffusion length depends on the function F_X. Without doing an exact calculation knowing the values of the optical transition matrix elements, it is difficult to estimate the possible errors in F_X. It is possible, however, to calculate the maximum possible error in the value of L_X. The yield in the X minima is given by equation (3.7). Solving for L_X, we obtain

$$L_X \quad \frac{Y_X}{\alpha(P_X F_X - Y_X)} \quad . \qquad (3.10)$$

At 2.3 eV for this sample, $Y_X = 0.087$, and $\alpha = 0.7032 \times 10^5$/cm. By estimating the maximum and minimum limits of $P_X F_X$, we may estimate the possible range of L_X. The upper limits of P_X and F_X give a lower limit of L_X, and conversely the lower limits of P_X and F_X give a upper limit of L_X. 2.3 eV was chosen because at 2.3 eV all transitions from the top two valence bands are included in F_X, and all transitions from the 3rd highest valence band are included in F_Γ, independent of small errors in the band structure calculation.

The maximum possible value of F_X is 1.0. Pseudopotential calculations[5] indicate that the matrix elements for transitions from the 3rd highest valence band are smaller than for transitions from the top two valence bands by about a factor of 3. If this ratio is off by a factor of 2, that is if a ratio of 1.5 is the correct ratio, then F_X (2.3 eV) is greater than 0.82,* giving a lower limit for F_X.

The maximum yield for this sample and surface treatment is about 0.5 (for photon energies low enough that carrier multiplication is not possible). The Γ yield in this range (around 3.0 eV) is at a minimum value of 0.06 electrons/absorbed photon. The "average" escape probability for X and high energy electrons is then 0.6. Assuming that escape probability is a monotonically increasing function of energy, we have 0.6 for the maximum value of P_X.

---

* If there were an equal number of transitions to the conduction band from each valence band, then $F_X = 1+1 / 1+1+(1/1.5)^2 = 0.82$. Since in fact there are fewer transitions from the third highest valence band, F_X is greater than 0.82.

For an optimum surface treatment of cesium plus six additional oxygen-cesium layers on this sample, $P_{\Gamma} = 0.360$, and the vacuum level is less than 0.3 eV below the Γ_1 minima. Again assuming a monotonically increasing escape function, $P_X > 0.360$. If we take into account absorption in the six oxygen-cesium layers, and the fact that escape probability does increase with energy, a minimum value of 0.45 for P_X is still a conservative lower limit. From these considerations

$$0.024 < L_X < 0.44 \text{ microns} \tag{3.11}$$

giving $L_X = 0.03 \begin{smallmatrix} + 0.014 \\ - 0.006 \end{smallmatrix}$ microns at room temperature.

IV. THE HOT ELECTRON SCATTERING MODEL FOR HIGHER PHOTON ENERGIES

For photon energies above 2.3 eV, the number of electrons emitted which are not thermalized becomes significant. The diffusion model is no longer sufficient to explain the experimental results, and we must consider in more detail the scattering process by which thermalization in the X minima occurs. The major scattering mechanism for hot electrons in the X minima is equivalent intervalley scattering by optical phonons for which the relaxation time is given by Conwell and Vassel[6] as

$$\frac{1}{\tau_{XX'}} = \frac{2}{3} \frac{D_{XX'}{}^2 (m_X{}^{(N)})^{3/2}}{2^{1/2}\pi\hbar^3 \rho\omega_{opt}(e^{\beta}-1)} \times \left[(E+\hbar\omega_{opt}-E_X)^{1/2} + e^{\beta}(E-\hbar\omega_{opt}-E_X)^{1/2}\right] \quad (4.1)$$

where E_X is the energy of the X minima, and $\hbar\omega_{opt}$ is the optical phonon energy. For $E-E_X >> \hbar\omega_{opt}$,

$$1/\tau_{XX'} \approx C\ (E-E_X)^{1/2} \quad (4.2)$$

where C is a temperature dependent constant. For this energy dependence

TABLE III

Numerical Values Used in Calculations

$C_\ell = \rho\mu_\ell{}^2$		$m_1 = 0.065\ m_o$	
$\hbar\omega_{opt} = 0.03$ eV		$\rho = 5.31$ g/cm^3	
$m_X{}^{(n)} = 1.2\ m_o$		$q = 1.602 \times 10^{-19}$ coulomb	
$m^* = 0.41\ m_o$		$\mu_\ell = 5.22 \times 10^5$ cm/sec	

of τ, the mean free path is constant and will be defined as the scattering length, ℓs.

At each scattering event, the electron will lose or gain an energy equal to the optical phonon energy, $\hbar\omega_{opt}$. The average number of phonons with an energy $\hbar\omega_{opt}$ at a temperature T is given from the Bose-Einstein distribution as

$$n_a = \frac{1}{e^{\beta} - 1} \tag{4.3}$$

where $\beta = \hbar\omega_{opt}/kT$.

The probability of an electron absorbing an optical phonon is proportional to n_a, while the probability of emitting a photon is proportional to $n_a + 1$. Thus, the probability of gaining energy during a scattering event is given by

$$\begin{aligned} P_G &= \frac{n_a}{2n_a + 1} \\ &= \frac{1}{1 + e^{\beta}} \quad . \end{aligned} \tag{4.4}$$

The probability of losing energy during a scattering event is then

$$P_L = 1 - P_G . \tag{4.5}$$

As discussed earlier, we may calculate the exact excited energy distribution from the band structure throughout the Brillouin zone and the optical transition matrix elements. Let this excited distribution function be given by $f_0(E)$, where $f_0(E)$ is normalized such that $\int_0^{\infty} f_0(E)dE = 1$.

The distribution after one scattering event is then given by

$$f_1(E) = P_G f_0(E - \hbar\omega_{opt}) + P_L f_0(E + \hbar\omega_{opt}). \tag{4.6}$$

Continuing this process, the distribution after n scattering events is given by

$$\begin{aligned} f_n(E) &= P_G f_{n-1}(E - \hbar\omega_{opt}) + P_L f_{n-1}(E + \hbar\omega_{opt}) \\ &= \sum_{\ell=0}^{n} \frac{n!}{\ell!(n-\ell)!} P_G^{\ell}(1 - P_G)^{n-\ell} f_0(E + [n - 2\ell]\hbar\omega_{opt}). \end{aligned} \tag{4.7}$$

The emitted energy distribution which can be externally observed is given by

$$f_{EMT}(E) = \sum_{n=0}^{\infty} P_n f_n(E) \tag{4.8}$$

where P_n is the probability that an electon will escape after n scatterings. P_n is a function of α and ℓ_s. For the case of a constant scattering length, ℓ_s, this function has been calculated by Duckett,[7] and is given in our notation by

$$\begin{aligned} P_n = \frac{1}{\pi(n+1)} \Bigg({}_0\int^{\infty} \Big[1 - \left(\frac{\tan^{-1}\alpha\ell_s z}{\alpha\ell_s z}\right)^{n+1}\Big] \frac{dz}{1+z^2} \\ - \sum_{j=1}^{n} P_{n-j}\, {}_0\int^{\infty} \Big[1 - \left(\frac{\tan^{-1}\alpha\ell_s z}{\alpha\ell_s z}\right)^{j}\Big] \frac{dz}{1+z^2} \Bigg) . \end{aligned} \tag{4.9}$$

In doing this scattering calculation for GaAs, we must take into account thermalization in the X minima. We may do this in a simple manner by assuming that above 1.75 eV, $f_{EMT}(E)$ is given as before by Eq. (4.8). Those electrons which would have scattered below 1.75 eV are assumed instead to remain at the energy of the X minima, giving

$$
\begin{aligned}
F_{EMT}(E) &= f_{EMT} && \text{for } E > 1.75 \\
&= \delta(E - 1.75)\int_{-\infty}^{1.75} f_{EMT}(E)\, dE && \text{for } E = 1.75 \qquad (4.10) \\
&= 0 && \text{for } E < 1.75
\end{aligned}
$$

In order to facilitate comparison with experiment, $F_{EMT}(E)$ is convolved with the normalized measured resolution function, R, of the experimental curves (see section 9), giving for the observed distribution

$$f_{OBS}(E) = \int_{-\infty}^{\infty} F_{EMT}(E - \mu) R(\mu)\, d\mu . \qquad (4.11)$$

In a practical calculation of f_{OBS}, we must terminate the summation of $P_n f_n$ at some finite value of n. P_n drops off slowly for large n, so we must look at f_n. Due to the initial normalization of f_0,

$$\int_{-\infty}^{\infty} f_n(E)\, dE = 1 \qquad (4.12)$$

for all n. Scattering down in energy is more likely than scattering up in energy, therefore

$$\int_{1.75}^{\infty} f_n(E)\, dE < \int_{1.75}^{\infty} f_{n-1}(E)\, dE. \qquad (4.13)$$

We use the criteria

$$\int_{1.75}^{\infty} f_n(E)\, dE < .05 \qquad (4.14)$$

to terminate our calculation. This calculation has been done on a computer for a photon energy of 3.0 eV, using as a variable parameter the scattering length, ℓ_s. Figure 21 shows the comparison between this calculated distribution and the experimentally measured distribution. The computer solution for longer scattering lengths gives a larger high

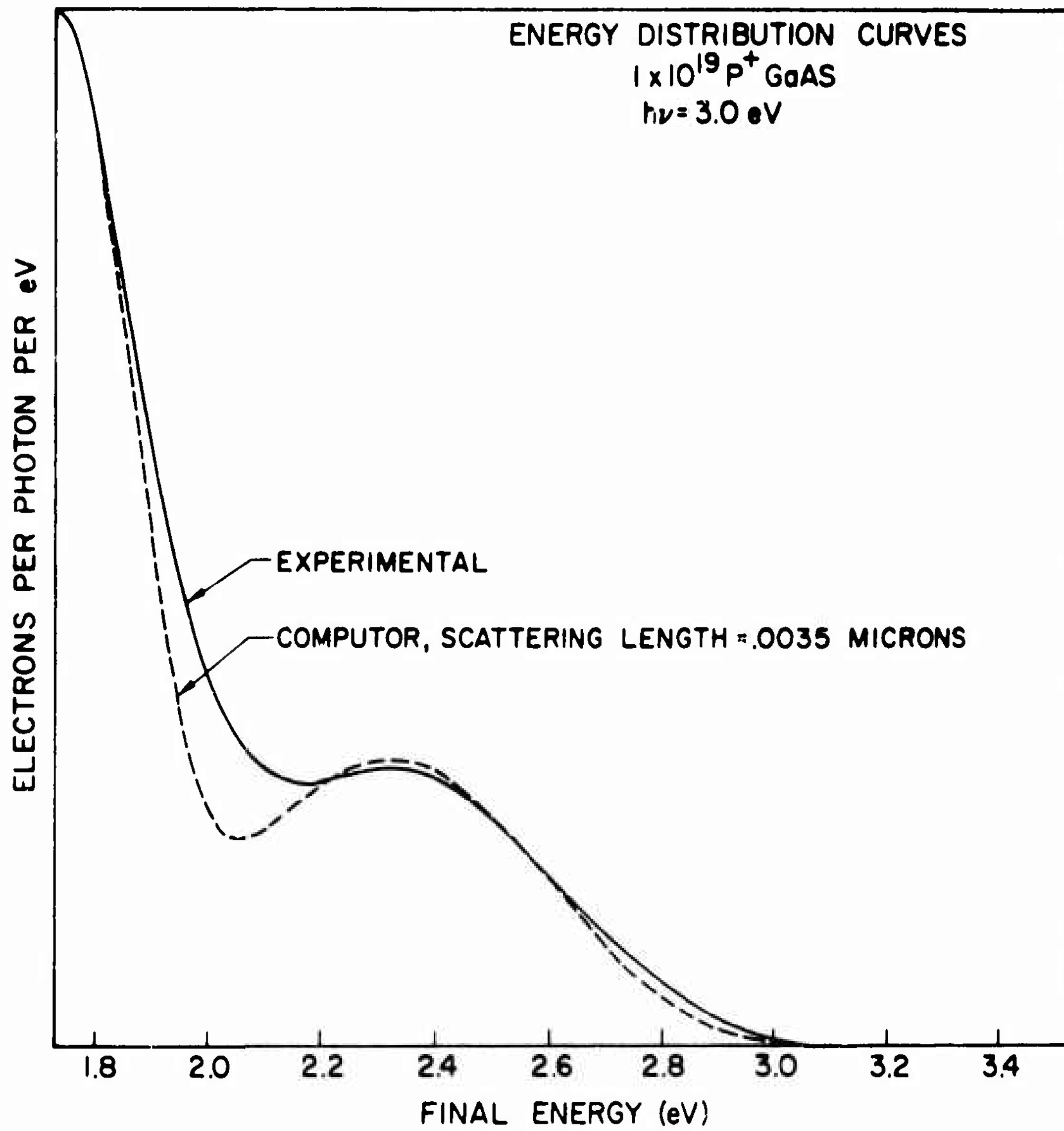

FIG. 21. Comparison of calculated and measured energy distribution curves for an excitation at hν = 3.0 eV. Electrons thermalized in the Γ_1 minima are not included in this figure.

energy peak, and that for shorter scattering lengths, a smaller peak. Thus by matching theoretical and experimental results, we are able to determine the hot electron mean free path, $\ell_s = 35 \pm 10$ Å at room temperature.

Using this scattering length, we may determine the thermalization length, L_T, discussed earlier in conjunction with the assumption of rapid thermalization and transport by diffusion. The average energy lost in a scattering event is given by

$$\Delta E_s = (P_L - P_G)\hbar\omega_{opt}. \quad (4.15)$$

Thus the average number of scattering events required for thermalization is

$$N = \frac{E - E_x}{\Delta E_s} \quad (4.16)$$

Using a three-dimensional random walk model and identifying L_T with the standard deviation of the probability density function after N scatterings, we obtain

$$L_T = \sqrt{N} \times \frac{\ell_s}{2} \quad . \quad (4.17)$$

For an electron initially excited to an energy of 2.0 eV, the thermalization length is $L_T = .0076$ microns. This value of L_T easily satisfies $L_T \ll \frac{1}{\alpha}$ over the range of interest, and gives $L_X \approx 4L_T$, satisfying the requirement that $L_T \ll L_X$ as long as only modest accuracy is desired.

V. CALCULATION OF INTERVALLEY COUPLING CONSTANTS

Using the value of ℓ_s obtained, we may calculate the coupling constant for equivalent intervalley scattering. From Eq. (4.1) we have

$$\frac{1}{\tau_{XX'}} \approx \frac{2}{3} \frac{D_{XX'}^{2}(m_X^{(n)})^{3/2}(e^{\beta}+1)}{2^{1/2}\pi\hbar^2\rho(\hbar\omega_{opt})(e^{\beta}-1)} \times (E - E_X)^{1/2} \text{ for } E-E_X \gg \hbar\omega_{opt} \quad (5.1)$$

where everything except $D_{XX'}$ and $\tau_{XX'}$ are known. For a constant scattering length, we have

$$\frac{1}{\tau_{XX'}} = \frac{v}{\ell_s} = \frac{2^{1/2}}{m^{*1/2}\ell_s} \times (E - E_X)^{1/2}. \quad (5.2)$$

Combining these equations and solving for $D_{XX'}$, we have

$$D_{XX'} = \left(\frac{e^{\beta}-1}{e^{\beta}+1} \times \frac{3\pi\hbar^2\rho(\hbar\omega_{opt})}{(m_X^{(n)})^{3/2} m^{*1/2}\ell_s}\right)^{1/2} \quad (5.3)$$

Substituting our measured value of $\ell_s = 35$ Å at room temperature gives

$$D_{XX'} = (1.5 \pm .2) \times 10^{9} \text{ eV/cm} .$$

This value is probably somewhat high, because at the electron energies involved in the determination of ℓ_s, intervalley scattering to the L_1 and X_3 valleys and polar mode intravalley scattering are also possible. If we assume that the matrix elements for scattering to states in L_1 and X_3 are equal to that for scattering to equivalent X_1 valley states, and that the combined density of states for L_1 and X_3 is 30% of the density of states in the X_1 valleys,* we have as a better estimation,

$$D_{XX'} = (1.3 \pm .2) \times 10^{9} \text{ eV/cm}. \quad (5.4)$$

---

* Estimated from a plot of equal energy contours in the ⟨110⟩ plane and symmetry considerations. It is the ratio of the density of states available for scattering into at a fixed electron energy, and not the ratio of the density of states referred separately to each minima.

Using Eq. (4.1) we may calculate the mobility for equivalent intervalley scattering in X at 300°K,

$$\mu_{EIS} = \frac{q}{m^*} \frac{3\pi\hbar^3\rho\omega_{opt}(e^{\beta}-1)\left\langle \dfrac{E-E_X}{(E-E_X+\hbar\omega_{opt})^{1/2} + e^{\beta}(E-E_X-\hbar\omega_{opt})^{1/2}} \right\rangle}{2^{1/2} D_{XX'}{}^2 (m_X{}^{(n)})^{3/2} \langle E - E_X \rangle} \tag{5.5}$$

$$= 175 \text{ cm}^2/\text{volt-sec.}$$

Combining this with Conwell and Vassel's[6] value for polar mode intervalley scattering, and with Harris' recently measured values for deformation potential scattering,[10] we obtain

$$\mu_X = 120 \text{ cm}^2/\text{volt-sec.} \tag{5.6}$$

This compares with experimental values of 155 cm^2/volt-sec[10] and 110 cm^2/volt-sec[11] for GaAs, and a value of 110 cm^2/volt-sec for GaP.[12]

Using the Einstein relationship to determine the diffusion constant gives

$$D_X = \frac{kT}{q} \mu_X$$
$$= 3.1 \text{ cm}^2/\text{sec.} \tag{5.7}$$

Using this value of diffusion coefficient and the measured value of $L_X = .03$ microns, we obtain the scattering time for scattering from X to Γ,

$$\tau_{X\Gamma} = \frac{L_X^2}{D_X}$$
$$= 2.9 \left({}^{+3.3}_{-1.1}\right) \times 10^{-12} \text{ seconds.} \tag{5.8}$$

From Conwell and Vassell[6] we have

$$\frac{1}{\tau_{X\Gamma}} = \frac{D_{\Gamma X}^2 m_1^{3/2}}{2^{1/2}\pi\hbar^3\rho\omega_{opt}} \frac{1}{e^{\beta}-1} [\gamma^{1/2}(E-E_{\Gamma}+\hbar\omega_{opt})\gamma'(E-E_{\Gamma}+\hbar\omega_{opt}) \tag{5.9}$$

$$+ e^{\beta}\gamma^{1/2}(E-E_{\Gamma}-\hbar\omega_{opt})\gamma'(E-E_{\Gamma}-\hbar\omega_{opt})].$$

For a distribution thermalized in the X minima, $(E-E_X \pm \hbar\omega_{opt}) \ll E_X-E_{\Gamma}$, giving

$$\frac{1}{\langle\tau_{X\Gamma}\rangle} \approx \frac{D_{\Gamma X}^2 m_1^{3/2}}{2^{1/2}\pi\hbar^2\rho(\hbar\omega_{opt})} \frac{e^{\beta}+1}{e^{\beta}-1} [\gamma^{1/2}(E_X - E_{\Gamma})\gamma'(E_X - E_{\Gamma})]. \tag{5.10}$$

We may solve this equation for $D_{\Gamma X}$, giving

$$D_{\Gamma X} = 3.8 \left({+.9 \atop -1.2}\right) \times 10^8 \text{ eV/cm}. \tag{5.11}$$

For this value of $D_{\Gamma X}$, the energy dependence of the Γ to X scattering time at room temperature is shown in Fig. 22, along with the scattering time for polar optical and acoustic scattering as calculated by Conwell and Vassel.[6] For an electron excited to an energy higher than .016 eV above the X_1 minima, the most likely scattering event is a scattering from the Γ_1 to the X_1 minima. Thus the assumption used in the calculation of F_{Γ} and F_X, that all electrons excited to energies higher than 1.75 eV could be considered to scatter almost instantly into an X_1 minima, is well justified.

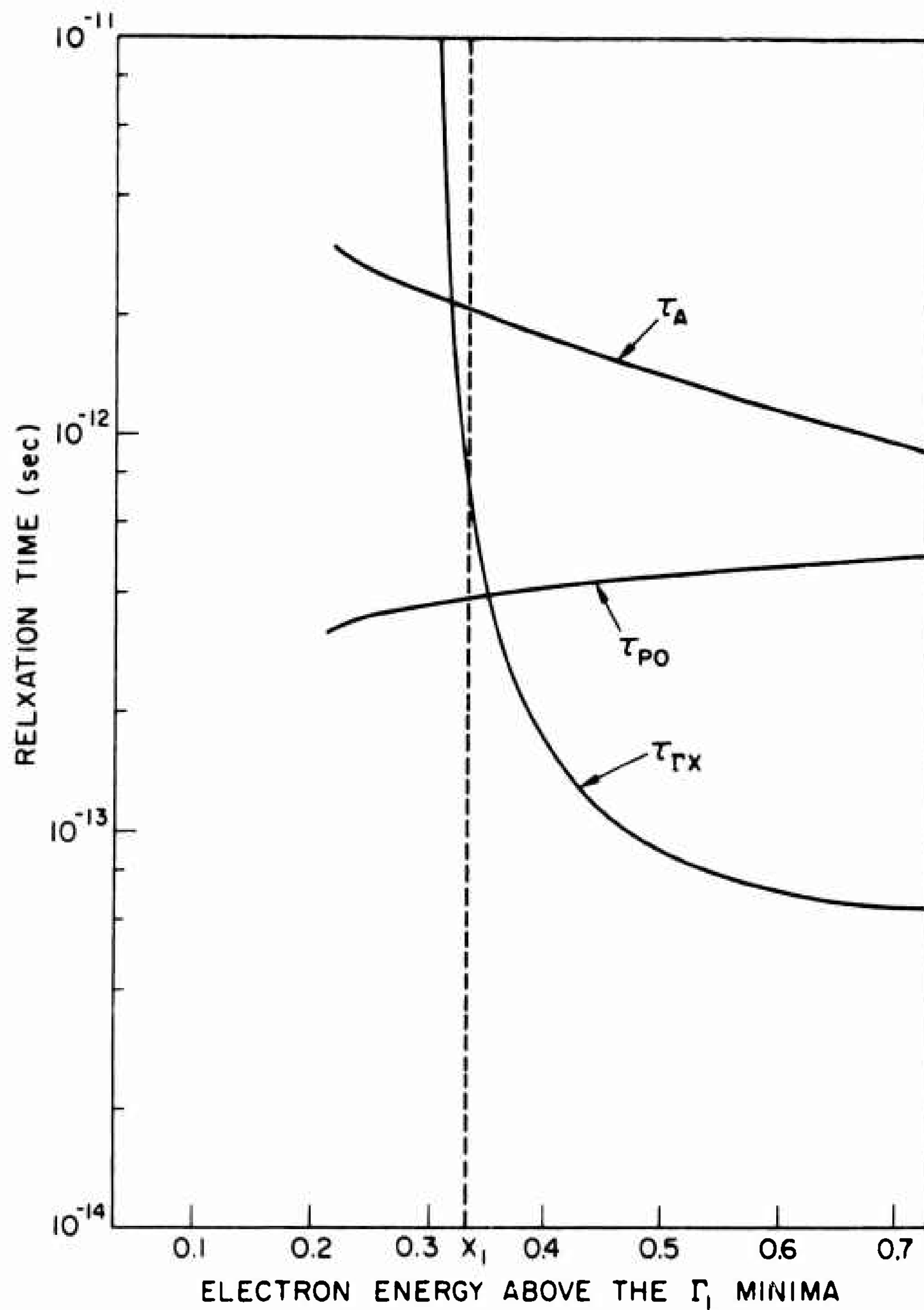

FIG. 22. Scattering times for Γ_1 to X_1 scattering, polar optical scattering, and acoustic scattering for hot electrons in the Γ_1 minima.

VI. TEMPERATURE DEPENDENCE OF THE X MOBILITY AND DIFFUSION LENGTH

At liquid nitrogen temperatures, impurity scattering and acoustic phonon scattering are more important than equivalent intervalley scattering in determining the mobility in the X minima. In order to obtain an accurate temperature dependence of the X mobility and diffusion length, we must include several types of scattering. These are plotted in Fig.23.

The mobility for equivalent intervalley scattering is given by Eq. (5.5), where the indicated averages were obtained by numerical integration.

For intravalley acoustic scattering, using Harris' recently measured values[9] of $\Xi_d = 16.8$ eV and $\Xi_\mu = -4.6$ eV, we obtain

$$\mu_A = \frac{4\pi\hbar^4 c_\ell q}{9\sqrt{2\pi}\,(m_X^* k_o T)^{3/2}} \left[\frac{1}{m_\ell \Xi_\ell^2} + \frac{2}{m_t \Xi_t^2} \right] \tag{6.1}$$

$$= 2.9 \times 10^6/T^{3/2} \quad \text{cm}^2/\text{volt-sec.}$$

From Eq. (5.10), $\tau_{X\Gamma}$ is given by

$$\tau_{X\Gamma} = 5.4 \times 10^{-12} \frac{e^\beta - 1}{e^\beta + 1} \text{ seconds,} \tag{6.2}$$

which is plotted in Fig. 24 . The mobility for scattering to Γ_1 is given by

$$\mu_{X\Gamma} = \frac{q\tau_{X\Gamma}}{m_X^*} \tag{6.3}$$

From Conwell and Vassel,[6] the mobility for polar optical scattering at room temperature is approximately 6 μ_{EIS}. The temperature dependence should be the same as for equivalent intervalley scattering, so we assume

$$\mu_{po} \approx 6\mu_{EIS}. \tag{6.4}$$

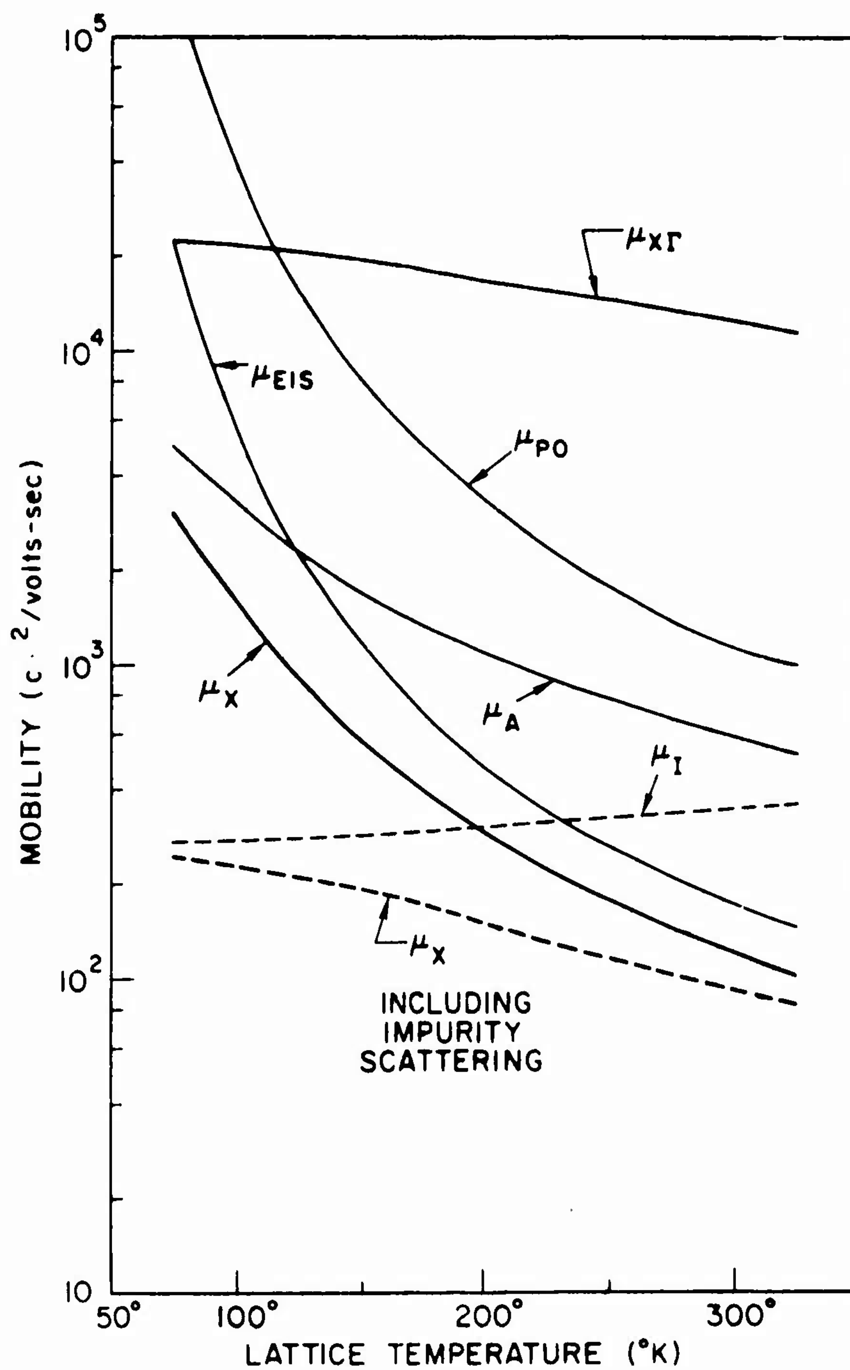

FIG. 23. Temperature dependence of the various mechanisms which determine the mobility in the X_1 minima. Solid lines are for a lightly doped sample. Dotted lines include impurity scattering.

In any case, μ_{po} is sufficiently larger than both μ_{EIS} and μ_A over the entire temperature range, that the value of mobility in the X minima is insensitive to the exact value of μ_{po}.

The mobility in the X minima for an impurity-free sample, shown as the heavy line in Fig. 23, is given by

$$\mu_X = \frac{q < \tau_X >}{m^*} \tag{6.5}$$

$$\approx \left(\frac{1}{\mu_{EIS}} + \frac{1}{\mu_A} + \frac{1}{\mu_{X\Gamma}} + \frac{1}{\mu_{po}}\right)^{-1} \tag{6.6}$$

At the high doping levels involved in this experiment, impurity scattering must also be considered. To our knowledge, no really good theory exists for minority carrier scattering time at high doping concentrations for ionized impurity scattering or electron-hole scattering. Undoubtedly the holes screen the ionized acceptors to some extent. We have approximated these types of scattering with the Mansfield impurity scattering model,[13] modified to use the hole density of states effective mass to calculate the screening potential, and an electron effective mass of .25 m_o to calculate the resultant mobility, giving the dotted curve shown in Fig. 23 as μ_I. At the $3 \times 10^{19}/cm^3$ doping level of this sample, it is necessary to include the effects of degeneracy. The Mansfield formula is therefore used to calculate the screening length, and Boltzmann statistics are used for the electrons in the conduction band.

The X mobility including impurity scattering is also shown in Fig. 23. From Eq. (6.5), $< \tau_X > \approx 2.1 \times 10^{-14}$ seconds at 300^oK and 5.8×10^{-14} seconds at 77^oK. Thus

$$\tau_{X\Gamma} >> < \tau_X > \tag{6.7}$$

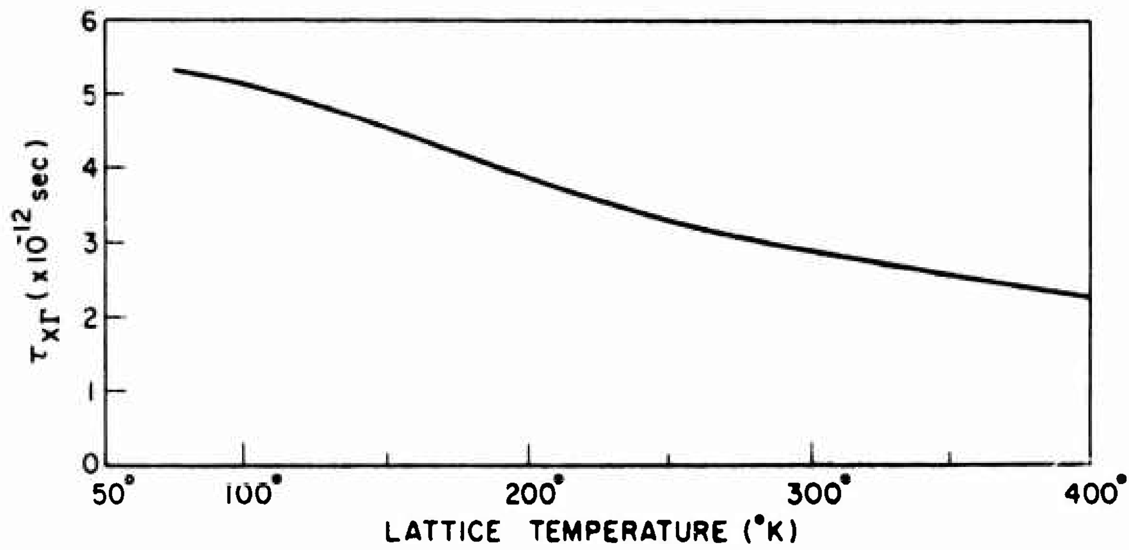

FIG. 24. Temperature dependence of the X_1 to Γ_1 scattering time.

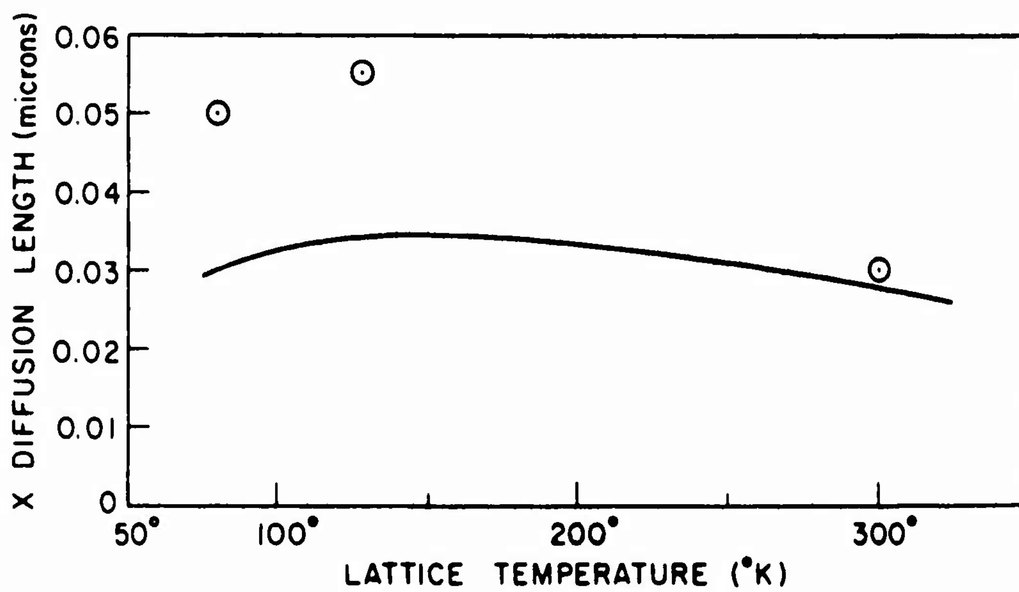

FIG. 25. Experimental (points) and theoretical (line) temperature dependence of the X diffusion length.

in both cases, and the concept of a thermalized distribution diffusing in the X minima is valid throughout the temperature range. The diffusion length is given by

$$L_X = \sqrt{\left(\frac{kT}{q}\right)\mu_X \tau_{X\Gamma}} \quad , \qquad (6.8)$$

and is plotted in Fig. 25 , along with three experimental points. The point at 130°K was the maximum experimental diffusion length. These experimental points were obtained by measuring the yield from the X minima vs temperature using Eq. (3.7), where F_X and α are obtained by shifting the 300°K values to a higher energy corresponding to the shift in the band gap. P_X increases slightly as the temperature is lowered.

The experimental and theoretical diffusion lengths are in qualitative agreement in that both increase as the temperature is decreased. The experimental increase is, however, significantly more than the theoretical increase. We believe that the physical reasons for this disagreement relate to the finite number of scatterings before the energy drops to the optical phonon energy, and a finite rate of finally settling down to a Boltzmann distribution characterized by the lattice temperature. Both of these effects result in an over-estimation of the impurity scattering cross section in the mobility theory. An arbitrary increase of the relatively temperature independent impurity mobility by a factor of approximately three gives an adjusted theory that is in line with experiment.

VII. TEMPERATURE DEPENDENCE OF THE HOT ELECTRON SCATTERING LENGTH

From Eqs. (5.1) and (5.2), we see that

$$\ell_s = K \frac{e^{\beta} - 1}{e^{\beta} + 1} \quad , \tag{7.1}$$

where K is a temperature-independent constant. Thus we have

$$\ell_s(80^\circ K) = 1.8\, \ell_s(300^\circ K) = 63\ \text{Å} \quad . \tag{7.2}$$

On the other hand, from Eqs. (4.4), (4.5), and (4.15), we see that the average energy lost per scattering event is also proportional to $(e^{\beta}-1)/(e^{\beta}+1)$, giving

$$\Delta E_s(80^\circ K) = 1.8\, \Delta E_s(300^\circ K) \quad . \tag{7.3}$$

Thus we have two counteracting effects, and might expect only a small change with temperature in the high energy part of the emitted distribution. Both the computer model (assuming no change in α with temperature, but with $\ell_s = 63$ Å) and the experimental data (shown in Fig. 26 show a small increase in the number of high energy electrons at liquid nitrogen temperature.

VIII. TEMPERATURE DEPENDENCE OF THE LOCATION OF THE CONDUCTION BAND MINIMA

Since we can see electrons thermalized in the conduction band minima in a photoemission experiment, our data offers a very direct method of measuring the energy of these minima.

In the measurement of an electron energy distribution curve (EDC), the energy scale is derived from the retarding potential applied between the emitter and the collector can. Errors in the measurement of spacing between two pieces of structure can be introduced by stray fields which are present in the experimental apparatus.

An extraneous field component parallel to the retarding field will cause a uniform shift in the energy scale of the EDC, introducing no errors in the measurement of structure spacing, except for electrons with almost zero kinetic energy. For the case of almost zero kinetic energy, there can be an apparent shift to a lower measured energy if the parallel field component changes direction along the electron trajectory. This shift will increase the measured structure spacing.

An extraneous field component perpendicular to the retarding field will give a resultant field

$$F_T = \sqrt{F_{APP}^2 + F_{\perp}^2} , \qquad (8.1)$$

where F_T is the total field seen by the electron, F_{APP} is the desired retarding field, and $F_{\perp}$ is the extraneous perpendicular field. Looking at

the change in total field with respect to a change in applied field, we see that

$$\frac{dF_T}{dF_{APP}} = \frac{F_{APP}}{\sqrt{F_{APP}^2 + F_\perp^2}} \leq 1. \tag{8.2}$$

This means that the change in field seen by the electron at every point along its trajectory is less than or equal to the change in applied field, thus the spacing in energy between two pieces of structure as measured on an experimental energy distribution curve will be greater than or equal to the actual spacing in energy.

If there is a rapidly varying threshold escape function ($C_E(E)$) near one peak (the lower peak), the apparent peak in the emitted electron distribution is at the point where

$$\frac{d}{dE}\left(f(E) \times C_E(E)\right) = f(E)\,\frac{dC_E(E)}{dE} + C_E(E)\,\frac{df(E)}{dE} = 0. \tag{8.3}$$

Since $C_E(E)$ is a monotonically increasing function of E, $\frac{dC_E(E)}{dE} > 0$, giving $\frac{df(E)}{dE} < 0$ at the measured peak. Thus the apparent peak is on the high energy side of the actual peak.

If f(E) is assumed to be a Guassian distribution of the form,

$$f(E) \propto e^{-\left(\frac{E - E_o}{\Delta E}\right)^2}, \tag{8.4}$$

then the apparent shift in the peak position is given by

$$\delta_E = \frac{(\Delta E)^2}{2C_E}\,\frac{dC_E}{dE}. \tag{8.5}$$

For our room temperature experimental data, $\Delta E \approx .1$ eV. The energy dependence of C_E is not known exactly, but from the data in Sec. IX, we estimate $C_E(1.4\ \text{eV}) \approx .1$ and $\frac{dC_E}{dE}(1.4\ \text{eV}) \approx .2$ for a $C_s + (O + C_s)^2$ surface treatment, giving $\delta_E \approx .01$ eV.

At liquid nitrogen temperature ΔE becomes much smaller, and δ_E is completely negligible.

From Eq. (8.2), it is clear that the largest errors will occur for small applied fields, that is for low energy (Γ_1) electrons. In our experimental apparatus, every attempt has been made to reduce stray fields to the smallest possible values. The measured separation between the Γ_1 and X_1 peaks at room temperature in our best experimental data is .35 eV. In this case, the effect of the threshold function is negligible (of the order of .01 eV). The actual separation is almost certainly less than .35 eV. We can estimate the error still present in this measurement by using the second derivative method for locating the final energy states of the vertical transitions, and measuring back from the energy of these states (assumed to be at $E = h\nu$ because of the large ratio of effective masses) to the location of the X_1 peak. Using Sturge's[15] value for the band gap of 1.425 eV at $300^{\circ}K$, this measurement shows that the spacing between the Γ_1 and X_1 minima can be no less than .28 eV. Our best estimate of the actual separation is .33 eV.

Because of the smaller energy differences involved, the change in the position of a conduction band minima with temperature may be determined more accurately than its relative position with respect to other minima.

Figure 27 shows a series of energy distribution curves for a photon energy of 1.6 eV taken over a range of temperatures between $80^{\circ}K$ and $300^{\circ}K$. Figure 26 shows a similar series for a photon energy of 3.0 eV. Both sets of curves are for a 3×10^{19} Zn-doped sample. In cooling from $300^{\circ}K$ to $80^{\circ}K$, the Fermi level moves down .01 eV. Subtracting this value from the measured energy shifts, we see that the band gap increases $.09 \pm .02$ eV,

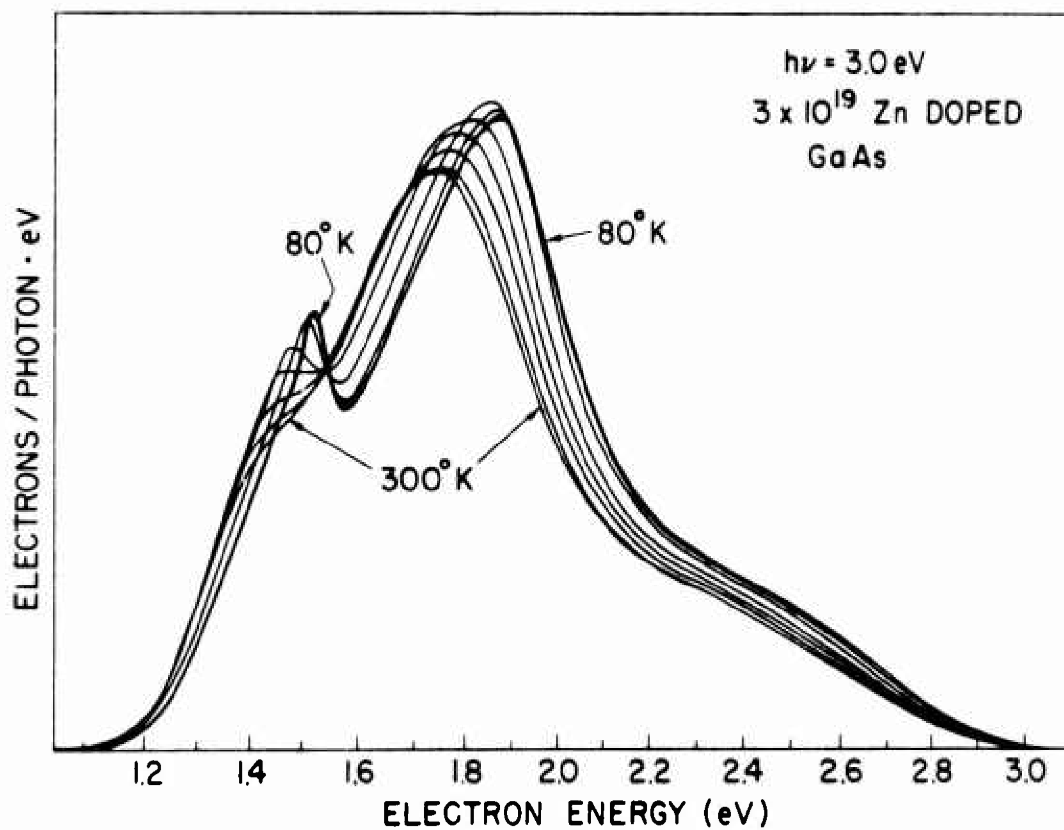

FIG. 26. Energy distribution curves for a $3 \times 10^{19}/cm^3$ Zn-doped sample for a photon energy of 3.0 eV over a temperature range of 80°K to 300°K.

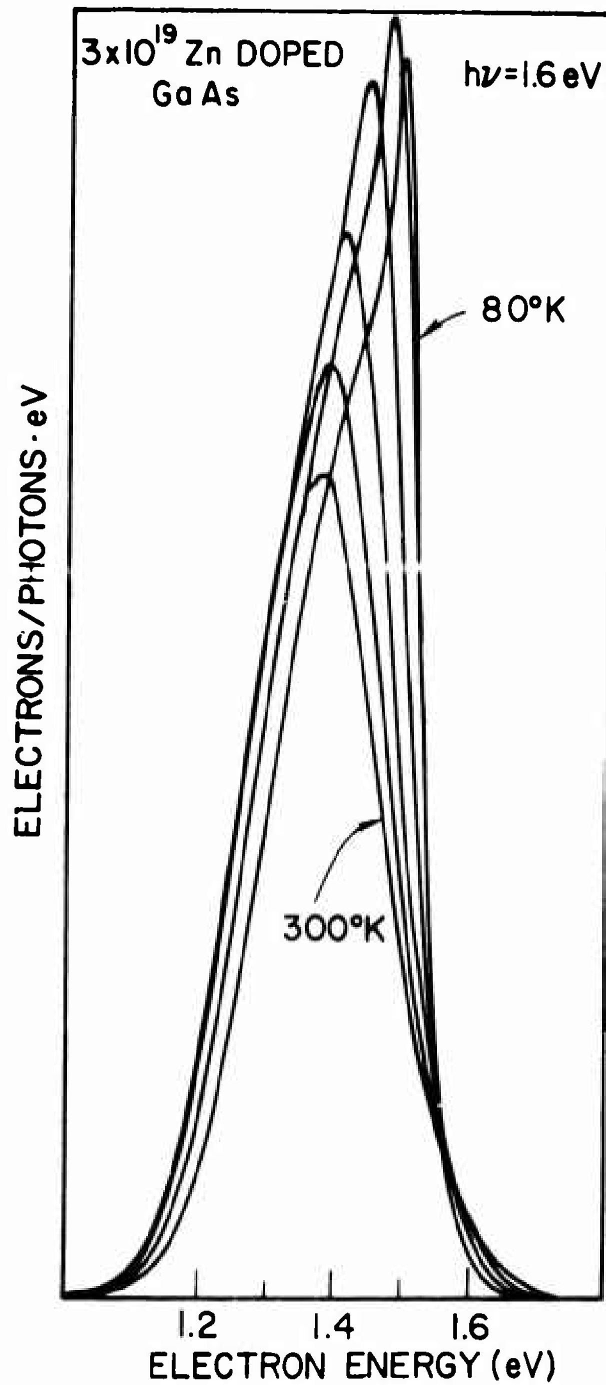

FIG. 27. Energy distribution curves for a 3 x $10^{19}/cm^3$ Zn-doped sample for a photon energy of 1.6 eV over a temperature range of 80°K to 300°K.

and the energy of the X_1 minima increases .11 ± .02 eV, when the temperature is reduced from 300°K to 80°K. The shift of .09 eV in the band gap agrees with Sturge's[15] measurement of the band gap shift, giving us confidence that δ_E from Eq. (8.5) is in fact small enough to be neglected over the entire temperature range. Our best estimate of the Γ_1 to X_1 spacing at liquid nitrogen temperature is .35 eV, which agrees well with the value of .36 eV obtained by extrapolating high temperature Hall data to 0°K.[16] However, our data is in conflict with the recently claimed value of .44 eV[17] and the commonly used value of .36 eV at room temperature.

A decrease in Γ_1 to X_1 spacing with an increase in temperature is consistent with the temperature dependence of the Gunn effect threshold field. A calculation by Harris[9] of the GaAs velocity-field characteristic has been extended to include our measured temperature dependence of the Γ_1 to X_1 spacing and the X_1 mobility, giving a theoretical velocity -field relationship over a range of temperatures from 75°K to 375°K. The results obtained for a doping density of 10^{14} shallow donors/cm^3 are shown in Fig. 28. For the details of the calculation, see Harris and James.[26] The resultant values of the Gunn threshold field and peak drift velocity vs temperature are in good agreement with Foyt's experimental results.[18]

Figure 29 shows the location of the conduction band minima vs lattice temperature, assuming a quadratic temperature dependence between experimental points which are shown with bars indicating the possible error range. The zero of the energy scale is defined from Sturge's value of the band gap[15] at 300°K.

At 80°K, two pieces of structure are visible below the Γ_1 minimum. Their exact location is determined from the derivative of the energy distribution curve, which is shown in Fig. 30 along with the corresponding E.D.C. If the sample is illuminated with a photon energy slightly less than the band gap, such as is shown in Fig. 31 for a photon energy of 1.46 eV, the structure at 1.455 eV (indicated by the square in Fig. 29) is no longer present in the energy distribution curve, and the structure at 1.415 eV (indicated by the triangle in Fig. 29) is a dominant peak.

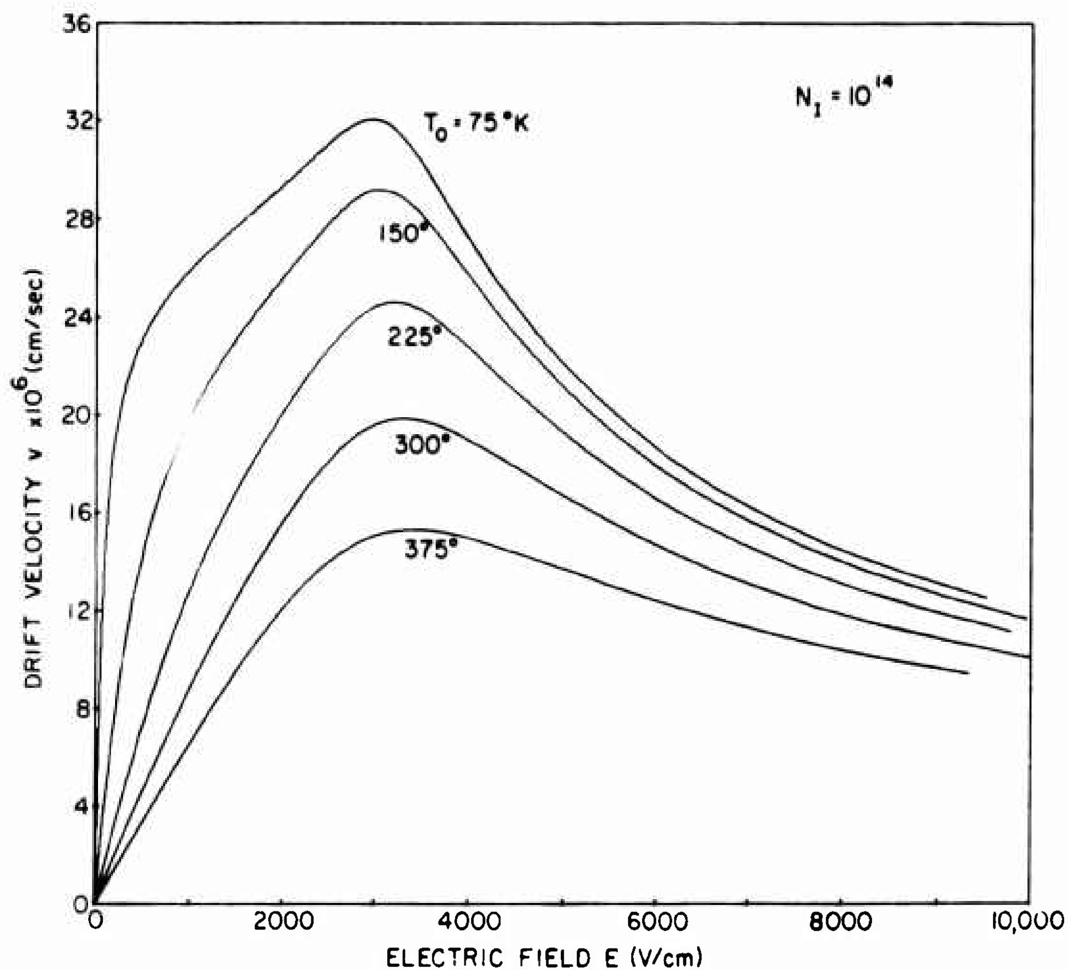

FIG. 28. Temperature dependence of the GaAs velocity-field characteristic.

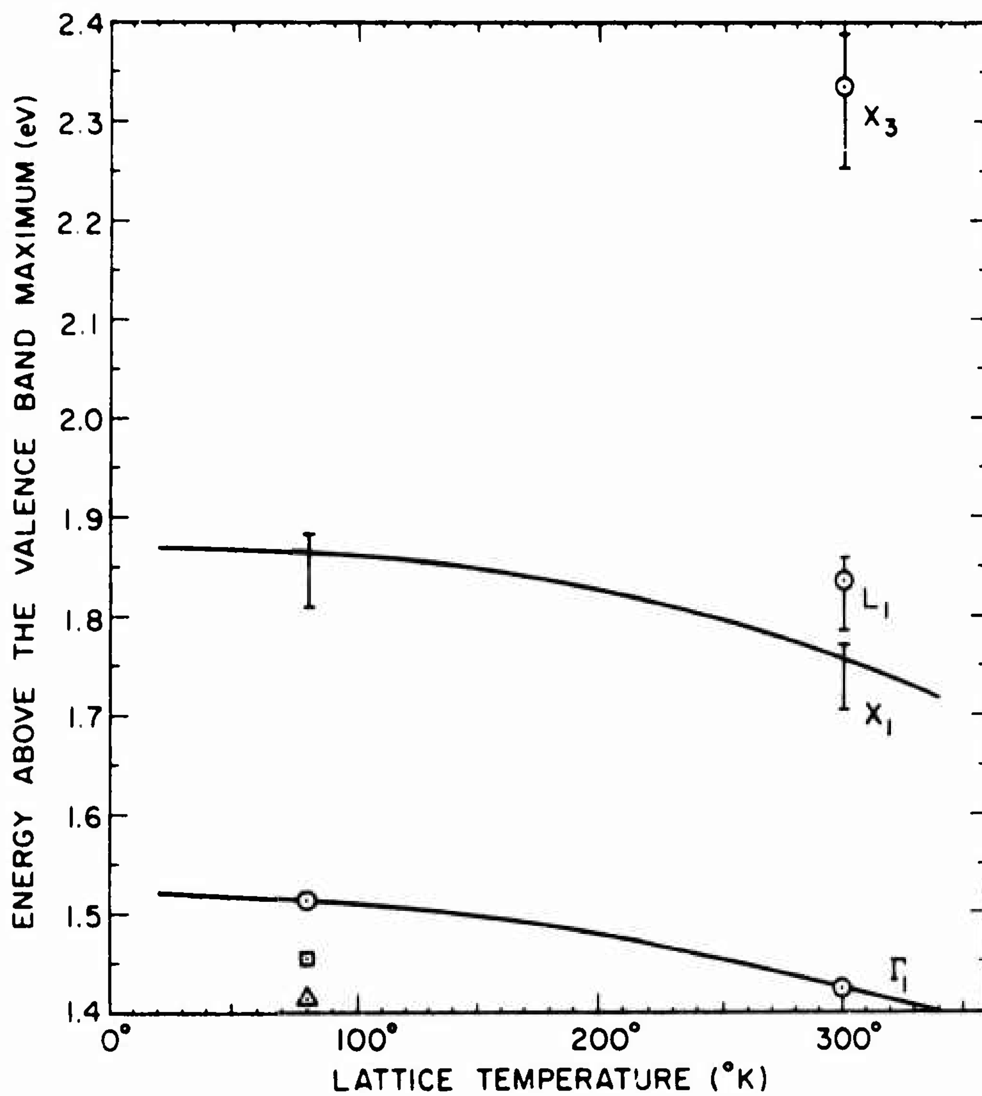

FIG. 29. Temperature dependence of the location of conduction band minima indicating best estimates and possible error ranges. The error range for the location of the L_1 and X_3 minima comes principally from the possible error in the location of the X_1 minima, X_1 to L_1 spacing is known more accurately (Ref. 14).

Thus the structure at 1.415 eV corresponds to a definite state to which photoexcitation can occur. It is possible that this peak comes from an exciton which moves into the band-bending region until the field is sufficient to pull it apart, at which point the electron is emitted. Because the bands are already bent where the exciton is separated into hole and electron, the 0.1 eV energy separation between this structure and the Γ_1 peak cannot be associated with the exciton binding energy.

The structure at 1.455 eV corresponds to a state to which direct photoexcitation is impossible, it is present only when electrons in the Γ_1 minimum are present. Its location at 0.06 eV below the Γ_1 minima prohibits identifying it with electrons which have undergone an optical phonon scattering event in the band-bending region, the optical phonon energy is 0.03 eV. There is no reason to believe that electrons which have undergone two scattering events should produce a definite structure in the energy distribution curve, when those scattering only once do not.

When an electron is accelerated through the band-bending region and strikes the potential barrier at the surface, it has some chance of being reflected rather than being emitted. We believe that the peak at 1.455 eV is electrons which have been reflected once and are then emitted. This interpretation is supported by the results shown in Section IX. An energy of 0.06 eV seems reasonable for a vibrational mode localized at the surface. Interaction with this mode would provide the necessary momentum conservation upon reflection. There is no large density of phonon modes in the bulk crystal with energies near 0.06 eV.

One of the most convenient methods for analyzing energy distribution curves for the position of structure is the structure diagram,[21] which

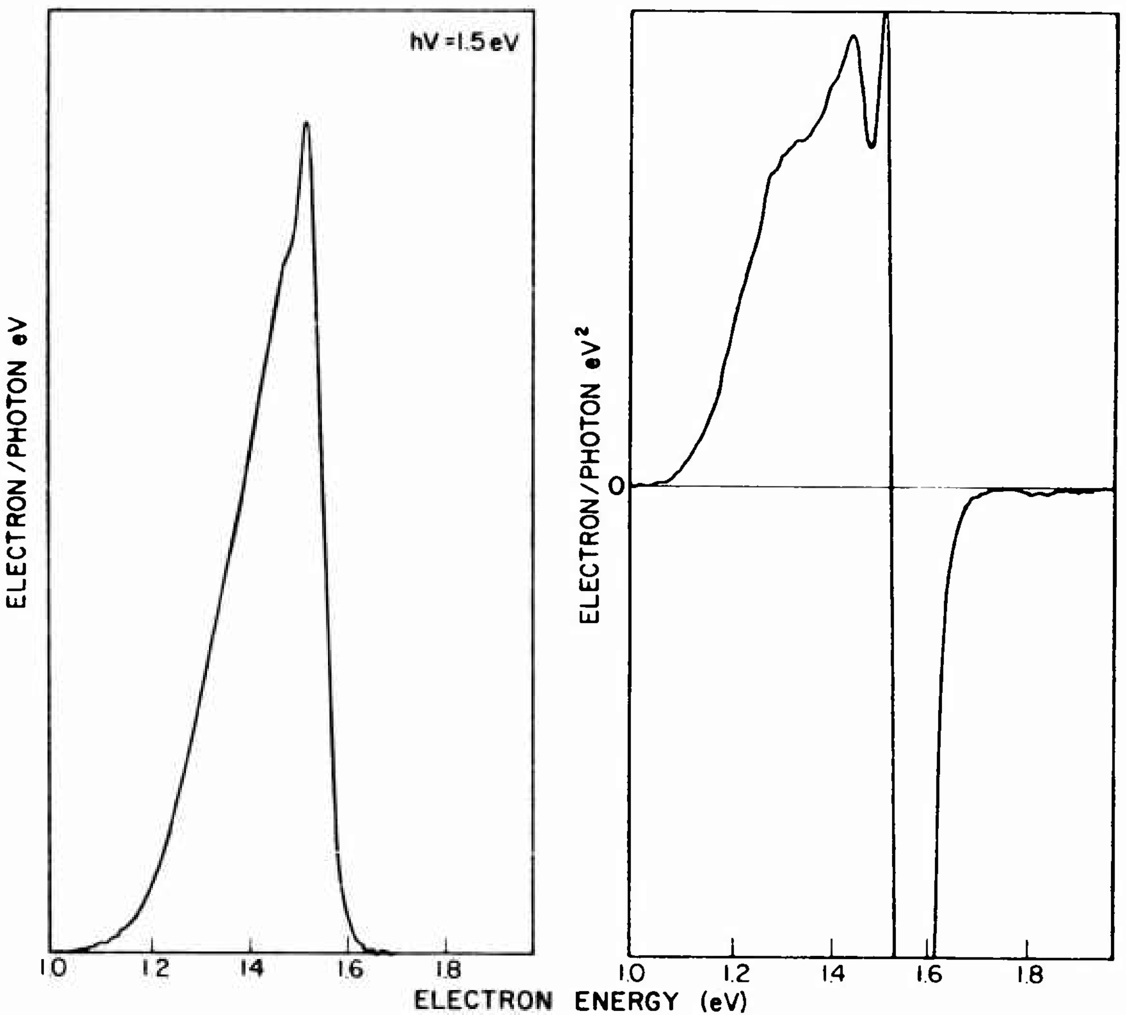

FIG. 30. The E.D.C. and its derivative for a photon energy of 1.5 eV on a $3 \times 10^{19}/cm^3$ Zn-doped GaAs crystal.

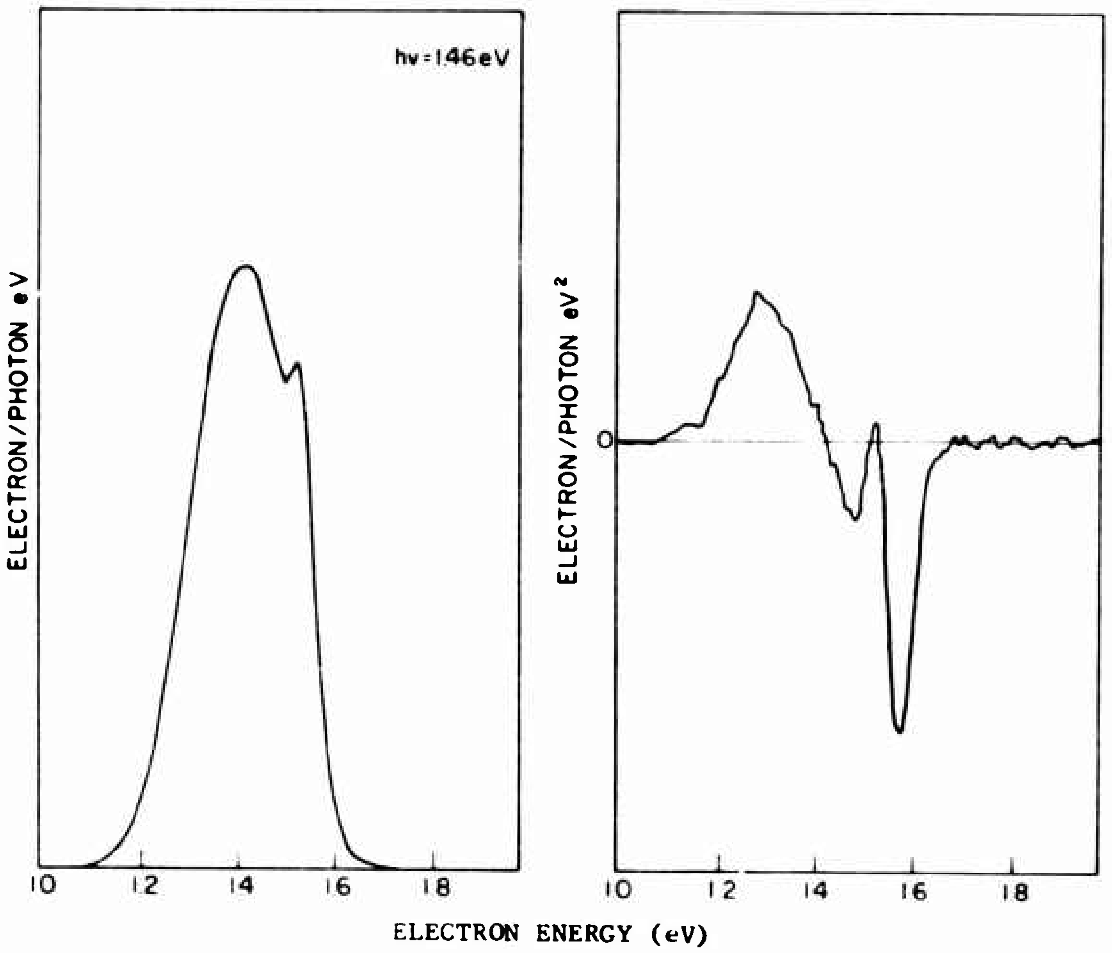

FIG. 31. The E.D.C. and its derivative for a photon energy of 1.46 eV on the same crystal as Fig. 30.

is a diagram indicating the position of structure on an electron energy vs photon energy plot. The use of the high resolution can structure along with the derivative curves allows the location of considerably more structure in the 1.0 to 5.0 eV energy range than was previously observed.[21] Our measurements for photon energies above 5.0 eV are essentially identical to those of Eden.[21]

Figure 32 shows a structure plot obtained from our highest resolution data, measured on a GaAs sample with $1 \times 10^{19}/cm^3$ Zn doping. In GaAs, $\bar{k}$ conservation is required for optical transitions. Two types of structure are present on structure diagrams for materials where $\bar{k}$ conservation is valid. When a piece of structure remains at the same electron energy for a wide range of photon energies, it results from electrons thermalized in a conduction band minima. The locations of those minima identified by comparison with band structure calculations are indicated in Fig. 32.

Figure 33 shows an energy distribution curve for p^+ GaAs with a Zn doping of $1 \times 10^{19}/cm^3$ taken at a photon energy of 2.2 eV. The peaks corresponding to the Γ_1 and X_1 minima are clearly visible. The shoulder corresponding to the L_1 minima is present, but barely discernible. Figure 34 shows the corresponding derivative of the energy distribution curve. Here the kink in the derivative curve corresponding to the L_1 shoulder is more evident, and its location can be accurately determined as 0.08 ± 0.02 eV above the X_1 minima. This structure is present at the same final energy in all curves taken over a photon energy range of 2.0 to 4.25 eV, leading to its positive identification as a conduction band minimum. Comparisons with calculated band structures show that this minimum must be the L_1 minimum.

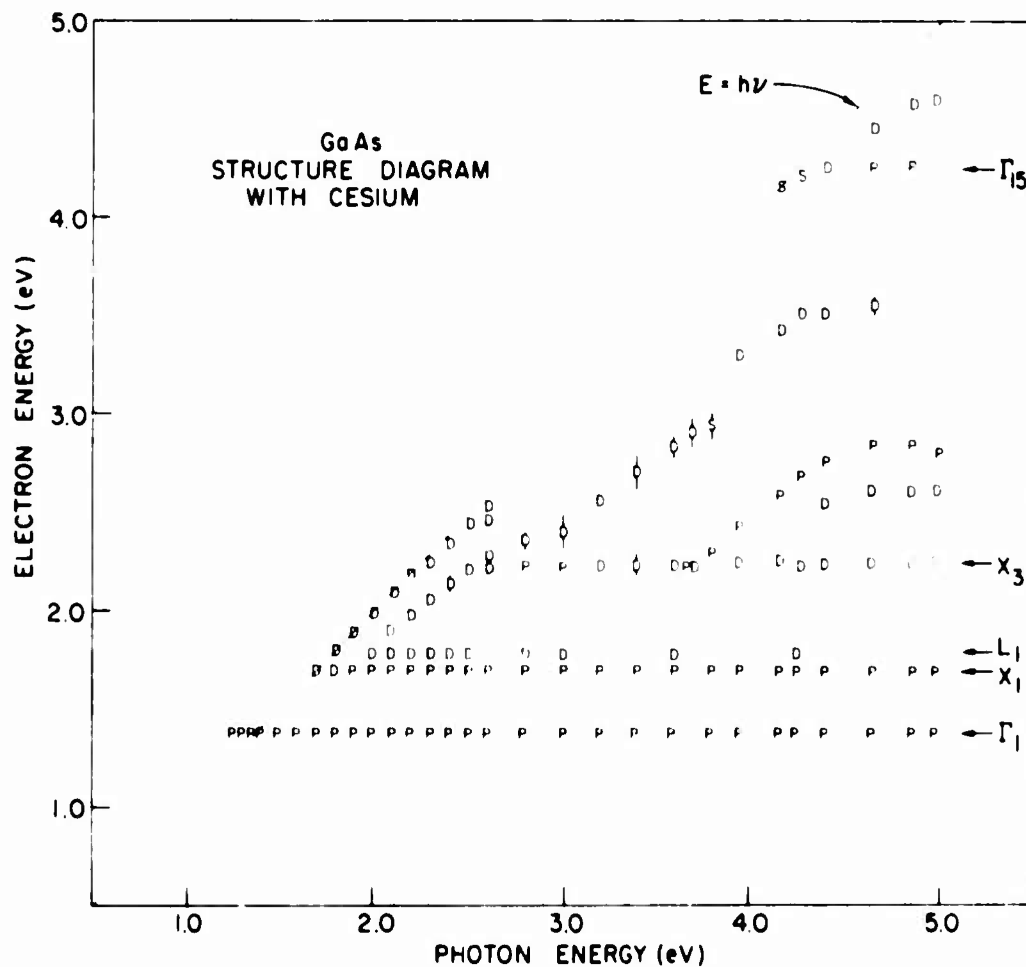

FIG. 32. Structure plot showing the location of structure measured using the high resolution can structure and the derivative curves for a 1 x $10^{19}/cm^3$ Zn-doped GaAs crystal. Structures which are definite peaks are indicated by "P." Shoulders which are identified by locating the center of a Z-shaped structure on the derivative curve are indicated by "D."

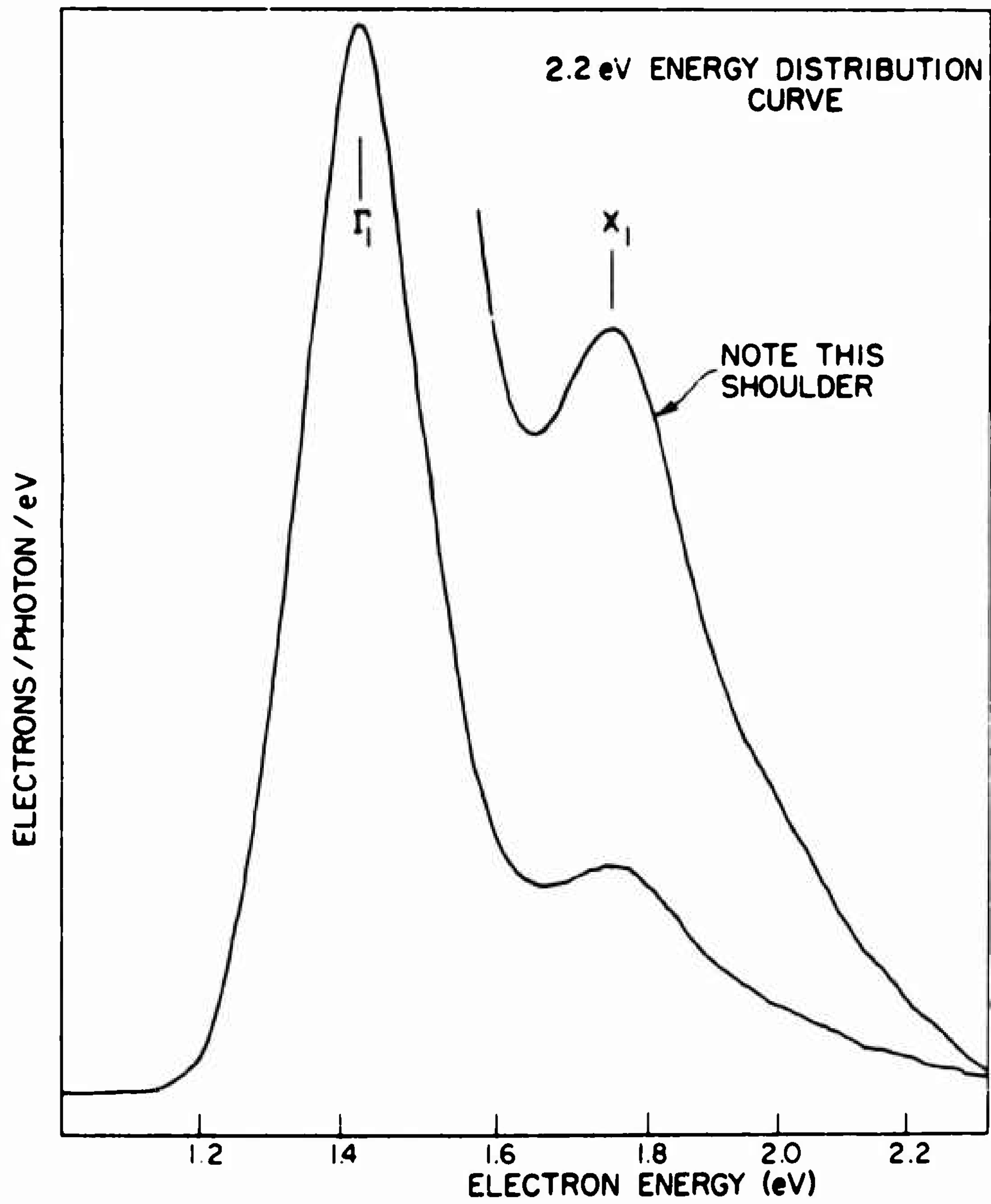

FIG. 33. p^+ GaAs photoemitted electron energy distribution curve for a photon energy of 2.2 eV.

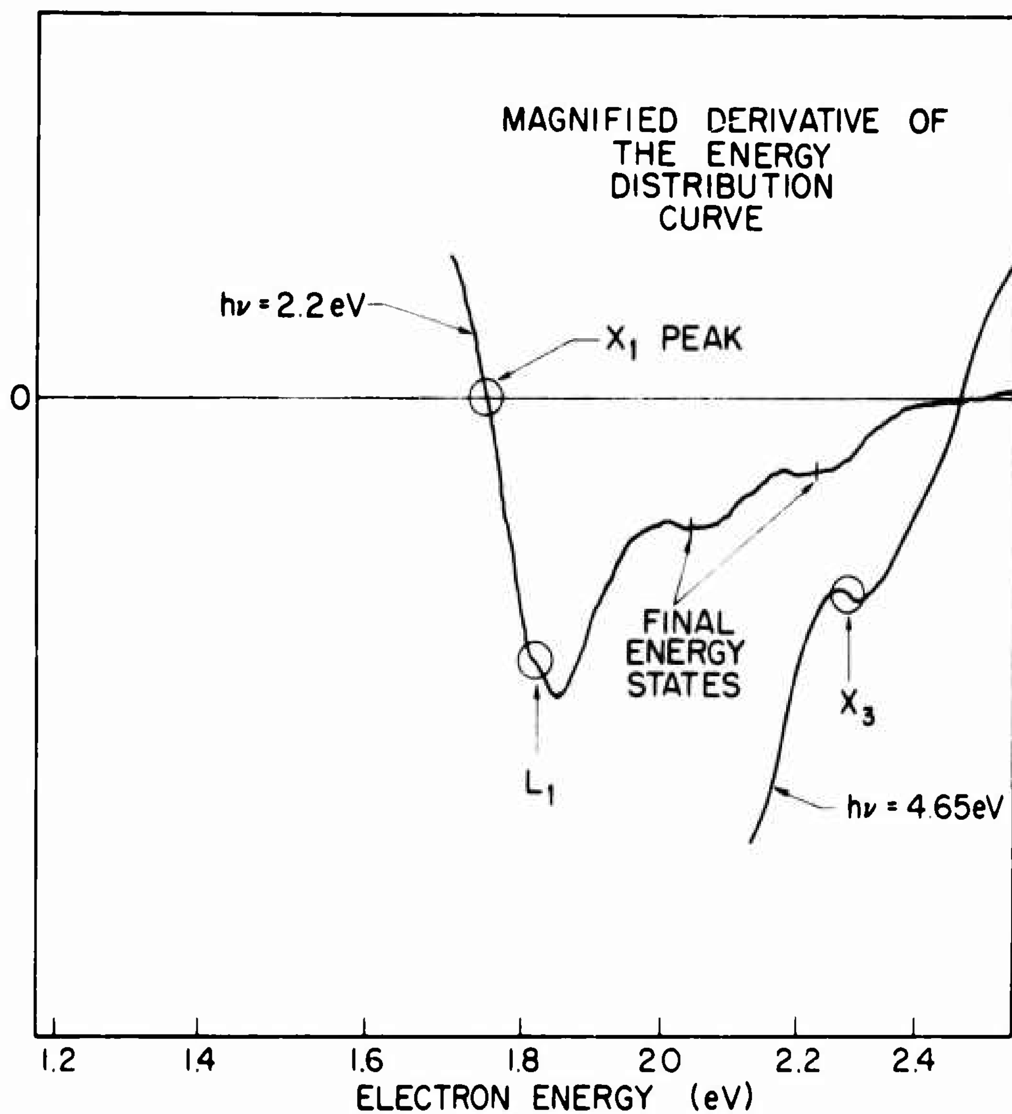

FIG. 34. Derivative of energy distribution curves. A curve is given for hν = 2.2 eV showing the position of the dominant X_1 peak as well as the L_1 shoulder and shoulders due to the unscattered electrons in the original optical excitation spectra (labeled "Final Energy States," corresponding to point "c" and higher in Fig. 2). Although the L_1 structure is weak, it was completely reproducible and occurred at the same energy for a large range of hν. Also included in this figure is data for hν = 4.65 eV showing only that portion corresponding to the X_3 conduction band minima. This structure did not move with hν.

By a similar analysis the X_3 conduction band minima have been located at 0.58 ± 0.04 eV above the X_1 minima. One of the derivative curves indicating the X_3 minima is also shown in Fig. 34. All minima except the X_1 and L_1 minima are separated enough in energy, that their identification is straightforward. It is by now a well accepted fact that the X_1 minima are lower than the L_1 minima in GaAs. Our location of the X_3 minima supports this when comparison is made with band structure calculations. Herman and co-workers' adjusted first principles band structure calculation[3] with L_1 placed 0.1 eV above X_1 places X_3 at 0.6 eV above X_1, in excellent agreement with our experiments. The same calculation done with L_1 placed 0.1 eV below X_1 places X_3 more than 1 eV above X_1, which is considerably outside the possible range of experimental error. Table IV shows the comparison between Herman's calculation corrected for spin-orbit splitting and our experimental results. Herman's calculation was done using our experimental value of 0.08 eV X_1 to L_1 spacing, but used a value of 0.36 eV for Γ_1 to X_1 spacing. Had a slightly smaller value of Γ_1 to X_1 spacing been used, the agreement might have been even closer. Figure 35 shows the band structure of GaAs as calculated by Herman.

The location of the Γ_{15} minima deserves some comment. In Eden's thesis[21] it is pointed out that the conduction band minima in this region may not be at the Γ_{15} symmetry point, therefore labelling this structure as Γ_{15} is open to some question, the actual Γ_{15} energy could be somewhat higher.

The L_3 minima is located on a structure plot including higher photon energies than are shown in Fig. 32.

TABLE IV

Experimental and Theoretical Values for the Location of Conduction Band Minima at Room Temperature

CONDUCTION BAND ENERGY LEVEL	EXPERIMENT (see text for discussion of possible errors and error ranges)	HERMAN'S BAND STRUCTURE WITH SPIN-ORBIT SPLITTING
L_3	5.05 eV	5.2 eV
Γ_{15}	4.3*	4.4
X_3	2.33	2.39
L_1	1.835	1.89
X_1	1.755	1.79
Γ_1	1.425	1.43

NOTE: All energies are given in eV with respect to the valence band maximum.

* at or near Γ_{15}

When the electron energy at which a piece of structure occurs changes as the photon energy is changed, the photon energy is changed, the electron energy of the structure corresponds with the final energy state of an optical transition. This structure comes from electrons excited near the surface which are emitted before suffering any significant energy loss. The initial energy state for the optical transition may be obtained by subtracting the photon energy from the electron energy.

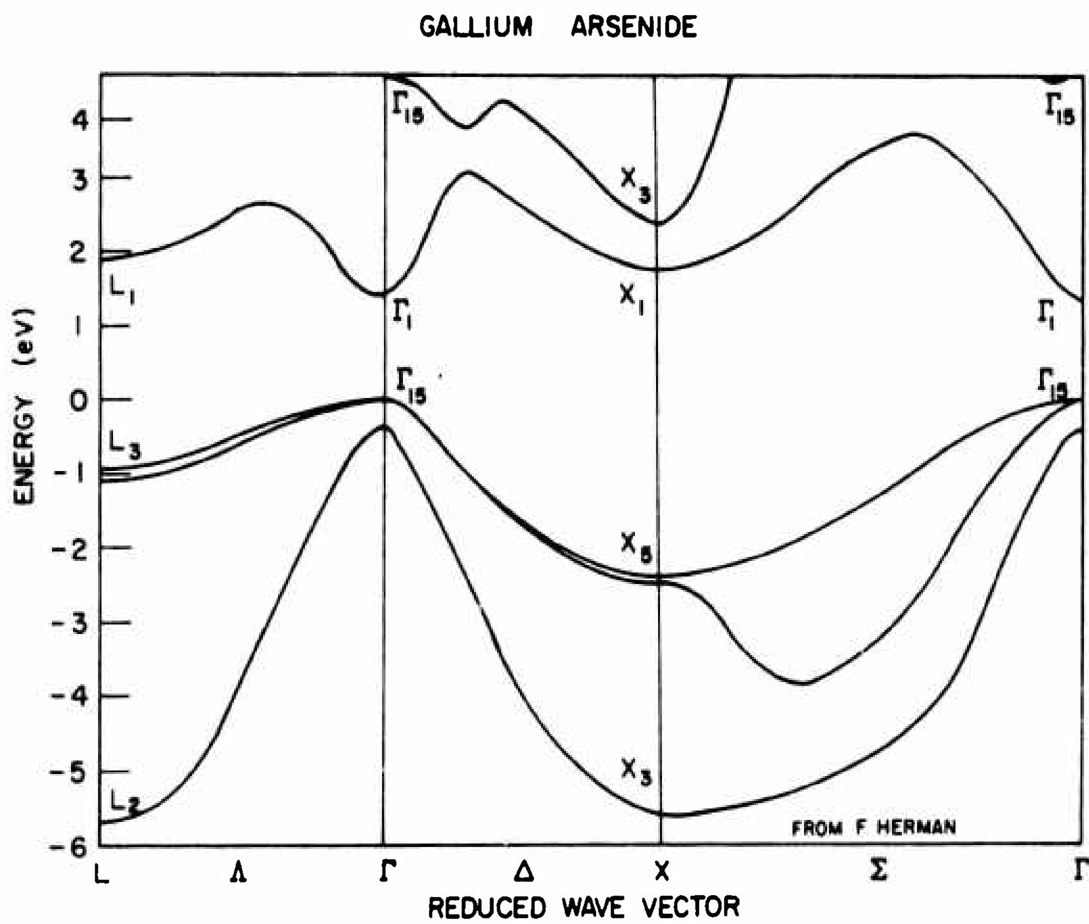

FIG. 35. GaAs band structure calculated by Herman et al.,[3] using our experimental data as a perturbation on a first principles calculation.

IX. DETAILS OF THE ESCAPE PROCESS

The sharp peak visible in the liquid nitrogen energy distribution curves indicates that the experimental apparatus is capable of extremely high resolution, and that the measured widths of the Γ_1 and X_1 peaks are in fact their actual widths. In this section we will look in detail at the physical processes which are responsible for the width of these peaks, and show how they relate to the details of the escape process which determine escape probability.

For electrons thermalized in a parabolic conduction band minima, the distribution in initial state energies is proportional to $E^{1/2}\ e^{-E/kT}$. The width at half amplitude of this distribution in the bulk of the crystal before entering the band bending region is given by

$$\begin{aligned} \Delta E_T &\approx 1.5\ kT \\ &= .04\ \text{eV} \end{aligned} \tag{9.1}$$

at room temperature.

The field in the band bending region is approximately

$$\begin{aligned} F &= \frac{\Delta E\ \text{(Band Bending)}}{W} \\ &= 720{,}000\ \text{volts/cm}, \end{aligned} \tag{9.2}$$

considerably beyond the point where saturated drift velocity is reached, thus most electrons will be heated in the Γ_1 minima and will be transferred into the X_1 minima at the first scattering event. For $D_{\Gamma X} = 3.8 \times 10^8$, the time to scatter into X_1 is approximately equal to $< \tau_X >$ at room temperature. (The exact time is energy dependent and shown in Fig. 22.) The probability that an electron will undergo n scattering events while passing through the band-bending region is given approximately by the Poisson distribution

$$P_n = \frac{e^{-\frac{W}{\ell_s}} \left(\frac{W}{\ell_s}\right)^n}{n!} \tag{9.3}$$

From Eqs. (4.7) and (4.8), the emitted energy distribution for an intially thermalized distribution in a conduction band minima at E_o is given by

$$f_{EMT}(E) = \sum_{n=0}^{\infty} e^{-\frac{W}{\ell_s}} \left(\frac{W}{\ell_s}\right)^m \sum_{\ell=0}^{n} \frac{P_G^{\ell}(1-P_G)^{n-\ell}}{\ell!(n-\ell)!} (E-E_o+[n-2\ell]\hbar\omega_{opt})^{1/2} \times$$
$$e^{-\frac{(E-E_o+[n-2\ell]\hbar\omega_{opt})}{kT}} \quad u(E-E_o+[n-2\ell]\hbar\omega_{opt}) \tag{9.4}$$

where $u(x) = 1$ for $x \geq 0$
$= 0$ for $x < 0$.

For the parameters valid for GaAs with a doping of $3 \times 10^{19}/cm^3$ at room temperature, this calculation yields an approximately Guassian distribution with a width at half amplitude of .09 eV and a peak at approximately .01 eV below the energy of the Γ minimum.

For an electron .2 eV above the bottom of the X_1 minima (valid for an electron near the surface in the band bending region which was originally thermalized in the Γ_1 minimum), the time between scattering events is given by Eq. (5.2). $\tau_{XX'} = 1.32 \times 10^{-14}$ seconds at room temperature. The accuracy with which the electron energy may be defined is limited by the uncertainty principle. The width at the half amplitude points of a measured energy distribution (assuming a Lorenzian line shape from a single energy level) is given for $\tau_{XX'} = 1.32 \times 10^{-14}$ seconds by

$$\Delta E_\tau = \frac{\hbar}{\tau_{XX'}} = .08 \text{ eV} . \tag{9.5}$$

Combining this lifetime broadening effect with the width of the emitted distribution calculated above, we obtain an expected half-amplitude width of .12 eV for the observed energy distribution of electrons thermalized in the Γ_1 minima at room temperature. The actual experimental curves show a half-width of .20 eV. The reason for the additional width is made clear by examining the liquid nitrogen data.

At liquid nitrogen temperature, we have a different situation. The half amplitude width of the initial thermalized distribution is .01 eV. From Eq. (9.3), $P_0 > P_n$ where $n > 0$; that is, more electrons will cross the band bending region without scattering than will undergo any given number of scattering events while crossing. This coupled with the fact that the probability for gaining energy during a scattering event is practically zero, leads to a skewed distribution with a peak at the Γ_1 energy point, and a tail going to lower energies. After combining this distribution with the lifetime broadening (.043 eV half-amplitude width), we obtain the results shown as the short-dashed theoretical curve in Fig. 36. Comparison with the experimental curve shows good agreement in shape at the high-energy end of the curve, and a large discrepancy in the low-energy tail. The theoretical curve, if drawn to scale, would be eight times as high as the experimental curve at the peak. The theory on the width of the energy distribution curve to this point has assumed that all electrons which reach the surface are emitted. From the measured escape probabilities, we know that this is not the case. From the actual value of the peak height of the experimental and theoretical curves, we can estimate for this sample that roughly 12 percent of the electrons which strike the surface (with an energy of 1.5 eV above the valence band maximum

in the bulk) are emitted the first time they strike the surface. We define this percentage which escapes upon hitting the surface once as the escape coefficient, C_E.

A certain fraction of the electrons which strike the surface will encounter impurities, defects, or other surface irregularities where they will lose sufficient energy to drop below the vacuum level where they will ultimately recombine. This fraction will be given by the surface trapping coefficient, C_{ST}. C_{ST} is determined by the quality of the material and the method of surface preparation, cleaved surfaces giving the lowest value observed so far. Some boat-grown material has been found to have a moderately high value of C_{ST} even for cleaved surfaces.

Those electrons which are not emitted or trapped will be reflected back into the band bending region, giving a reflection coefficient, $C_R = 1 - C_E - C_{ST}$. The structure in the liquid nitrogen energy distribution curves .06 eV below the Γ_1 minima is identified with once-reflected electrons, thus the electrons are assumed to lose .06 eV at each reflection. After being reflected, the electrons are re-accelerated toward the surface (some of them undergoing optical phonon scattering in the process) and strike the surface again.

For hot electrons where C_E and C_{ST} change slowly with electron energy and where an electron may undergo many reflections before losing enough energy that it drops below the vacuum level, the escape probability is given by

$$P = \frac{C_E}{C_{ST} + C_E} \quad . \tag{9.6}$$

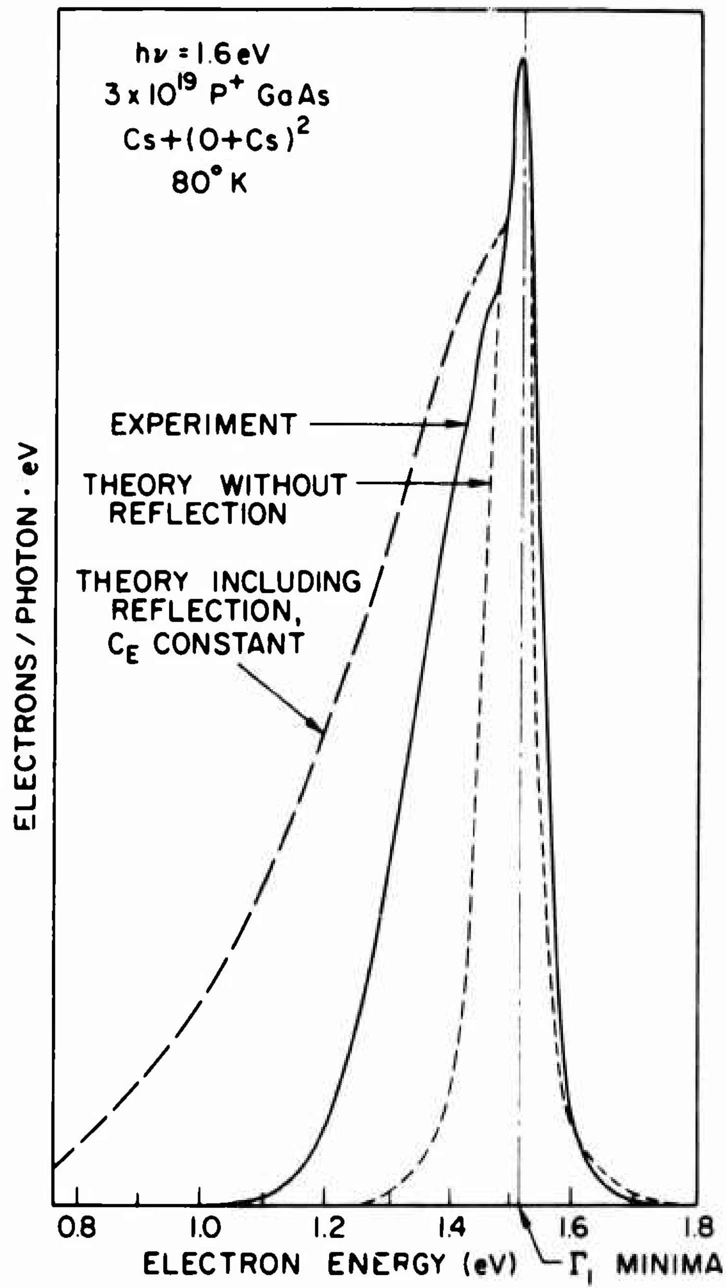

FIG. 36. Comparison between theory and experiment for the shape of the 80°K energy distribution curve.

For X_1 and Γ_1 electrons, dropping below the vacuum level cannot be ignored. The simplest estimate of escape probability for this case ignores optical phonon scattering in the band bending region and assumes a sharp cutoff of C_E at the vacuum level, giving

$$P = C_E \sum_{n=0}^{\ell} C_R^{\,n} \tag{9.7}$$

where ℓ is the next integer smaller than $\frac{E_{min.} - E_{vac.\ level}}{.06}$, and $\frac{C_E}{C_R}$ is assumed constant as C_{ST} varies. This calculation is shown in Fig. 37 for the case of an optimum (Cs + $(O+Cs)^6$) surface treatment.[20] For this surface treatment, roughly 80% of the electrons pass through the surface layers unabsorbed. Thus for this approximation, absorption in the (O+Cs) layers is neglected. This is intended as a rough estimate of escape probability variation with surface state density and not as an exact calculation. $\frac{C_E}{C_R}$ is undoubtedly a function of electron energy.

For the sample of Fig. 36, the maximum escape probability measured is .4, giving from Eq. (9.6), C_{ST} = .18 and C_R = .70. Using these values and introducing reflection into the model, we obtain the long-dashed theoretical curve shown in Fig. 36 . The theoretical curve is now drawn with the proper magnitude scale. The remaining difference between the theoretical and experimental curves is due to the fact that C_E and C_{ST} are functions of the electron energy rather than constants. Not enough data is available to determine these functions quantitatively. C_E is zero for energies below the vacuum level, and increases with increasing electron energy. The energy of the bottom of the tail of the measured EDC is therefore a good measurement of the energy of the vacuum level.

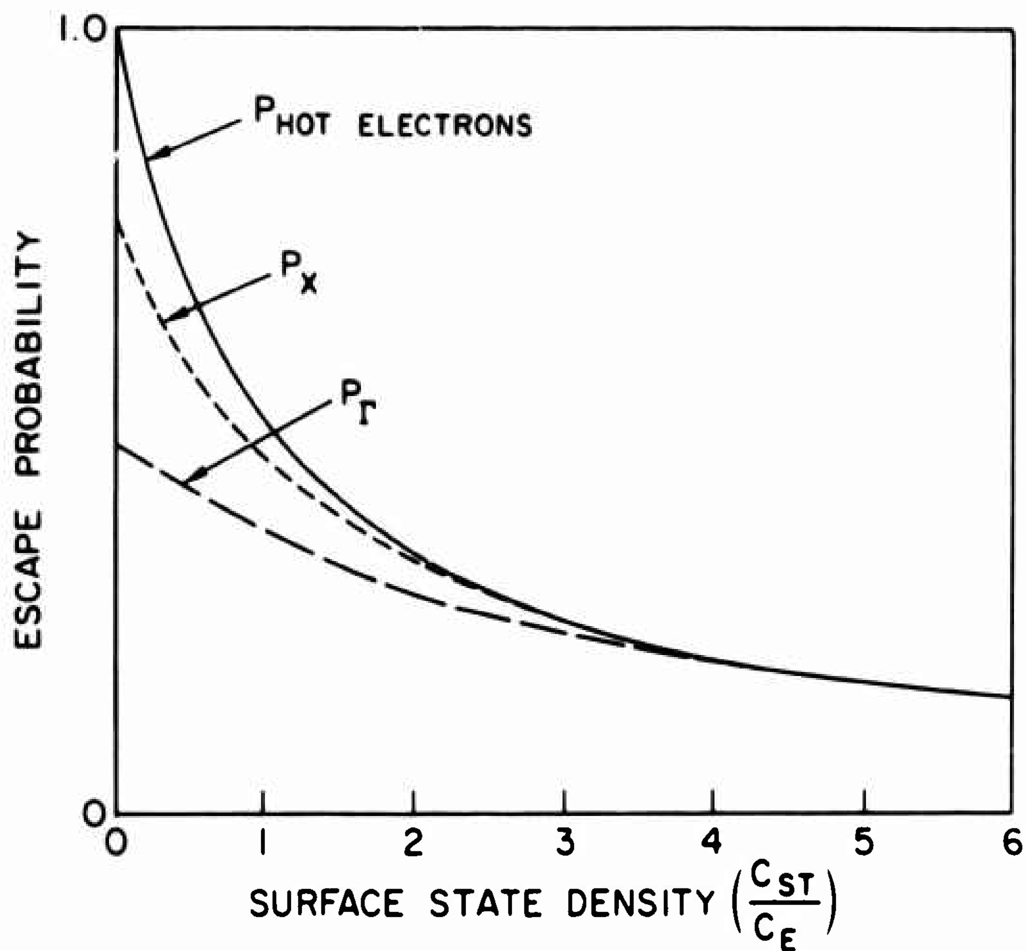

FIG. 37. Estimate from a simplified model of the effect of surface states on escape probability.

Comparison of the energy distribution curves for low yield (C_{ST} high) samples, such as shown in Fig. 26, and high yield (C_{ST} negligible) samples, such as shown in Fig. 10, show that low energy electrons are more adversely affected by high surface state densities than high-energy electrons, indicating that C_{ST} decreases with increasing electron energy, as expected.

By adding 30 (O + Cs) layers to the surface, we lower the vacuum level far enough[20] that C_E no longer varies rapidly with energy. Figure 38 shows the comparison between theory and experiment for this case. The theoretical curve has been multiplied by .25 to take into account absorption in the (O + Cs) layers. The agreement is now good.

In Fig. 36 the ratio between the area under the experimental curve and the area under the long-dashed theoretical curve, multiplied by the maximum escape probability (.4), gives the Γ escape probability, which is .22 at liquid nitrogen temperature for this sample and surface treatment.

The difference between the measured (.20 eV) and calculated (.12 eV) half-amplitude widths for the Γ_1 peak at room temperature can also be accounted for by multiple reflections at the surface.

Half-amplitude width of the peak corresponding to electrons in the X minima cannot be measured directly because of the presence of Γ electrons and hot electrons, but the X peak appears slightly wider than the Γ peak. This is expected for two reasons. First, there is no cutoff of the low end of the distribution by electrons scattering to an energy lower than the vacuum level. Second, τ in the band bending region is smaller for electrons initially thermalized in X, both from the energy dependence of $\tau_{XX'}$, and from the fact that scattering to states in the X_3 minima is

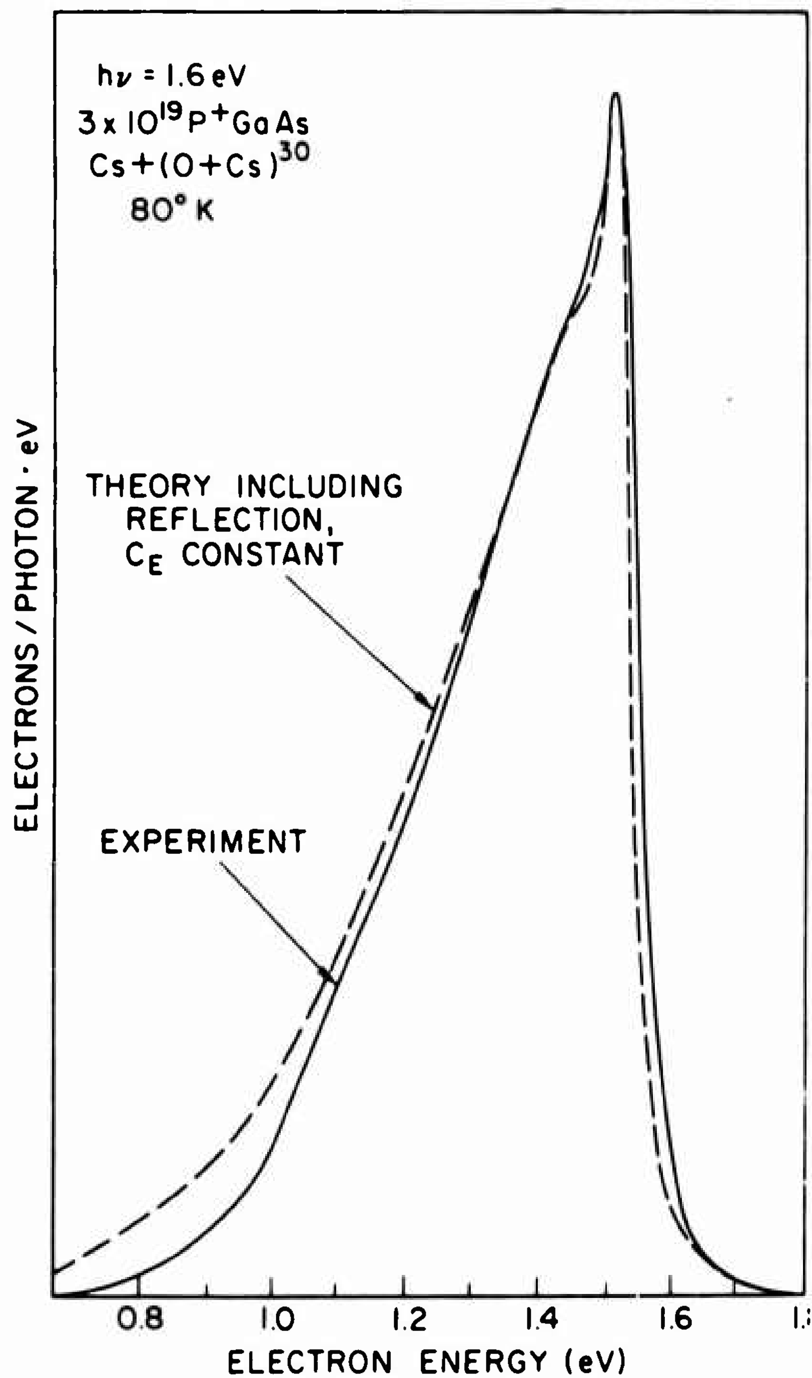

FIG. 38. Comparison between theory and experiment for the shape of the 80°K energy distribution curve for the case of C_E constant.

energetically possible as well as equivalent intervalley scattering. A smaller τ means a larger lifetime broadening of the distribution.

Examining Fig. 36 we can see that if the probability of escaping with no collisions were reduced by 20-30 percent, the sharp peak corresponding to unscattered electrons would be buried in the broader distribution. Apparently this is true for X electrons, the X distribution shows no such sharp structure.

The exact functional forms of $C_E(E)$, $C_R(E)$, and $C_{ST}(E)$ cannot be determined from the amount of experimental information available at this time, preventing the development of a quantitative theory for calculation of escape probability. However, if we assume that for samples where C_{ST} is negligible that escape probability is a function only of the energy difference between the electron energy and the vacuum level, we do have enough information to plot this function. The vacuum level to valence band spacing is determined from a liquid nitrogen temperature energy distribution curve in the manner indicated in Fig. 39. The measured vacuum level depends on the amount of broadening due to instrumental and other causes which is assumed, and should not be considered any more accurate than within 0.1 eV. For Zn doping in the range of 1-4 x $10^{19}/cm^3$, the Fermi level is at the top of the valence band in the bulk of the crystal, so the measured value of the vacuum level is also the value of the work function. The top curve in Fig. 40 shows this measured work function vs the number of additional oxygen-cesium layers applied.

There will be some absorption of electrons in the oxygen-cesium layers. This absorption was measured by comparing the hot electron (2.5 eV) escape probabilities with 0, 1, 2, and 30 additional (O+Cs)

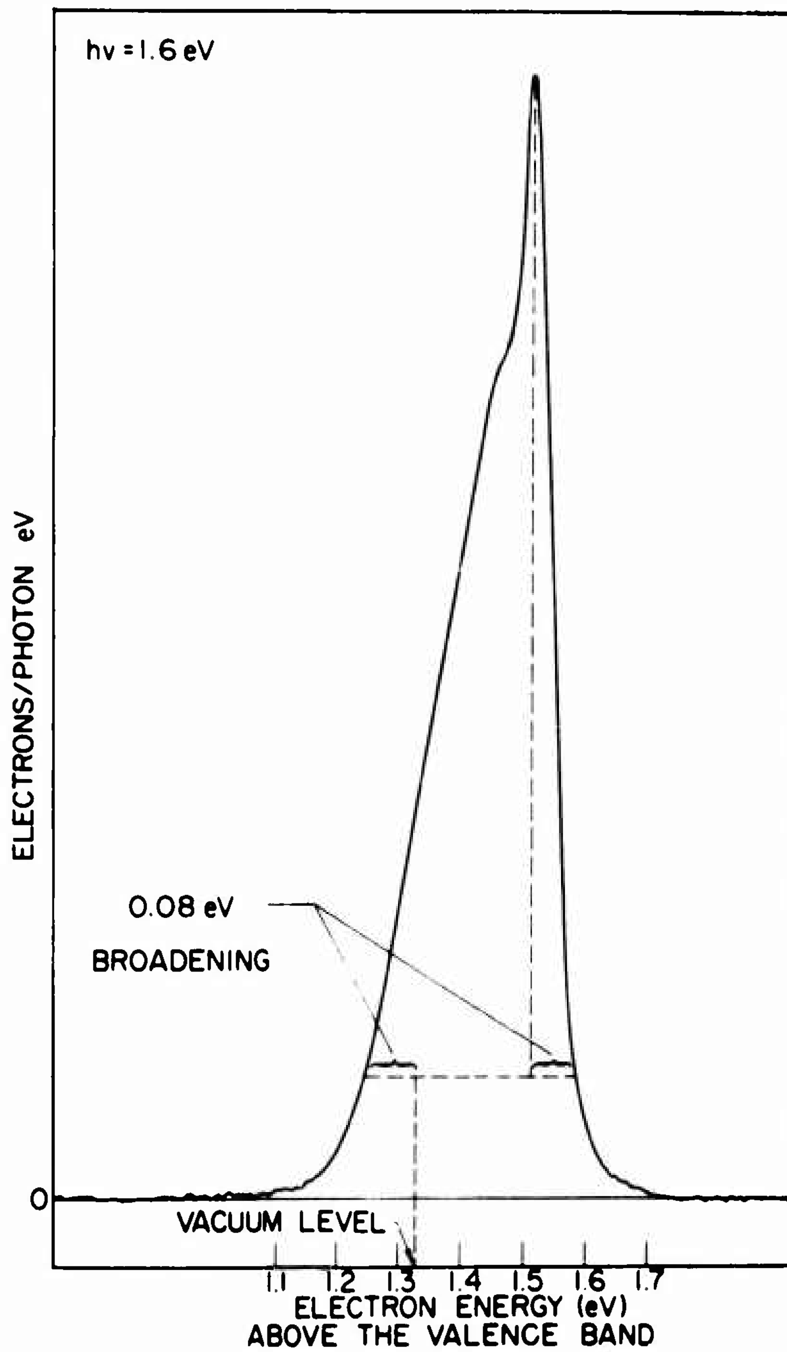

FIG. 39. High resolution electron energy distribution curve for a photon energy of 1.6 eV at 80°K showing the peak of electrons thermalized in the Γ minima and the tail of electrons which are scattered in the band-bending region and reflected from the surface.

layers, and is shown in the bottom curve of Fig. 40. The curve is drawn between 2 and 30 layers by assuming a constant absorption length, for which the probability of passing through a given thickness T given by

$$P = e^{-T/La}$$

where La is the absorption length.

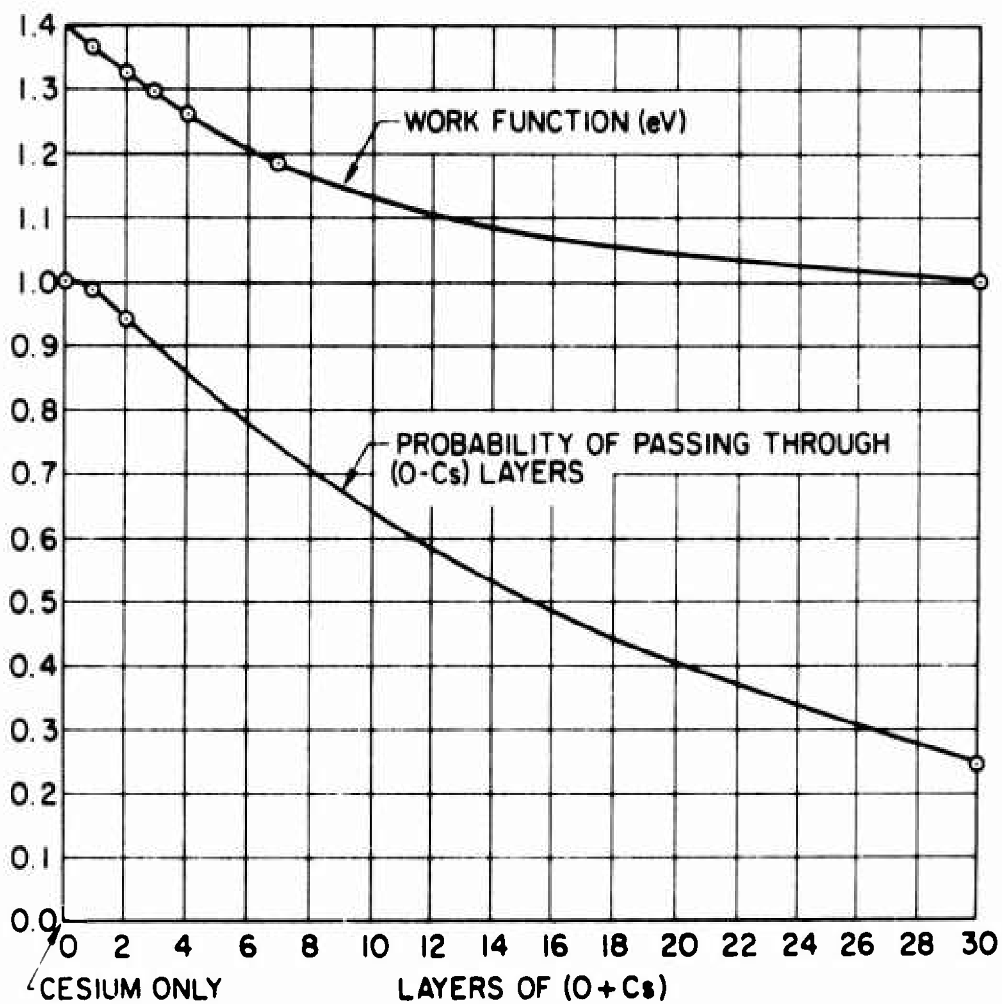

FIG. 40. Effects of additional oxygen-cesium layers, showing the vacuum level lowering and the electron absorption as measured experimentally.

For the same surface treatment for which the vacuum level is obtained as shown in Fig. 39, we obtain experimentally the Γ and X escape probabilities from a match to the two-minima diffusion theory discussed earlier. After correcting for absorption in the (O+Cs) layers from Fig. 40, we obtain two points (one for Γ and one for X) on a curve plotting the escape probability vs energy above the vacuum level. Additional points are obtained for other surface treatments, and Fig. 41 shows a smooth curve fitting these points. The curve of Fig. 41 is very steep near

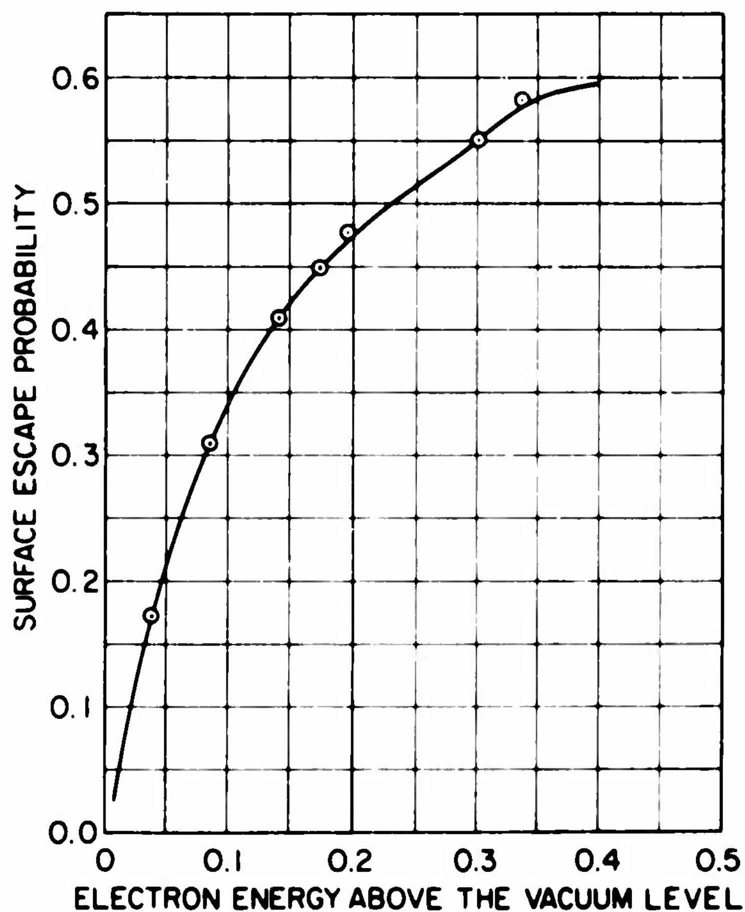

FIG. 41. Surface escape probability vs electron energy above the work function, measured for a 1 x $10^{19}/cm^3$ sample. Slight differences could be expected for different doping due to the differing width of the band-bending region.

threshold. For electron energies near the vacuum level, a 10 millivolt decrease in work function will triple the Γ escape probability (tripling the yield near threshold). This extreme sensitivity to small changes in vacuum level probably accounts for the wide range of sensitivities obtained by some workers under seemingly identical preparation conditions.

The actual escape probability for any surface treatment is the product of the surface escape probability and the probability of passing through the (O+Cs) layers. Figure 42 shows the Γ and X escape proba-

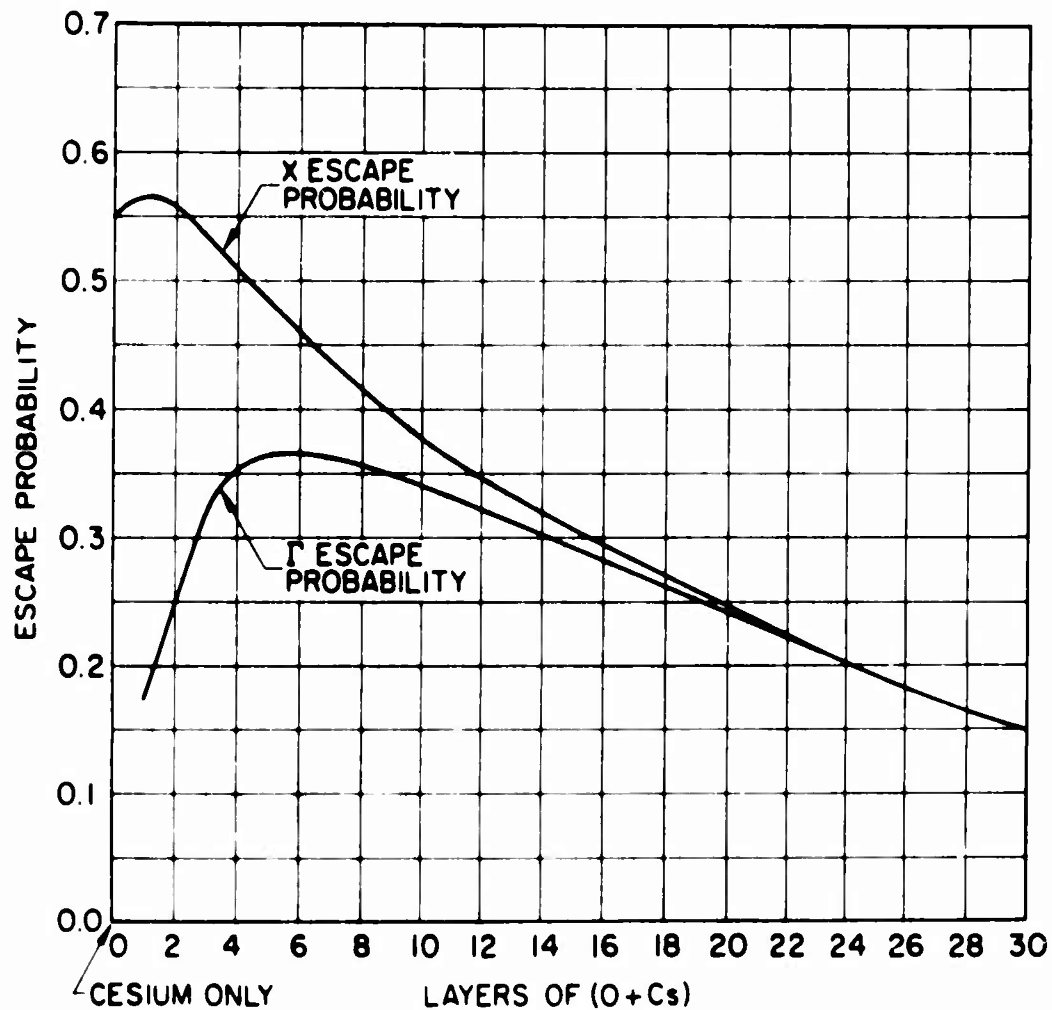

FIG. 42. Γ and X escape probability for a 1 x $10^{19}/cm^3$ sample calculated using Figs. 40 and 41.

bilities for a 1 x $10^{19}/cm^3$ sample calculated using Figs. 40 and 41. Figure 43 shows energy distribution curves for n = 2 and N = 30. As is predicted by Fig. 42, the X escape probability changes by a much larger factor than the Γ escape probability. The work function lowering is also evident. The fact that the relative heights of the X and Γ peaks agree with the predictions of Fig. 42 implies that absorption in the cesium-

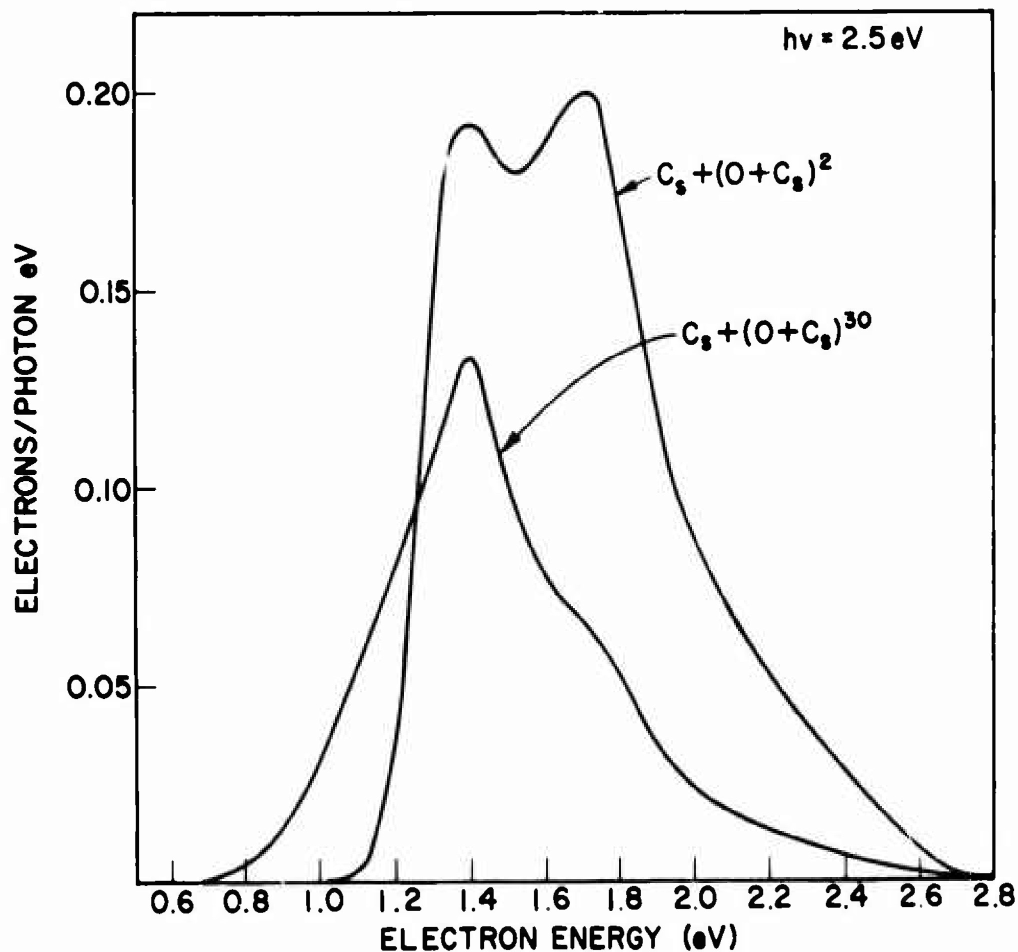

FIG. 43. Energy distribution curves at 300°K showing the effect of 30 (O+Cs) layers on the energy distribution. The large decrease in X escape probability, the smaller decrease in Γ escape probability, and the lowering of the work function are all clearly visible.

oxygen layers is the major loss process, rather than a scattering down in energy of electrons in many small steps, such as by an optical phonon scattering process. Obviously there is some scattering with small energy exchanges taking place, as the peaks in the E.D.C.'s taken for the Cs + $(O+Cs)^{30}$ surface treatment show a slight broadening of the peaks. Assuming that the many (O+Cs) layers do not change the work function of the collector can, we can determine that an average of approximately 0.1 eV in inergy is lost by electrons passing through $(O+Cs)^{30}$ layers. From probability theory for random scattering events, there is a relationship between the average energy lost in scattering, and the additional width of the scattered distribution over that of the initial distribution. For example, if the initial distribution is a delta function, by the time that the average energy loss is 0.1 eV, the distribution has a half-width of 0.06 eV. (Calculated for statistics applicable for optical phonon scattering.) By examining the experimental curves in Figs. 36 and 38, we can see that the additional broadening of the peak in the distribution is such that no more than approximately 0.1 eV average energy is lost. With the electron affinity being lowered by 0.4 eV, obviously the less than 0.1 eV energy loss through scattering in the oxygen-cesium layers cannot explain all or even a significant part of the loss of yield observed with a thick coating.

If scattering in small energy steps to below the vacuum level were the major cause of reduced yield with the thick layers, then the yield would be reduced more for low photon energies where only Γ electrons are present in the distribution, than for higher photon energies where X electrons are also present, because the X electrons could loose more

energy before dropping below the vacuum level. In fact the opposite is true. At 1.6 eV, the yield with 30 layers is down only to 0.8 of the yield with two layers; while at 2.0 eV, the yield with 30 layers is down to 0.5 of the yield with two layers (as predicted by the curves in Fig.42 which are based on the absorption assumption).

Thus we have several pieces of information which lead us to believe that scattering in small energy steps is not important in determining the effects of thick oxygen-cesium layers. Since a significant number of electrons do not make it through these layers, there must be an absorption process, some process through which the electrons can loose enough energy to drop lower in energy than the vacuum level in one step. This process is apparently just as effective for high energy electrons as for low energy electrons. If we assume no energy dependence and a probability for absorption for any one electron which is independent of time and position in the cesium-oxide layers, we obtain a probability for passing through the oxygen-cesium layers which is given by

$$P = e^{-T/La}$$

where T is the thickness and La is the absorption length. This is just the form used earlier.

X. EFFECTS OF DOPING ON YIELD

The level of doping which is used in the GaAs sample has two effects on the yield obtained. As shown in Table I in Section III, higher doping levels cause a decrease in the Γ diffusion length, which in turn causes a decrease in the yield obtained for a given escape probability, especially for photon energies close to threshold where α is small. The top two curves in Fig. 44 show the yield for two samples with differing diffusion lengths which could be obtained if it were possible to have an escape probability of 1.0. It is clear that the $1 \times 10^{19}/cm^3$ doped sample with a diffusion length of 1.6 microns has a definite advantage over the $4 \times 10^{19}/cm^3$ doped sample with a diffusion length of 1.0 microns. This factor indicates that we should use lightly-doped samples.

For a surface treatment of only cesium, the vacuum level is very close to the conduction band minimum in the bulk of the crystal. As shown in Fig. 41, a small change in the vacuum level can produce a large change in the Γ escape probability. The vacuum level may be lowered slightly (assuming Fermi level pinned at the surface as is apparently the case) by increasing the doping level to lower the Fermi level in the bulk crystal. In addition, Fig. 41 measured for a crystal with heavier doping would have a slightly steeper slope near the origin due to fewer optical phonon scattering events occurring in the narrower band-bending region. As a result of these considerations, for a surface treatment of cesium only the experimental yield for the 4×10^{19} crystal is higher than for the 1×10^{19} crystal as shown in Fig. 45.

We can have both the longer diffusion length of the lightly-doped crystal and a higher escape probability by applying additional oxygen-

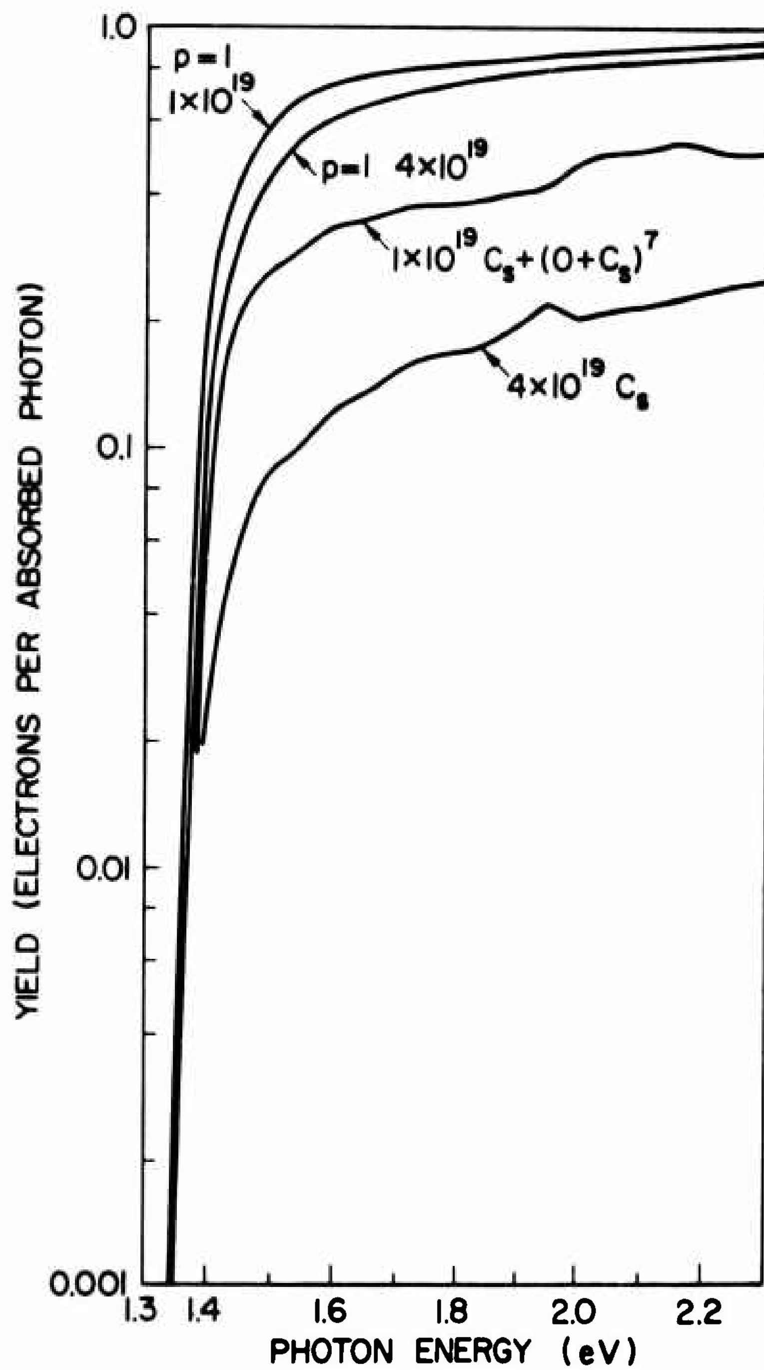

Fig. 44. Theoretically maximum possible (escape probability = 1.0) yield for samples with two different diffusion lengths, compared with the actual yield obtained from those samples.

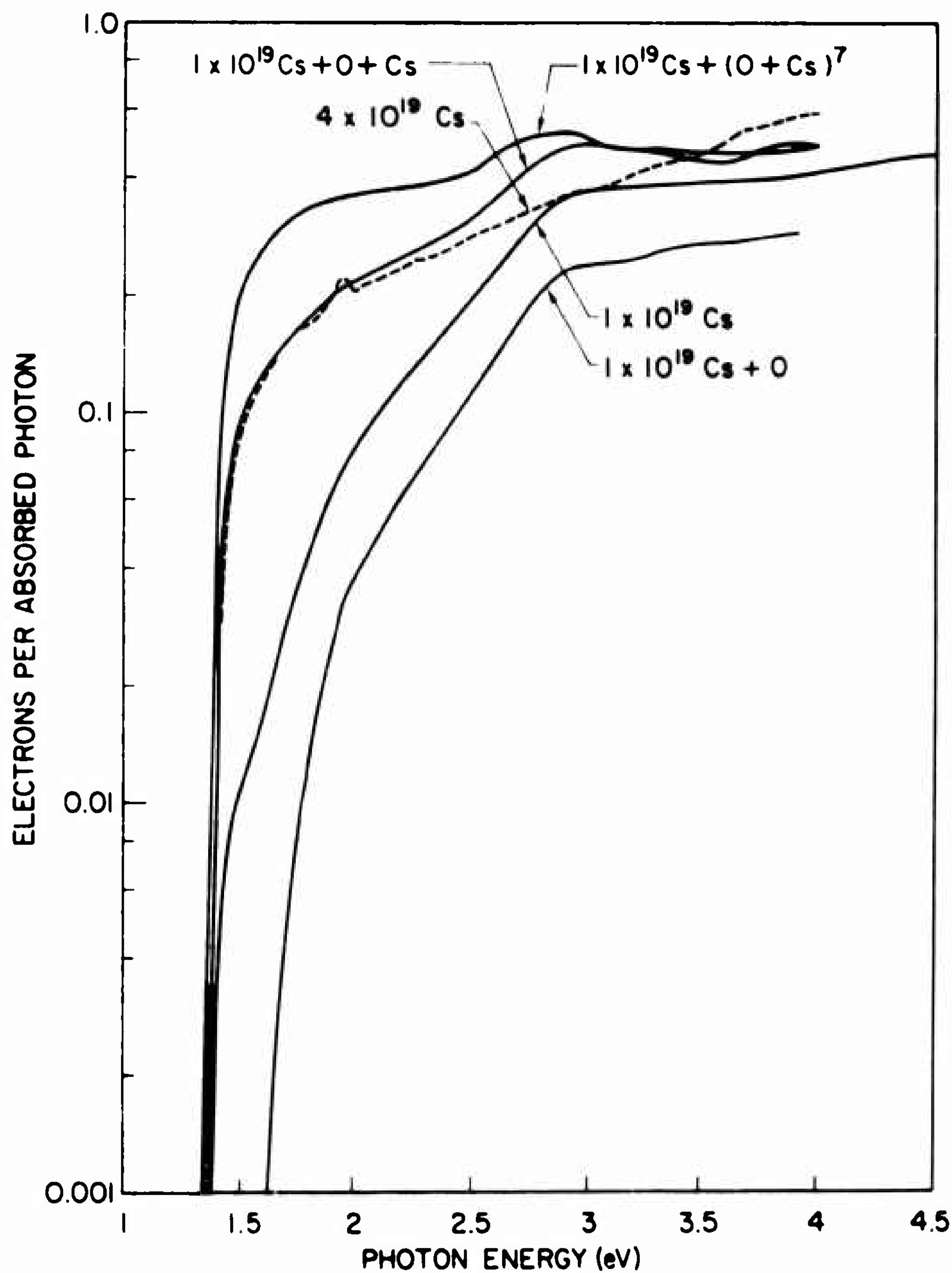

FIG. 45. Yield curves comparing different doping densities and surface treatments. The yield after each step in applying a Cs + (O+Cs) surface treatment is shown.

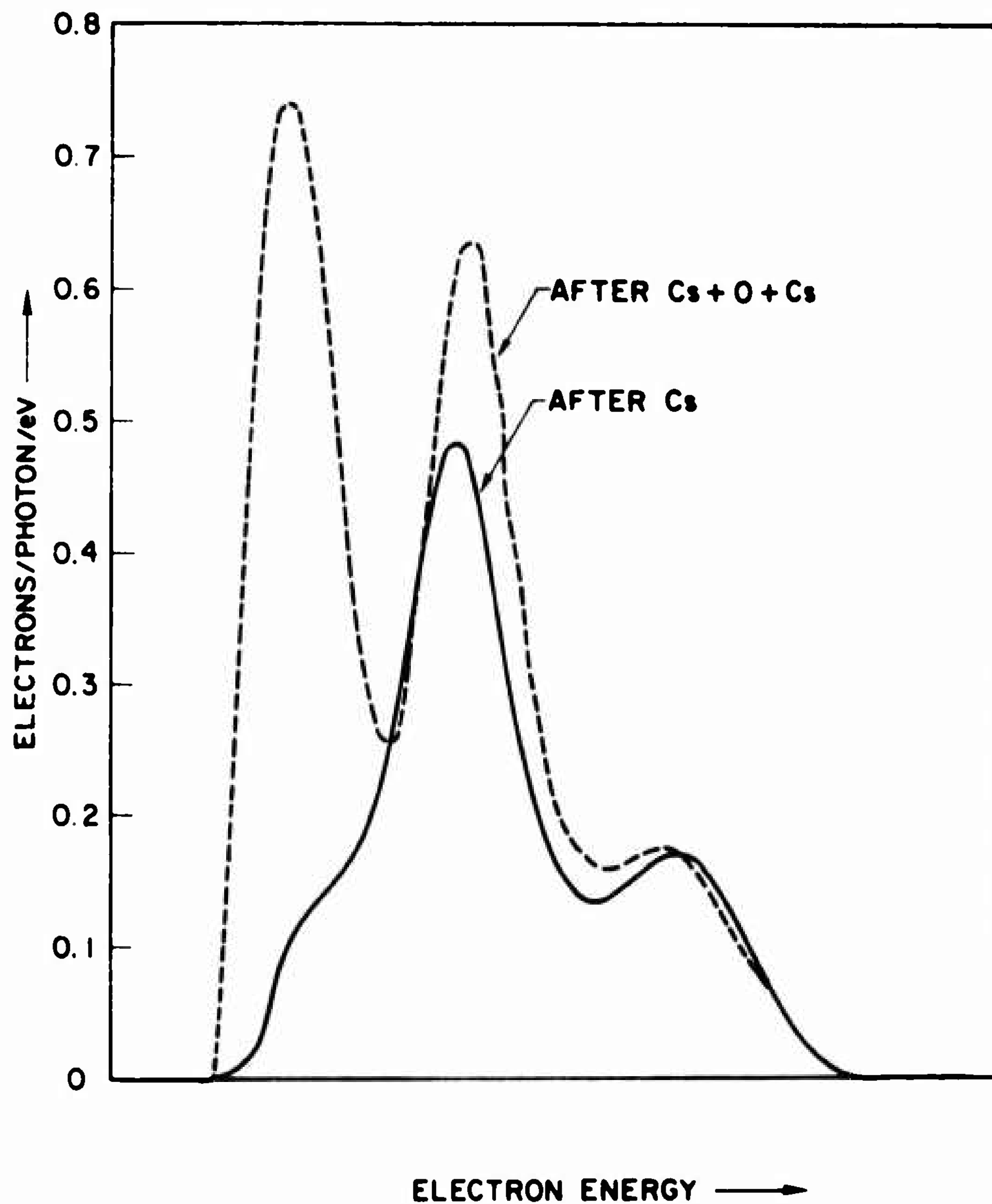

FIG. 46. Normalized energy distribution curves for a photon energy of 2.6 eV before and after oxygen and recesiation, for a 1 x $10^{19}/cm^3$ Zn-doped crystal.

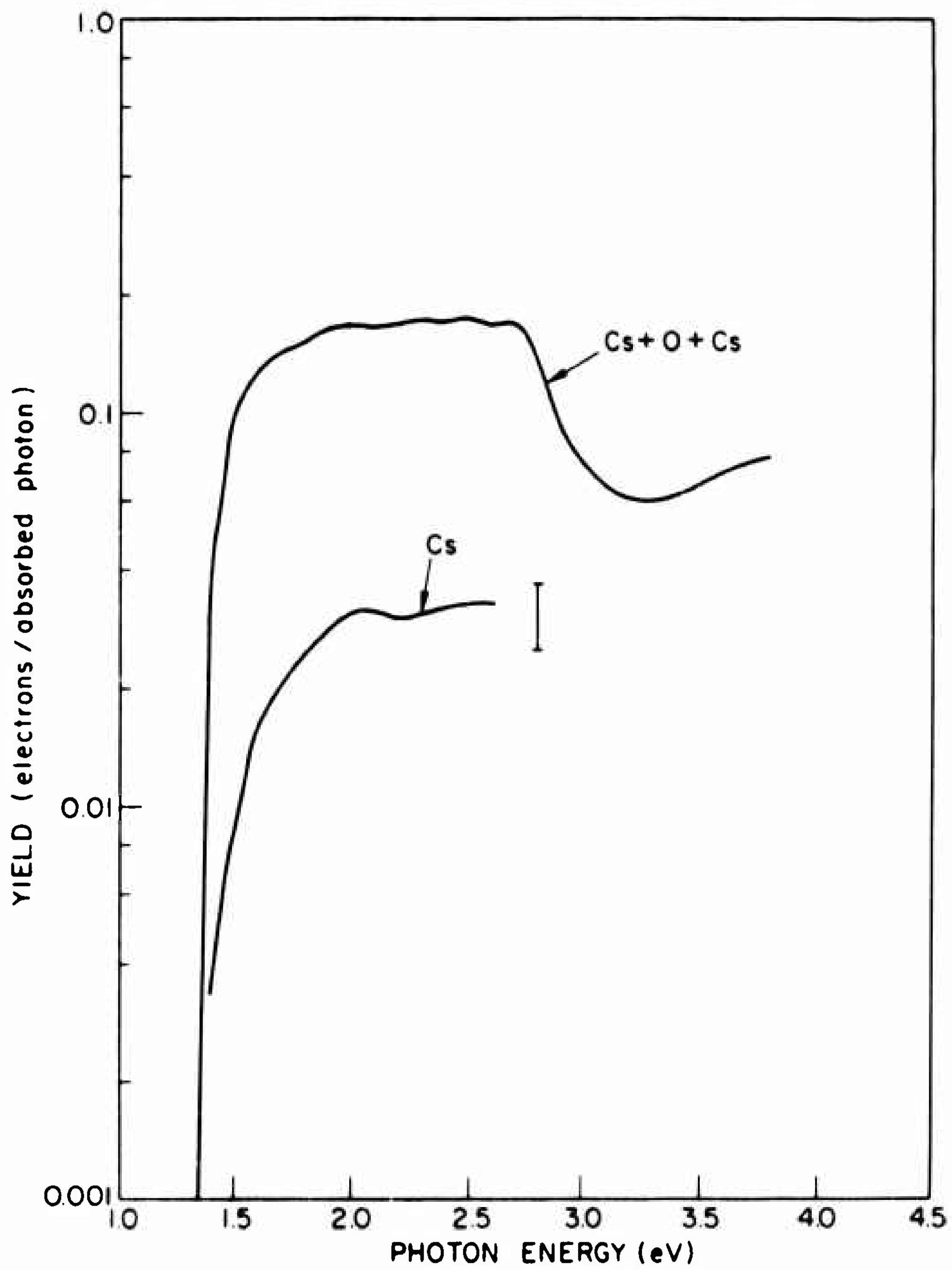

FIG. 47. Yield from electrons thermalized in the Γ_1 minimum for a 1 x $10^{19}/cm^3$ Zn-doped crystal with a Cs only and a Cs + (O+Cs) surface treatment.

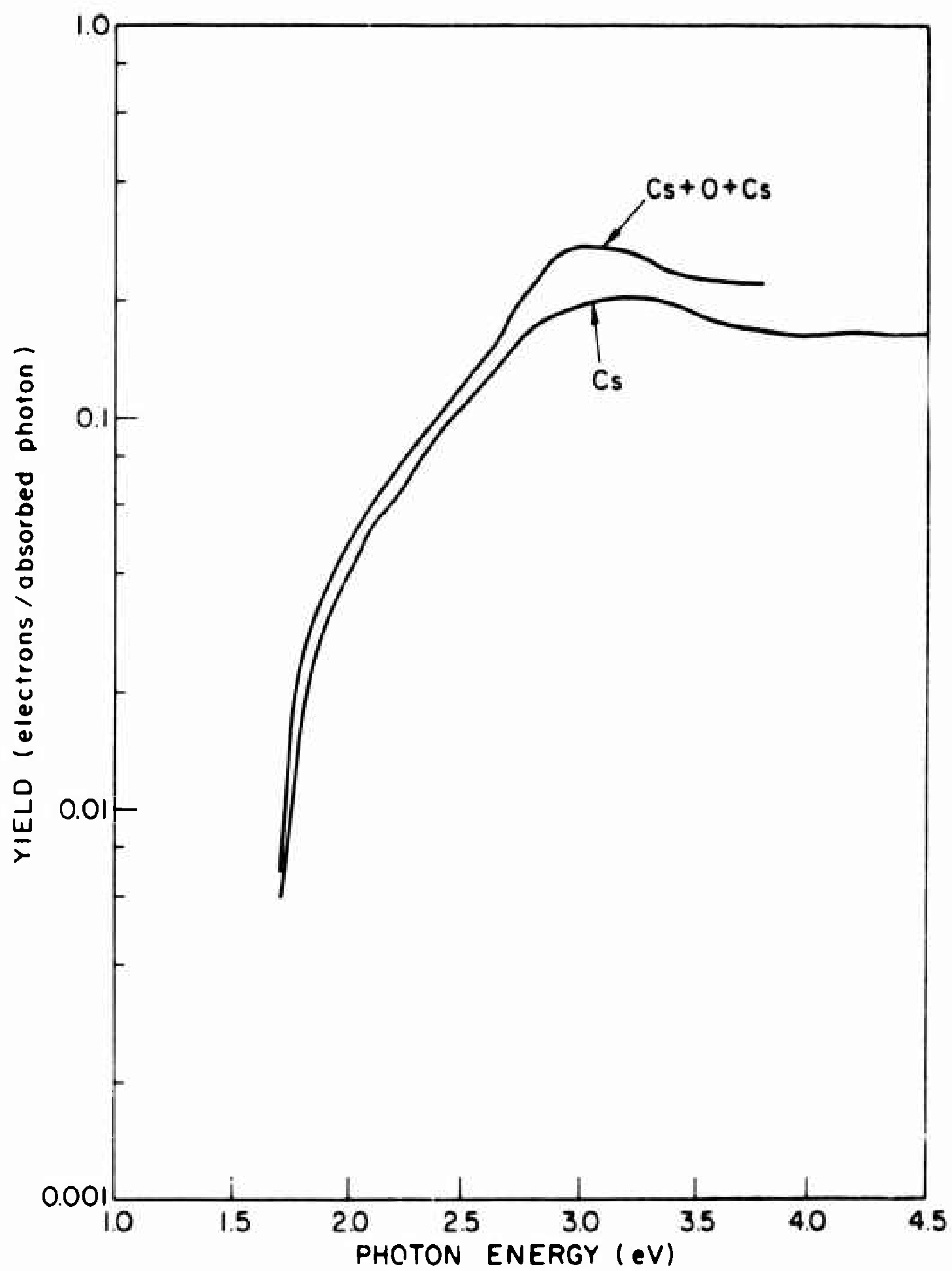

FIG. 48. Yield from electrons thermalized in the X_1 minima for a $1 \times 10^{19}/cm^3$ Zn-doped crystal with a Cs only and a Cs + (O+Cs) surface treatment.

cesium layers to the surface. Figure 45 also shows the yield for the 1×10^{19} crystal after applying a layer of oxygen, and again after cesiating to the point of maximum yield. The yield is now practically identical with that obtained from the 4×10^{19} crystal. From Fig. 46 it is clear that the Γ escape probability has increased dramatically, and the X escape probability has increased slightly. The hot electron escape probability is not changed appreciably. Figure 47 shows the Γ yield, and Fig. 48 the X yield, for both a cesium only and a Cs + (O+Cs) surface treatment.

We can increase the escape probability even further by applying more oxygen-cesium layers up to a point where electron absorption in the additional layers does more harm than the additional lowering of the work function does good. Figure 49 shows the measured escape probability for Γ electrons on a 1×10^{19} sample vs the number of additional oxygen-cesium layers. A broad maximum occurred with six additional layers.

Figure 50 shows our experimental results which we believe to be near the optimum obtainable with the techniques used. The 4×10^{19} data indicate a near optimum Cs only result, while the 1×10^{19} data indicate a near optimum Cs + $(O+Cs)^n$ result, corresponding to a sensitivity of approximately 1000 μA/lumen. The yield obtained from a commercial S-1 photocathode is shown for comparison.

The yield curves shown so far in this section have been for samples which had very small if any effects from surface impurities or defects. Figure 51 shows the yield at both room temperature and liquid nitrogen temperature for a sample with a large surface trapping coefficient. The yield is considerably below the best obtained. The yield increases

at liquid nitrogen temperature because of the increase in Γ escape probability. This increase and the increase in the threshold photon energy are caused by an increase in the band gap as the crystal is cooled. Had a high value of Γ escape probability been obtainable initially, the increase in yield with cooling might not have occurred.

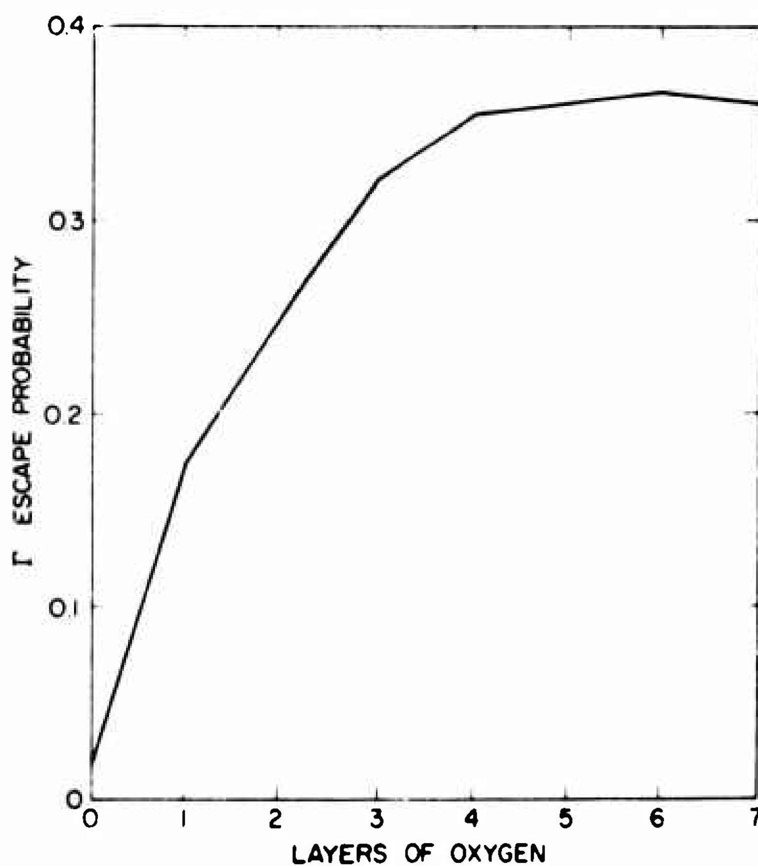

FIG. 49. Experimental Γ escape probability for various surface treatments.

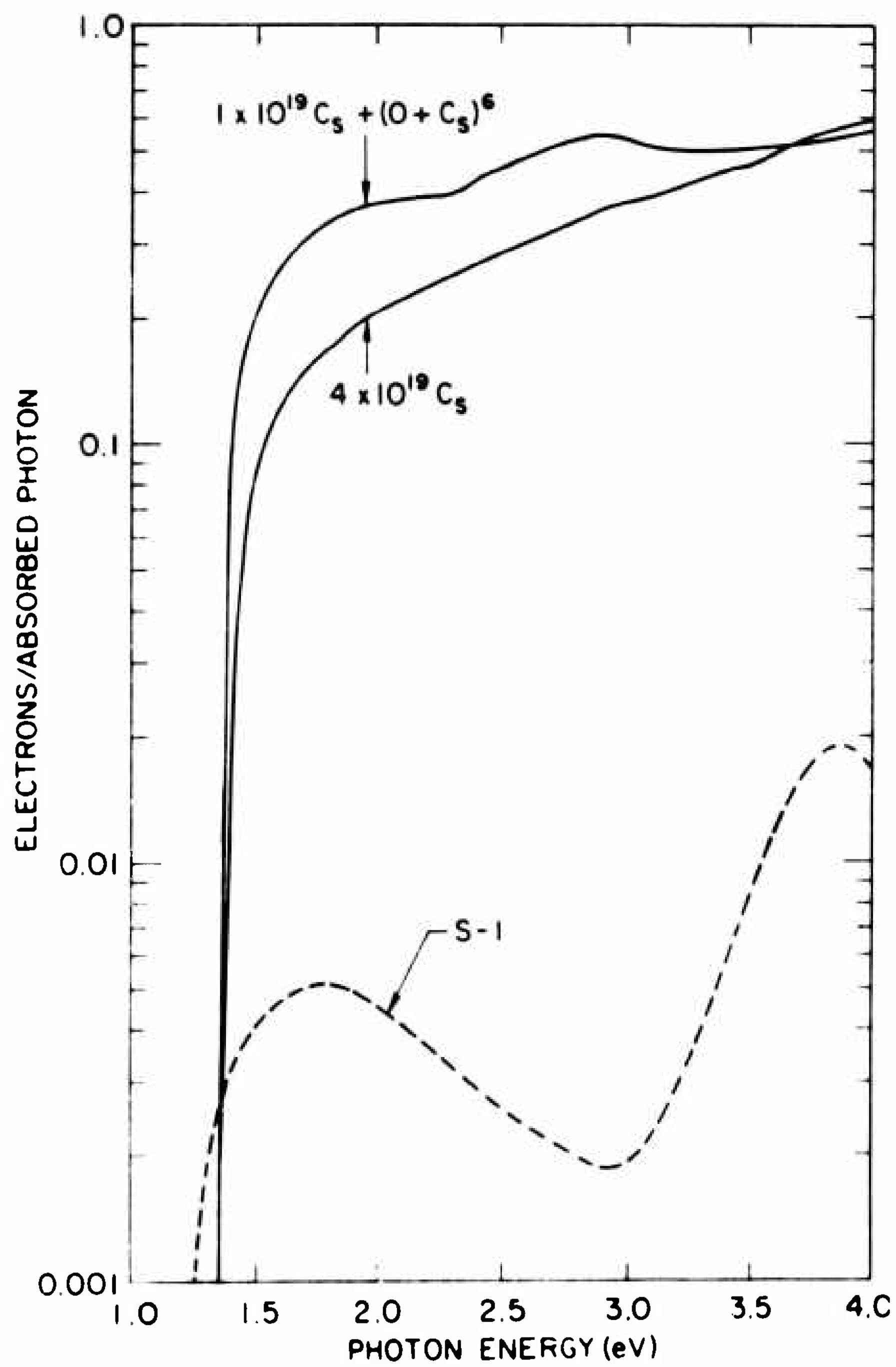

FIG. 50. Absolute quantum yield curves shown for optimum cesium only treatment (4×10^{19} Cs), optimum oxygen-cesium treatment (1×10^{19} Cs + $(O+Cs)^6$), and, for comparison, a commercial S-1 photocathode.

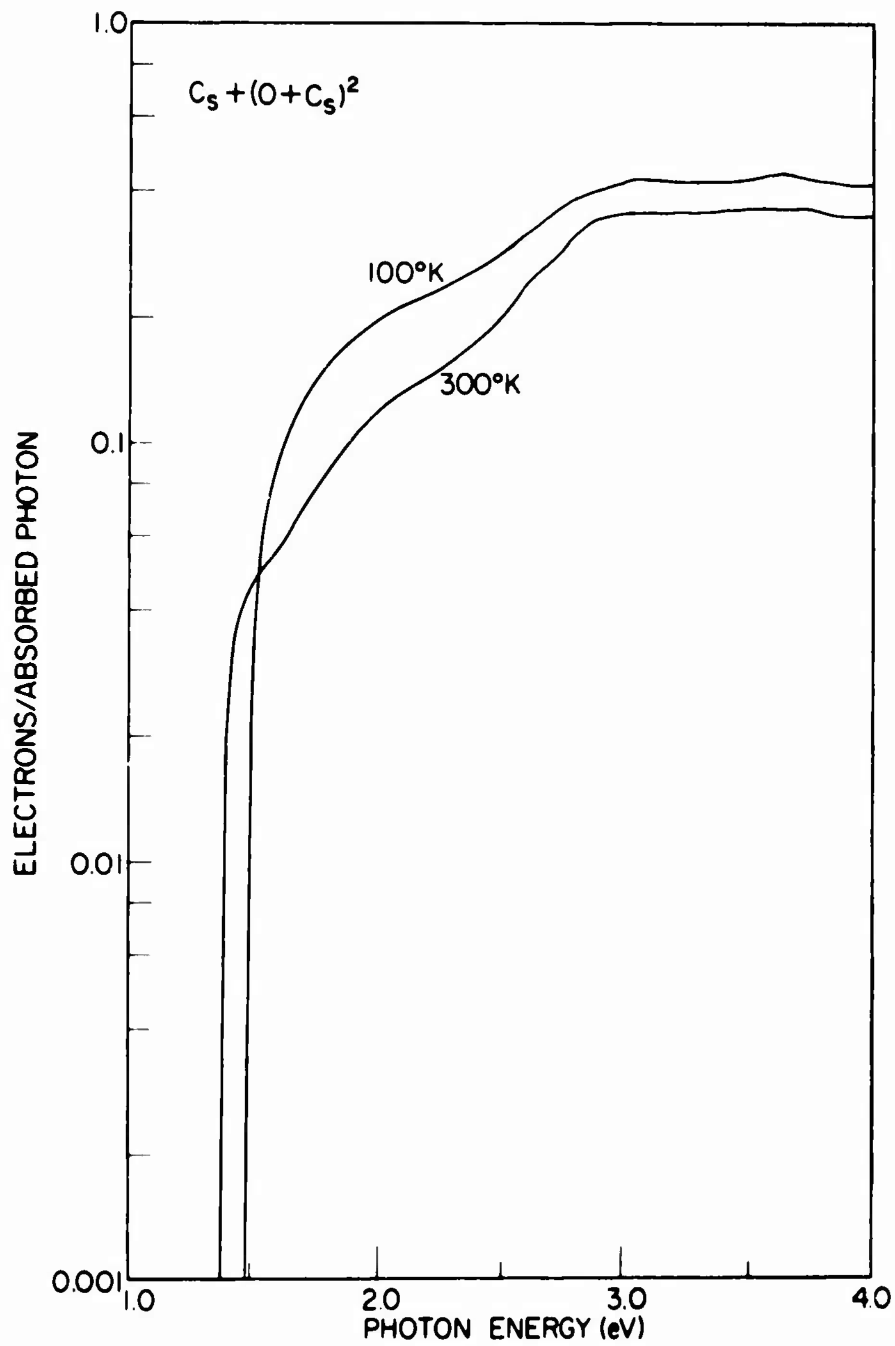

FIG. 51. Yield at room temperature and liquid nitrogen temperature from a 3 x 10^{19} Zn-doped GaAs crystal which has a large surface trapping coefficient.

XI. EFFECTS OF HEATING ON THE CLEAVED GaAs SURFACE

In conjunction with the effort to produce a useful GaAs photoemission surface by some means other than cleaving, a check was made on the effects of heating on the cleaved and cesiated surface.

Initial cesiation has been done at a temperature of 70 to 75°C, as described earlier. Re-heating of the cesiated crystal to this temperature for 8 hours causes some cesium to leave the surface, increasing the work function by $\approx$ 0.25 eV. Applying additional cesium to the surface restores the original condition.

Heating of the cesiated crystal to 150°C causes irreversible deleterious effects. After heating to this temperature, the sticking probability for cesium is reduced to the point where the optimum cesiation is obtained by cooling the crystal while maintaining the cesium partial pressure as high as possible. The best results that could be obtained using this method were a Γ_1 escape probability down from the optimum by a factor of 1.5 after 45 minutes at 150°C, and down by a factor of 30 after 12 hours at 150°C (at a pressure of 10^{-9} Torr). In both of these cases, the X_1 escape probability was reduced only slightly, indicating that the major difference after heating and recesiating was a higher work function.

After heating to 200°C for one hour, slight physical changes could be noticed on the cleaved surface. In particular, under a microscope, th the previously sharp fine cleavage lines running across the face of the crystal were somewhat smoothed with their end points blending into the flat crystal face instead of being clearly defined. Recesiation after this heat treatment showed the Γ_1 escape probability reduced by a factor

of 4 and the X_1 escape probability reduced by a factor of 1.7. This significant reduction in X_1 escape probability coupled with the moderate reduction in Γ_1 escape probability indicates that after heating to 200°C the work function is no longer uniform across the crystal face. Yield curves measured by Liu[25] for sputter-cleaned and high temperature annealed GaAs also seem indicative of a variation in work function across the surface.

No attempts have been made to determine the size of the spots over which the work function variation occurs or to determine whether the effects of heating differ if no cesium is present on the original cleaved surface.

XII. THE FUTURE FOR PRACTICAL PHOTOCATHODES

It should be emphasized that the results given in this report were obtained on cleaved surfaces under ultrahigh vacuum conditions. Two problems become apparent in processing the photocathode under less ideal conditions of poor vacuum or uncleaved surfaces. In some cases the work function is larger than shown in Fig. 41 for the same surface treatment, and in other cases a high density of surface states lowers the escape probability for a given work function. More work is required to adequately understand these effects.

Stability of the GaAs-Cs photocathode is also a problem. Deterioration in sensitivity is thought to occur with adsorption of oxygen or other contaminates on the cesium surface causing an increase in work function. At 10^{-11} Torr, the sensitivity of a cesium-only treated photocathode is reduced by about 15% in a two-week period. The oxygen-cesium treated photocathode shows less deterioration due to the much lower sensitivity to small changes in work function. In both cases, practically full sensitivity may be restored by applying a small amount of additional Cs.

Heating the photocathode to 75°C causes cesium to leave the surface, raising the work function about 0.25 eV, and drastically reducing the yield. Optimum sensitivity may be restored by reapplying Cs, but high temperature operation is obviously prohibited.

The possibility of a fatigue effect of the cathode at high levels of illumination was checked. While cesiating, a very low level of illumination is found to be required to prevent a reduction in photocurrent. However, after the crystal is covered with an optimum layer of cesium and cooled to room temperature, white light levels as high as that

required to produce a current density of 10^{-4} A/cm^2 did not produce a serious fatigue effect.

Cooling the photocathode to liquid nitrogen temperatures causes an increase in threshold and an increase in Γ escape probability due to the increase in the band gap to 1.5 eV. The dark current due to thermal generation in the band-bending region should be completely negligible at liquid nitrogen temperatures.

The materials work currently in progress on III-V mixed alloys points to additional possibilities in photocathode development. If high sensitivity in the visible light range is desired and near-infrared sensitivity is of no importance, a wider bandgap material such - $GaAs_xP_{1-x}As$ should give higher Γ escape probabilities and be easier to fabricate. If a lower threshold than 1.4 eV is desired, a smaller band gap material such as InP[23] or $Ga_xIn_{x-1}As$[24] may be used with oxygen-cesium surface layers at the expense of reduced escape probability.

XIII. SUGGESTIONS FOR FUTURE WORK

Several things in this report suggest areas which could be explored in the future.

Impurity scattering of minority carriers at the high doping levels used in photocathodes is not fully understood. A temperature dependence of the X diffusion length for samples with a variety of doping densities could help clear up this area.

A theoretical study of the temperature dependence of the Γ_1 diffusion length, when compared with experimental results, could lead to an answer to the important question of whether the diffusion length in commercially available material is limited by band-to-band recombination or by traps. If the limitation is in fact by traps, then liquid epitaxial material should ultimately produce better yields near threshold.

Much work remains to be done in the area of surface preparation before practical GaAs-Cs-O photocathodes can be made on a production basis.

The possibility of producing a cold cathode for vacuum tubes suggests itself if it is possible to inject electrons into a thin p region from a p-n junction, rather than producing the electrons by photoexcitation.

REFERENCES

1. J. J. Scheer and J. van Laar, Solid State Comm. 3, 189 (1965).

2. R. C. Eden, J. L. Moll, and W. E. Spicer, Phys. Rev. Letters 18, 597 (1967).

3. F. Herman, R. L. Kortum, C. D. Kuglin, J. P. Van Dyke, and S. Skillman, Methods of Computational Physics (Academic Press, New York, to be published in 1968), Vol. 8.

4. C. M. Chang, Ph.D. Thesis, Stanford University (unpublished), 1964.

5. F. Herman, private communication.

6. E. M. Conwell and M. O. Vassell, Phys. Rev. 166, 797 (1968).

7. S. W. Dickett, Phys. Rev. 166, 302 (1968).

8. A. D. Baer, Fundamental Investigations of Photoemission, Quarterly Report No. 6, Stanford University, July 1967.

9. J. S. Harris, Ph.D. Thesis, Stanford University (unpublished), 1968

10. G. King, J. Lees, and M. P. Wasse, quoted by P. N. Butcher and W. Fawcett, Phys. Letters 21, 489 (1966).

11. A. R. Hutson, A. Jayaraman, and A. S. Coriell, Phys. Rev. 155, 786 (1967).

12. D. N. Nasledor and S. V. Slobalchikor, Fiz. Tr. Tela 4, 2755

13. R. Mansfield, Proc. Phys. Soc. B 69, 76 (1956).

14. L. W. James, R. C. Eden, J. L. Moll, and W. E. Spicer, Phys. Rev. 174, 909 (1968).

15. M. D. Sturge, Phys. Rev. 127, 768 (1962).

16. H. Ehrenreich, Phys. Rev. 120, 1951 (1960).

17. I. Balslev, Phys. Rev. 173, 762 (1968).

18. A. G. Foyt, "Gunn Effect in Compound Semiconductors," Technical Report 385, Lincoln Laboratory, Lexington, Mass., 1965.

19. R. J. Powell, "Photoemission and Optical Studies of the Electronic Structure of NiO, CoO, and V_2O_4," Ph.D. Dissertation, Stanford University, 1967.

REFERENCES (Contd)

20. L. W. James, J. L. Moll, and W. E. Spicer, Proc. of the 1968 International Conference on GaAs, Dallas, Texas.

21. R. C. Eden, Ph.D. Thesis, Stanford University, 1967.

22. W. F. Krolikowski, Ph.D. Thesis, Stanford University, 1967.

23. R. L. Bell and J. J. Uebbing, Appl. Phys. Letters 12, 76 (1968).

24. J. J. Uebbing and R.L. Bell, Proc. IEEE 56, 1624 (1968).

25. Y. Lui and J. L. Moll, Fundamental Investigations of Photoemission, Quarterly Report No. 8, Stanford University, January 1968.

26. J. S. Harris and L. W. James, J. Appl. Phys. (to be published).

27. I. Kudman and T. Seidel, J. Appl. Phys. 33, 771 (1962).